A numerical investigation into the effects of positioning and rotation on the performance of two vertical-axis hydrokinetic turbines

by

Jody Soviak

A Thesis Submitted to the Faculty of Graduate Studies of
the University of Manitoba
in Partial Fulfilment of the Requirements of the Degree of

MASTER OF SCIENCE

Department of Mechanical Engineering
The University of Manitoba
Winnipeg

Abstract

Numerical simulation allows investigation into the influence of separation distance and rotation on the performance of two vertical-axis hydrokinetic turbines. Computational fluid dynamics is applied to calulate the lift and drag coefficients acting upon interacting NACA 0021 turbine blades for a Reynolds number of $Re_d = 10,000$. To understand the effect of separation distance, large-eddy simulation of the flow around side-by-side and staggered cylinders, $Re_D = 3,000$, and airfoils, $Re_c = 3,000$, are also performed. Based upon the simulations, a drag reduction of 11.3% and 19.8% is determined for the downstream cylinder and airfoil, respectively. A reduction in Reynolds stresses is also observed for the staggered configuration compared to the side-by-side configuration. Due to computational resources of large-eddy simulation, the Reynolds averaged Navier-Stokes method is also applied to investigate the influence of separation distance and rotation on two vertical axis hydrokinetic turbines. The numerical simulations show that a drag reduction of 15.5% occurs when the non-dimensional spanwise and streamwise separation distances, based on turbine diameter, reach 1 and 2, respectively.

Acknowledgements

I would like to take the opportunity to sincerly thank my advisors Dr. Bing-Chen Wang and Dr. Eric Bibeau for all their support, patience and teaching. All of the oppertunities they provided for me are greatly appreciated. I would also like to thank my committee members Dr. David Kuhn and Dr. Quiang Zhang for their time, Dr. Amir Birjandi for his guidance and support, Zeev Kapitankar for his help with the experimental set-up, Richard Lozowy for his help with learning the OpenFOAM software and Xingjin Fang for his help with debugging and coding using the large eddy simulation method.

I would also like to thank all of my friends and collegues in the research groups of both Dr. Bing-Chen Wang and Dr. Eric Bibeau who created a warm and welcoming environment.

Last, but not least, my appreciation goes to my family without whom this thesis would not have been possible.

Funding for this research was provided by NSERC discovery grant.

Contents

List of Tables

List of Figures

Nomenclature

English Symbols

A	Cross sectional area
a	Induction factor
B	Number of blades
C_D	Drag coefficient
C_K	Kormorgorov constant
C_L	Lift coefficient
C_P	Power coefficient
C_p	Pressure coefficient
C_Q	Torque coefficient
C_S	SGS stress model coefficient for SM and DSM
c	Chord length
c_T	Chord thickness
D	Cylinder diameter
d	Turbine diameter
E_{ii}	Different components of energy spectra: $i = 1, 2, 3$
F_D	Drag force
F_L	Lift force

f	Vortex shedding frequency
G	Gap width
k	Uncertainty by a coverage factor
L	Streamwise distance
$\mathcal{L}_{ij}$	Leonard type stress tensor
M_{ij}	Differential tensors
n	Number of data points
P	Power
p	Pressure
p_∞	Static pressure
q_∞	Dynamic pressure
R	Radius
Re	Reynolds number
Re_D	Reynolds number based on diameter
Re_c	Reynolds number based on chord length
S	Contact area
s	Estimated standard deviation
S_{ij}	Strain rate tensor: $(\partial u_i/\partial x_j + \partial u_j/\partial x_i)/2$
$\|S\|$	Norm of S_{ij}: $(2S_{ij}S_{ij})^{1/2}$
S_T	Strouhal number
T	Spanwise distance
t	Time
u_A, u_B	Type A and B error
u_C	Combined standard uncertainty
u_i	Velocity components
u, v, w	Instantaneous velocity components in x, y and z directions
U_∞	Free-stream mean velocity

x, y, z	Coordinates of a Cartesian frame

Greek Symbols

α	Incidence angle
α_{ij}	Test-grid level base tensors
β_{ij}	Grid level base tensors
β_2, γ_2, σ_k, $\sigma_{\omega,1}$, $\sigma_{\omega,2}$	K-ω-SST turbulence model constants
δ_{ij}	Kronecker delta
Δ	Grid size
Δt	Time step
Δx, Δy, Δz	Grid length in x, y and z directions, respectively
$\bar{\Delta}$	Grid level filter width; or cut-off length scale
$\tilde{\bar{\Delta}}$	Test-grid level filter width
ϵ	Viscous dissipation rate
η	Betz limit
θ	Angle
κ	Karman constant
λ	tip speed ratio
ν	Molecular kinematic viscosity of the fluid
ν_T	Turbulent eddy viscosity
ν_{sgs}	SGS kinematic eddy viscosity
ρ	Fluid density
τ_{ij}	SGS or Reynolds averaged stress tensor
ω	Specific rate of dissipation

Subscripts and Superscripts

$\bar{(\,)}$	A grid level filtered quantity for large eddy simulation
$\bar{(\,)}$	An averaged quantity for Reynolds averaged Navier stokes
$\tilde{\bar{(\,)}}$	A test-grid level filtered quantity
$\langle(\,)\rangle$	A test-grid level filtered quantity
$(\cdot)'$	Fluctuating quantity
$(\cdot)^*_{ij}$	A trace-free tensor: $(\cdot)^*_{ij} = (\cdot)_{ij} - (\cdot)_{kk}\delta_{ij}/3$
$(\cdot)^+$	Wall coordinates
$(\cdot)_i$, $(\cdot)_j$, $(\cdot)_{ij}$	Vectors or second-order tensors: $i, j = 1, 2, 3$
$(\cdot)_\infty$	Free-stream property
$\langle\,\rangle$	Time- and/or plane-averaged quantity

Abbreviations

2-D	2-Dimensional
3-D	3-Dimensional
ADV	Accoustic Doppler Velocimetry
CFD	Computational Fluid Dynamics
DES	Detached Eddy Simulation
DNS	Direct Numerical Simulation
DSM	Dynamic Smagorinsky Model
HAWT	Horizontal Axis Wind Turbine
LES	Large-Eddy Simulation
PIV	Particle Image Velocimetry
RANS	Reynolds-Averaged Navier-Stokes

SGS	Subgrid-Scale
SM	Smagorinsky Model
TI	Turbulence Intensity
TKE	Turbulent Kinetic Energy
TSR	Tip Speed Ratio
VAWT	Vertical Axis Wind Turbine

Chapter 1

Introduction

Mankind has become increasingly dependent on the usage of non-renewable fossil fuels such as crude oil, coal and natural gas. As the amount of usable fossil fuels continues to decrease and the usage of these products continues to increase, the human society faces an economic crisis. According to the United Nations Secretariat, the world population is approaching 7.2 billion people and is expected to increase by approximately one billion people to reach 8.1 billion people within the coming decade [1]. Associated with the growth of human population, the world energy requirements are also expected to increase by approximately 300 TWh during the next decade [2]. Moreover, the release of CO_2 from combustion of fossil fuels is affecting the equilibrium temperature of the air and oceans due to the greenhouse effect.

Due to the diminishing quantities of fossil fuels, the increase in global temperatures and the need to reduce the world's greenhouse gases, renewable energy technologies are becoming attractive despite their limitations. All renewable energy generation methods have limitations: wind and solar both have intermittency issues while hydro and geothermal have geographical issues [3]. The most common form of

Figure 1.1: 25 kW New Energy turbine being tested at the Canadian Hydrokinetic Turbine Test Centre for mooring loads and power performance. The turbine is out of the water as an acoustic Doppler velocity instrument is being position in front of the turbine for precise localized 3-D transient velocity measurements.

renewable energy in use today is hydro-power due to its reliability compared to other renewable energy forms. While many different methods for generating hydropower exist, the developing field of hydrokinetic marine turbines presents opportunities due the significant potential of the devices to be applied in coastal and remote communities. Figure 1.1 shows the testing a of 25kW New Energy turbine at the Canadian Hydrokinetic Turbine Test Centre. Table 1.1 provides a description of the potential of hydrokinetic turbine for several locations worldwide.

Hydrokinetic turbines operate by extracting the kinetic energy from a mass of water as it moves along a given route typically in a river, a tidal regime, and a drainage basin. There are two main configurations for hydrokinetic river turbines and numerous different types each with its own potential. The two major configurations of hydrokinetic turbines include the axial flow turbine, horizontal-axis, in which the axes

Table 1.1: Potential analysis of marine renewable energy

Location	Ressource Type	Available Energy	Notes	Ref
Canada (NS, NB, QC, BC, Arctic)	In-stream tidal	6.3 GW	Based on the mean power potential with 15% extraction	[4]
Canada (QC, ON, MB, BC, Arctic)	River current	3.57 GW	Based on the mean power potential with 15% extraction	[4]
Canada (BC, NS, NL)	Wave	2.75 GW	Based on the mean power potential with 15% extraction	[4]
Canada (Bay of Fundy)	Marine tidal	2.5 to 7 GW	2.5GW results in 5% change in tides	[5]
United States (except Alaska)	All types	14 GW		[6]
France	In-stream tidal	6GW	Based upon energy which can be extracted on par with current cost of wind generated electricity	[7]
France	Marine current and tidal	160GW	Based upon energy which can be extracted on par with current cost of wind generated electricity	[7]

run parallel to the fluid and the turbine employs propeller-like rotors to extract the kinetic energy of the flow. The cross flow turbine, vertical-axis, has axes orthogonal to the rotor and the turbines appear mostly as cylindrical rotating structures [8]. Figure 1.2 shows several different types of hydrokinetic turbines.

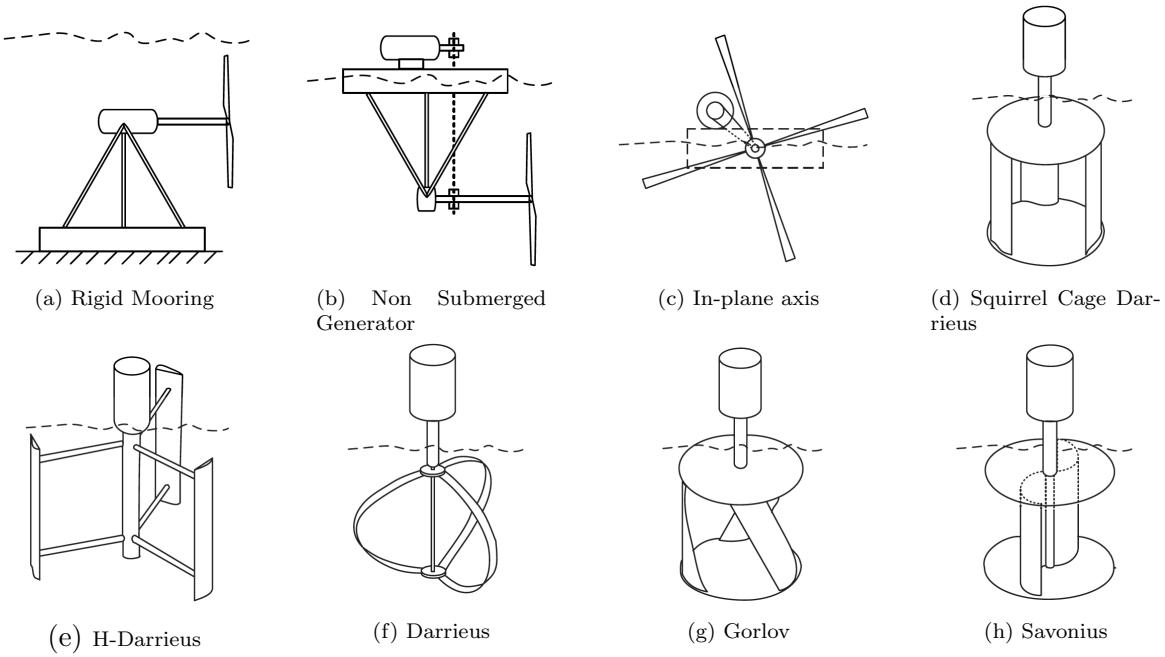

(a) Rigid Mooring (b) Non Submerged Generator (c) In-plane axis (d) Squirrel Cage Darrieus

(e) H-Darrieus (f) Darrieus (g) Gorlov (h) Savonius

Figure 1.2: Schematic representation of several different types of horizontal-axis and vertical axis turbines. ©2006 IEEE. Reprinted, with permission, from M. Khan, M. Iqbal and J. Quaicoe, A technology review and simulation based performance analysis of river current turbine systems, and May 2006

There are many proposed marine turbine projects whose economics are based the placement of turbines in a farm arrangement. One method to decrease the levelized cost of electricity is to produce more power by optimizing the configuration of turbines in a farm arrangement. An example is the proposed Canoe Pass project on the coast of British Columbia whose economics rest on the optimization of several vertical axis turbines in a relatively narrow passage. The focus of the current research is on vertical axis hydrokinetic turbines. The effects associated with two turbines operating within close proximity to each other will be studied. Specifically, the influence of positioning and rotation on the wake interactions and the performance of hydrokinetic turbines will be investigated through numerical simulations.

1.1 Objectives

The main objective of this research is to investigate the effects of turbine spacing, wake interaction and relative rotation on the performance of two closely spaced vertical axis hydrokinetic turbines using numerical approaches. To accomplish this goal, Large-Eddy Simulations (LES) simulations of stationary cylinders are performed to study the influence of the turbulence modelling on the wake interactions, how the wakes propagate downstream, how the wakes interact and how the positioning of the cylinders influences the wake interactions. The examination is conducted with respect to the velocity and turbulence statistics, pressure coefficients and force coefficients. Besides the cylinder configurations, airfoil configurations are also considered in the simulations to assess how two turbine blades interact with each other. The knowledge obtained by examining the wake interactions of airfoils and cylinders can be used as a means with which to initiate the investigation into two turbine interactions. Simulations of both stationary and rotating turbines are performed and compared to understand the influence of rotation on two hydrokinetic turbines.

Due to the complexity of the flow and relatively high Reynolds number, the rotating turbine simulations are performed using a Reynolds-Averaged Navier-Stokes (RANS) approach in conjunction with a k-ω-SST turbulence model. The k-ω-SST turbulence model is well documented for turbine [9] and similar aerospace applications [10].

The open-source Computational Fluid Dynamics (CFD) solver OpenFOAM v2.3.0 permits a numerical solution of the momentum, turbulence and continuity equations using parallel computing royalty free. In the following context, the literature relevant to this research is reviewed, including the single cylinder flow, two cylinder flow interactions, and turbine interactions. Since literature data related to the interactions of hydrokinetic turbines is limited in availability, results from wind turbines are also examined. Due to the assumption of incompressibility implied in both air and water, the results obtained for wind turbines provides a valid comparison with any results obtained from hydrokinetic turbines.

1.2 Outline of the thesis

A general outline of the thesis is as follows:

1. Simulate the flow around a single cylinder at $Re_D = 3,900$ using the LES turbulence modelling technique in OpenFOAM. Test two SubGrid Scale (SGS) models—the conventional Smagorinsky Model (SM) and Dynamic Smagorinsky Model (DSM)—and determine which model provides the best prediction of the flow around a bluff body. Compare the results to experimental results available in the literature.

2. Simulate the flow around side-by-side and staggered cylinders using LES for $Re_D = 3,000$ to gain an understanding of the influence of positioning and wake interactions on the resolved flow field. The comparative study focuses on the

first-order statistics and how the wakes interact in the downstream region of the cylinders. Such experiments are not available in the literature for comparison.

3. Simulate the flow around side-by-side and staggered stationary airfoils aligned at the $\frac{1}{4}$ chord point using LES for $Re_c = 3,000$. The analysis focuses on the turbulence activities indicated by the second-order moments of the flow field, and the lift and drag coefficients. Validate the model with experimental data obtained as part of this study.

4. Perform an experimental study in a water tunnel to validate the flow around side-by-side and staggered airfoils aligned at the $\frac{1}{4}$ chord point. The measurements are taken using Acoustic Doppler Velocimetry (ADV) and are used to validate the openFOAM models developed.

5. Preform multiple simulations of the flow around two vertical axis turbines using RANS for $Re_D = 10,000$ to determine the effects of positioning and rotation on the lift and drag coefficients. These numerical experiments contribute to decreasing the levelized cost of energy and hydrokinetic turbine farms. The previous items focused on validating the modelling approach to enable conclusions to be drawn on turbine spacing using a purely numerical approach. Experimental testing of 2 hydrokinetic turbines interacting are scheduled to be performed at the Canadian Hydro Kinetic Turbine Testing Center (CHTTC) as a next step.

This thesis is organized as follows:

The remainder of this chapter introduces the current state of research into single and two cylinder configurations, the mechanisms of interaction between two hydrokinetic turbines and the mechanisms of interaction between a turbine and its local environment. Chapter 2 introduces and reviews the theory behind the RANS and LES turbulence modelling techniques, and the turbulence models which

are used within the literature for simulating the flow around two kinetic turbines. Chapter 3 investigates the characteristics of the flow field around a single and two cylinders. The single cylinder simulations are performed due to the large amount of comparative experimental data available in the literature, which facilitates the development and validation of the CFD code based on the OpenFOAM platform. Chapter 4 presents the numerical simulations and water channel experiments for the two airfoil configurations. Chapter 5 presents the RANS simulations and analysis of the interactions between two rotating turbines. Finally, in Chapter 6, the major findings of this research are concluded and extended research subjects for future studies are discussed, understanding that this research can only provide a limited contribution to this difficult and challenging topic.

1.3 Single cylinder flow

Flow around a single cylinder is considered to be one of the fundamental problems of fluid mechanics as a complete solution requires the understanding of numerous fluid concepts, encompassing boundary layer, free shear flow and wake dynamics. In literature, extensive studies are reported which analyze the wake and properties of the flow around a cylinder as seen in references [11–15]. While a large range of Reynolds numbers are examined within the literature, a significant number of studies tend to focus on the Reynolds number $Re = 3,900$ due to the comprehensive dataset published by Lourenco and Shih [16].

From an experimental perspective, hot-wire anemometry measurements are relatively few, as measurements in the near wake region of a single cylinder are difficult due to the presence of the large re-circulation region located directly downstream of the cylinder. Despite the potential problems in obtaining measurements, Ong and

Wallace [12] are able to accurately measure the velocity and vorticity statistics in the range of $3 < x/D < 10$ using a complex probing mechanism. While many other studies are performed using hot-wire anemometry, none are able to provide any accurate turbulence statistics [13]. To avoid the restrictions associated with hot-wire anemometry, Lourenco and Shih [16] performed one of the first particle image velocimetry experiments for flow around a cylinder. The new measurement technique allows for the turbulent statistics to be captured much closer to the cylinder, at about $x/D = 1$, compared to the results of Ong and Wallace [12]. Due to the quality of the results obtained by Lourenco and Shih [16], their results are now used as one of the primary sources of validation for many numerical studies including [11, 13, 17–19].

In their LES study of single cylinder flow at $Re_D = 3,900$ defined based on the cylinder diameter, D, and mean freestream velocity, U_∞, Beaudan and Moin [11] solve the filtered Navier-Stokes equations using fifth-order upwind-biased and sixth-order centred finite difference schemes for the discretization of the convective and viscous terms respectively. While the turbulence statistics obtained by Beaudan and Moin are in reasonable agreement with the experimental results from Lourenco and Shih [16], within and outside of the re-circulation region, some important discrepancies are noted. Beaudan and Moin attribute these discrepancies to the experiments of Lourenco and Shih concluding that the disagreement is caused by flow perturbations within the experiments. Breuer [18] studied the numerical and modelling parameters that influence the quality of the LES solutions at $Re_D = 3,900$ and concluded that turbulence models with less dissipative numerical schemes, and to a lesser degree, with the dynamic rather than the fixed-coefficient Smagorinsky model, are able to improve the results. Later on, Mittal [20] performed LES of the same flow using second-order numerical methods with a central difference scheme and obtained results in reasonable agreement with existing numerical data, however, they still obtained disagreements

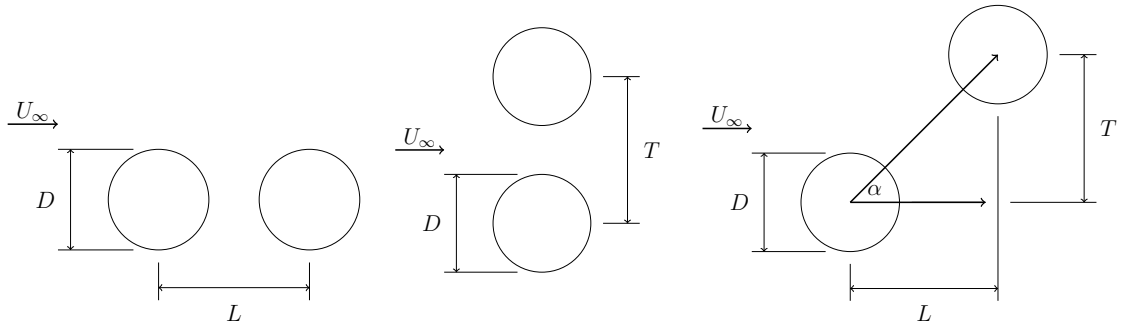

(a) tandem (b) side-by-side (c) staggered

Figure 1.3: Two cylinder configurations where D = diameter, L = streamwise spacing, T = spanwise spacing

with Lourenco and Shih's data in the re-circulation region. Recently, Ma *et al.* [17] investigated the predictive accuracy of LES by comparing the LES results with experimental and Direct Numerical Simulation (DNS) data in the Reynolds Number range $500 < Re_D < 5,000$. They are able to conclude that the spanwise domain length influences the convergence of the mean velocity profiles.

1.4 Two cylinder flow interactions

For the flow around two circular cylinders, there are three possible cylinder configurations: tandem, side-by-side and staggered, as shown in Figure 1.3. In the case of infinite length cylinders, the most important variables governing the fluid flow behaviour are the cylinder spacing, the cylinder's configuration and the Reynolds number.

As shown in Figure 1.3, two cylinders are considered to be in a staggered configuration when there are both vertical and horizontal separation distances between the two cylinders. For side-by-side cylinders, if the cylinders are positioned close to each other they behave as a single bluff body, moderately spaced cylinders experience wake interactions and widely spaced cylinders behave independently of each other.

Staggered cylinders behave similar to the side-by-side configuration in terms of the interactions experienced as a function of the separation distance, however, moderately spaced staggered cylinders can experience both wake and proximity interactions. Due to the complexity of the flow, the current focus of the literature is on attempting to classify the behaviour of the flow around two cylinders using a variety of different approaches based on a combination of theory, measurements and observation of the flow.

The simplest method for the classification of the flow around two cylinder configurations is the approach applied by Zdravkovich [21]. Zdravkovich classifies the behaviour of the flow into two separate categories based on the type of interference experienced between the two cylinders: wake and proximity interferences. Wake interference occurs when one of the cylinders becomes partially or completely submerged within the wake of the other cylinder. Proximity interference occurs when the two cylinders are located close enough to each other to ensure the wakes are interacting but when neither cylinder is located directly within the wake of the other cylinder.

The classification of two cylinder flows has also been developed substantially through the interpretation of experimental data. The classification of the cylinders is generally based upon the vortex shedding frequencies, the pressure coefficients and the force coefficients around the cylinders. These characteristics are typically examined as they can be conveniently acquired for different cylinder arrangements and Reynolds numbers. Other classifications based upon flow visualization techniques have provided important insights into the flow patterns of many different cylinder configurations [22–24].

Numerical modeling has only recently gained popularity due to the increased efficiency of high-quality turbulence modelling techniques such as LES and DNS, which can accurately predict the vortex shedding interactions behind the cylinders. Even so, as

Table 1.2: Examination of numerical studies around two cylinders

Authors	Title	Simulation	Reynolds Number (Re_D)	Parameters Examined	Results	Ref
J. Shao C. Zhang	Large eddy simulations of the flow past two side-by-side circular cylinders	LES of the flow around two side-by-side cylinders separated by $T/D = 1.5$ and 3.	5.8×10^3	Velocity, Turbulence, T/D, C_D, C_L	For $T/D = 3$ antiphase vortex streets are observed by LES. For $T/D = 1.5$ two different deflected gap flows are observed and the gap flow is unstable and switches intermittently. High computational requirements.	[25]
K. Kahil S. Benhamadouche P. Sagaut	Fine large eddy simulation of the flow around one and two side-by-side infinite cylinders at subcritical Reynolds numbers	LES of the flow around two side-by-side cylinders with $T/D = 1.5$.	3×10^3	Velocity, Turbulence, St, C_D, C_L	Observed bi-stability in the results. Two vortex shedding frequencies detected: $St = 0.1$ and 0.4. Insufficient computational time resolve the two flow regimes.	[26]
I. Afgan Y. Kahil S. Benhamadouche P. Sagaut	Large eddy simulation of the flow around single and two side-by-side cylinders at subcritical Reynolds numbers	LES of the flow around two side-by-side cylinders with $T/D = 1.5$	3×10^3	Velocity, Turbulence, St, C_D, C_L	Bi-stability is found to be intermittent and highly dependent on the gap flow vortices. Deflection of the flow is found to be away from the wide wake and towards the narrow wake. The narrow wake shows higher drag coefficients.	[27]
C. Ng N. Ko	Flow interaction behind two circular cylinders of equal diameter - a numerical study	Flow around two side-by-side cylinders modelled using the discrete vortex method for varying T/D ratios	5.6×10^3	Velocity, Turbulence, T/D, C_D, C_L	A single vortex street is obtained for $T/D = 1.25$, 3.0 and 3.5. Bi-stable flow is obtained for $T/D = 1.75$. The development of the downstream wake depends upon a series of vortex amalgamation processes. The maximum force coefficients are higher than a single cylinder.	[28]

most of the experimental studies available in the literature are all performed at high Reynolds numbers, which are not easily simulated through a numerical approach due to the high computation costs, numerical studies struggle with obtaining validated results. Table 1.2 presents the results from the few numerical studies for the side-by-side configuration in which $Re_D > 1,000$.

As the focus of this thesis is on the interactions between two hydrokinetic turbines, many of the parameters examined within the literature for the classification of two cylinder flows contain little or no relation to the performance of two hydrokinetic turbines. Consequently, this thesis will focus on the topics relevant to the interactions between two hydrokinetic turbines: the wake interactions and the lift and drag coefficients around the cylinders. Studies on the examination of the wake interactions between two-cylinder configurations are rather limited in the literature. Table 1.3

presents the results from several different studies examining the lift and drag forces acting on two side-by-side and staggered cylinders. The tandem configuration provides little insight into the hydrokinetic turbine interactions and shall not be discussed further. As can be seen from Table 1.3, for cylinders within the side-by-side configuration, the drag forces increase as a function of T/D until the cylinders behave independently of each other [24]. For cylinders within staggered configurations, the variation of the lift and drag forces depends significantly upon the cylinder spacing. For closely spaced staggered cylinders, significant variations to the force coefficients can occur with small changes in the incidence angle α. With moderately spaced staggered cylinders, the force coefficients become significantly less dependent on α, however, a substantial dependency still exists. Similar to the side-by-side configuration, widely spaced staggered cylinders behave independently of each other [24].

1.5 Turbine interactions

The interactions between two hydrokinetic turbines have a significant influence on turbine performance. Owing to the assumption of incompressible flows, the data from wind turbines is also examined. This section focus on reviewing experimental studies as very limited numerical data exists on the topic.

From Table 1.4, it can be seen that the presence of an upstream hydrokinetic turbine has a significant impact on the performance of a secondary downstream kinetic turbine. The performance reduction of the downstream turbine can be attributed to the turbulence generated by the upstream device, but more importantly, to the flow attenuation caused by the upstream device. Increasing the spanwise spacing can minimize the performance losses of the downstream turbine as the turbulence

Table 1.3: Experimental examination of force coefficient studies around two cylinders

Author	Title	Experiment	Reynolds Number (Re_D)	Parameters Examined	Results	Ref
M. Alam M. Moriya H. Sakamoto	Aerodynamic characteristics of two side-by-side circular cylinders and application of wavelet analysis on the switching phenomenon	Flow past two side-by-side cylinders using constant temperature anemometry in a wind tunnel	350 and 5.5×10^4	C_D, C_L, C_p, St, T/D	For $T/D = 0.5$, a minimum drag coefficient is observed. For $T/D = 1.2$ to 1.5 gap flow pattern is biased. For $T/D = 1.5$ both cylinders experience the same drag and lift coefficients.	[29]
P. Bearman A. Wadcock	The interaction between a pair of circular cylinders normal to a stream	Flow past two side-by-side cylinders using constant temperature anemometry in a wind tunnel	2.5×10^4	C_D, C_L, C_p, St, T/D	For $T/D = 1$, $C_D = 1.62$ and $C_L = 1.13$. For $T/D = 1.5$, $C_D = 1.29$ and $C_L = 0.34$. For $T/D = 2.0$, $C_D = 1.40$, $C_L = 0.22$.	[30]
D. Biermann W. Herrnsten Jr.	The interference between struts in various combinations	Experimental analysis in a wind tunnel to determine the interference drag between two streamlined struts and two circular cylinders	6.1×10^4 and 1.5×10^5	C_D	Interference drag can surpass the drag associated with the struts themselves. When $T/D > 5$, no interference of the wakes is observed. For various α, the interference drag between the cylinders can be considered negligible.	[31]
D. Sumner M. Richards O. Akosile	Two staggered circular cylinders of equal diameter in cross-flow	Experimental analysis of two cylinders in cross-flow with varying pitch ratios, P/D, from 1.125 to 4 using constant temperature anemometry in a wind tunnel.	3.2×10^4 and 7.4×10^4	C_D, C_L, C_p, St, P/D, α	A tandem configuration results in a minimum C_D. A large variation in C_D and C_L with α occurs for $P/D = 1.125$ to 1.25. When P/D increases the dependence of C_D and C_L with α decreases until at $P/D = 3.0$ two cylinders behave independently.	[32]
D. Sumner O. Akosile	Staggered circular cylinders immersed in a uniform planar shear flow	Examination of flow around two cylinders in a uniform plane shear flow using constant temperature anemometry in a wind tunnel	5×10^4	C_D, C_L, C_p, St, P/D, α, K	For $K = 0$ and $P/D = 1.125$ to 1.25, C_D and C_L are significantly different from single cylinder case. For $K = 0.05$, C_D decreases for all α. At lower α, the influence of shear is reduced.	[33]
D. Sumner M. Richards	Some vortex-shedding characteristics of the staggered configuration of circular cylinders	Examination of two cylinders with $P/D = 2.0$ to 2.5 and varying α, 0° to 90° using constant temperature anemometry in a wind tunnel.	3.2×10^4 to 7.0×10^4	C_D, C_L, St, P/D, α	The maximum inward directed lift forces and the maximum drag forces are experienced for $\alpha = 2^\circ$ to 15° at a wide range of Reynold numbers.	[34]
M. Alam H. Sakamoto Y. Zhou	Determination of flow configurations and fluid forces acting on two staggered circular cylinders of equal diameter in cross-flow	Examination of two staggered cylinders in cross flow using constant temperature anemometry in a wind tunnel.	5.5×10^4	C_D, C_L, C_p, P/D, α	For small T/D values, the lift force is dependent primarily on the size of the separation gap. Maximum C'_D occurs at $\alpha = 10^\circ$ for $T/D = 2.4$ to 3.0. The minimum C'_L is 0.78, occurs at $\alpha = 25^\circ$ for $T/D = 2.1$ to 5, and is due to vortex interactions.	[35]

and wake are dissipated into the free-stream. The streamwise spacing of kinetic turbines is also known to influence the performance of the devices, as decreasing the streamwise spacing increases the interactions between the turbines and creates a blockage effect which can cause a velocity increase of the fluid passing through

the device; consequently causing a potential performance increase in the hydrokinetic turbine [36].

In Table 1.4, the effects of wind and hydrokinetic turbine rotation and co-rotation against counter-rotation, are also examined. The examination tends to focus on horizontal axis turbines due to the lack of available data for vertical axis turbines. As obtaining two full-scale hydrokinetic turbines on which to perform results is challenging these studies were all numerical and obtained mixed results with several studies claiming a 1 to 3% performance increase, to others claiming no statistically significant performance increase. In Table 1.4, the interactions between the boundary layer and support structures are also examined, however, including these interactions within a numerical simulation provides significant challenges and these interactions should not significantly influence the relative performance differences between co-rotating and counter-rotating turbines. Thus, these interactions are ignored for the remainder of this thesis.

1.6 Relationship between turbine performance and drag in vertical-axis hydrokinetic turbines

In most fluid dynamics applications, the drag force is defined as the forces opposing the relative motion of any object moving with respect to a surrounding fluid. The drag force is defined as

$$F_D = \frac{1}{2}\rho U^2 S C_D \tag{1.1}$$

where U is the relative velocity between the object and flow, S is the wetted area, and C_D is the drag coefficient. The power density is calculated as

Table 1.4: Examination interactions between two wind or hydrokinetic turbines

Author	Title	Experiment	Reynolds Number (Re_d)	Parameters Examined	Results	Ref
J. Dabiri	Potential order-of-magnitude enhancement of wind farm power density via counter-rotating vertical-axis wind turbine arrays	Effects of turbine spacing and the direction of rotation in the performance of Vertical Axis Wind Turbines (VAWT)	5×10^5 to 8×10^6	T/d, L/d, Rotational Direction, TKE	To maintain 90% of the performance a VAWT must be placed 3 to 5 turbine diameters apart in the spanwise direction and 6 to 10 diameters apart in the streamwise direction. A VAWT with rated power of 1.2 kW can achieve a power density of 1001 W/m^2 compared to a horizontal axis wind turbine (HAWT) with rated power of 3 MW has power density of 304 W/m^2.	[37]
R. Whittlesey S. Liska J. Dabiri	Fish schooling as a basis for vertical axis wind turbine farm design	Examination of the effects of individual VAWT on the performance of turbine arrays.	2×10^5 to 7×10^5	Array size (32x32, 16x16, 4x4), Array Performance Coefficient	Maximum array performance coefficient is 1.4. Compared to HAWT's configurations of VAWT's reduce land use and result in array power density increased greater than one order of magnitude.	[38]
M. Kinzel Q. Mulligan J. Dabiri	Energy exchange in an array of vertical-axis wind turbines	Examination of the flow field within an array of 18 counter-rotating VAWT's	7×10^5	Velocity, T/d, L/d, TKE	The distance required to recover 95% of the wind velocity is approximately $6d$ for a pair of VAWT and $4d$ for a single turbine. HAWTs require $14d$.	[39]
A. Goude S. Lundin M. Leijon	A parameter study of the influence of struts on the performance of a vertical-axis marine current turbine	Investigation into the influence of support struts on the performance of 6 and 3 bladed turbines.	5×10^5 to 9×10^5	Number of Struts, Turbine Efficiency, TSR	A 6 bladed turbine exhibited more drop off losses with TSR and more step losses caused by additional supporting struts.	[40]
R. Barthelmie S. Frandsen M. Nielson	Modelling and measurements of power losses and turbulence intensity in wind turbine wakes at Middelgrunden offshore wind farm	Examined the power losses and turbulence intensity of wind turbine wakes using experiments and the "Wind Analysis Analysis and Application Program"	3×10^7 to 7×10^7	Power, TI	Observed 10% power losses due to the turbine wake interactions and an increase of 20% in the TI along a row of 2 MW wind turbines. Simulated results differed from the experimental results, however, the selection of a climate model could account for the differences.	[41]
A. Birjandi J. Woods E. Bibeau	Investigation of macro-turbulent flow structures interaction with a vertical hydrokinetic river turbine	Examination of river measurements one turbine diameter upstream of a hydrokinetic turbine	8.5×10^8	Velocity, Turbulence, Integral Length Scales, TKE	Upstream measurements indicate a reduction in the mean velocity as the eddies breakdown into smaller sizes. The velocity drops by 20% at $x/D = 1$ and the TKE increases due to the negative velocity gradient upstream of the turbine.	[42]
K. Golecha T. Eldho S. Prabhu	Study on the interaction between two hydrokinetic Savonius turbines	Examination of the interactions between two hydrokinetic Savonius turbines	1.2×10^5	T/d, L/d, C_Q, Power, TSR	At a separation distance of $4d$, the turbines performed independently. The maximum power coefficients are $C_P = 0.137$ and 0.139 for $T/d = 4$. The maximum torque occurred at the same location.	[43]
A. Shingetomi Y. Murai Y. Tasuka Y. Takeda	Interactive flow field around two Savonius turbines	Examination of the flow field around two Savonius turbines in close proximity using Particle Image Velocimetry (PIV)	1.07×10^4	Velocity, Power, Phase Angle	The interaction mechanism between two Savonius turbines is determined for two cases and four locations of positive coupling, arrangements resulted in the turbine performance exceeding that of a single turbine.	[44]
L. Myers A. Bahaj R. Rawlinsson-Smith M. Thompson	The effect of boundary proximity upon the wake structure of horizontal axis marine current turbines	Numerical simulation based upon an established wind turbine wake model to examine boundary layer interactions	1×10^5	Velocity, Turbulence, TKE	The close proximity of the seabed causes the wake to persist further downstream. Close proximity of boundary surfaces cause deviations and asymmetry within the wake.	[45]

$$P = \frac{1}{2}\rho U^3 A \tag{1.2}$$

where A is the cross-sectional or reference area of the turbine [46]. In actuality, however, when a kinetic turbine extracts power from the flow, the turbine causes a reduction in the energy of the surrounding fluid associated with a pressure difference across the turbine, creating an increase in the pressure at the leading edge (inlet) of the turbine and a decrease in the pressure at the trailing edge of the turbine. The high local pressure located at the inlet causes upstream fluid to be diverted around the turbine decreasing the volume of fluid passing through the turbine consequently reducing the amount of power available to the turbine. As more power is extracted, the pressure difference across the turbine increases further reducing the amount of fluid passing through the turbine, and gradually reaching a theoretical maximum amount of power that can be extracted from the fluid. The theoretical maximum is known as the Betz limit [47] and must be accounted for in the design of the turbine. The maximum power includes the Betz limit which now yields

$$P = \frac{1}{2}\eta\rho U^3 A \tag{1.3}$$

where η is referred to as the Betz limit. The maximum theoretical extractable power from a kinetic turbine is known to be simply a fraction, $\frac{16}{27}$ (or, 0.592). Obtaining the Betz limit, however, includes numerous assumptions which for practical applications cannot be assumed. By examining some of the parameters that influence the power generation of hydrokinetic turbines, Manwell *et al.* [48] proposed the following equation for the maximum power coefficient C_P. Practical hydrokinetic turbines have overall energy efficiencies water-to-wire of 0.35 for Darrieus [49].

$$C_P \approx 4a\left(1-a\right)^2 - \frac{1}{2}\frac{Bc}{R}C_D\lambda^3 \tag{1.4}$$

where a denotes an induction factor, B is the number of blades, λ is the tip speed ratio, R is the turbine radius and c is the chord length. As can be seen, the current form includes the drag coefficient and the number of blades within the turbines. By assuming negligible drag, and then optimizing the resulting relationship, the maximum power coefficient can be calculated as $\frac{16}{27}$, which is the Betz limit. From Equation 1.4, it is clear that the drag coefficient C_D provides one means to evaluate the performance of an actual hydrokinetic turbine with respect to its power coefficient C_P. Reducing the drag is the main approach to decrease the levelized cost of energy by optimally placing turbines in farms.

Chapter 2

Governing equations and turbulence models

Fluid motion is governed by the continuity and momentum equations, which take the following form for an incompressible fluid

$$\frac{\partial u_i}{\partial x_i} = 0 \tag{2.1}$$

$$\frac{\partial u_i}{\partial t} + u_j \frac{\partial u_i}{\partial x_j} = -\frac{1}{\rho}\frac{\partial p}{\partial x_i} + \frac{\partial}{\partial x_i}\left(\nu \frac{\partial u_i}{\partial x_j}\right) \tag{2.2}$$

where u_i represents the velocity, p is the pressure, ρ is the density and ν denotes the kinematic viscosity. There are three major approaches for solving the governing equations for turbulent flows. The first approach is to directly solve the governing equations over the entire range of temporal and spatial turbulent scales. This approach is referred to as DNS. When performing DNS a very fine mesh and small time steps are required in order to resolve the smallest turbulent scales. Although simple geometries at low Reynolds numbers can be solved using DNS, it is highly

impractical to apply DNS to very complex problems due to the large computational costs imposed by the mesh and time step requirements [50]. The second approach that is used to model turbulent flows is large eddy simulation. In LES, the large scale turbulent structures are resolved, whereas the small turbulent scales are filtered out and modelled through the use of turbulence models called SGS models [50]. The third approach used to model turbulent flows is the Reynolds averaged Navier-Stokes approach. In RANS, the governing equations are time averaged (or, ensemble averaged) before the application of numerical solution techniques. As only the mean quantities are needed due to the averaging procedure, the computational costs of RANS are significantly lower than both LES and DNS [10]. Currently, due to the computational requirements of both LES and DNS, the RANS turbulent modelling technique is typically used for most industrial applications. This thesis focuses primarily on the LES approach, however, due to the computational requirements involved in LES, the RANS approach is also considered.

2.1 Governing equations for LES

The main goal of LES is to obtain an accurate solution of turbulent flows but at significantly lower computational costs than DNS. As the major computational costs of DNS are related to resolving the small scales of the flow field, the objective of LES is to separate these computationally intensive scales of the flow. According to turbulence theory, the small scale eddies have a universal and isotropic behaviour that is independent of the flow boundary conditions. Therefore, a computational model can be used to describe their behaviour and to accurately reproduce the net effects without directly solving the flow at theses scales. While the computational costs of LES are significantly reduced due to the modelling procedure, the computational costs of LES are still relatively high compared to RANS. Owing to advances in

the computational hardware and parallel processing, the use of LES is becoming increasingly popular [50].

In LES, the large scales of motion are resolved, however, the small SGS are modelled. The resolved large scales and the SGS are differentiated using a low-pass spatial filter applied to the governing equations of fluid flow, and in the context of an incompressible flow, the filtered continuity and momentum equations take the following forms:

$$\frac{\partial \bar{u}_i}{\partial x_i} = 0 \tag{2.3}$$

$$\frac{\partial \bar{u}_i}{\partial t} + \frac{\partial}{\partial x_j}\left(\bar{u}_j \bar{u}_j\right) = -\frac{1}{\rho}\frac{\partial \bar{p}}{\partial x_i} + \nu \frac{\partial^2 \bar{u}_i}{\partial x_j \partial x_j} - \frac{\partial \tau_{ij}}{\partial x_j} \tag{2.4}$$

where $\bar{u}_i$ and $\bar{p}$ represents the filtered velocity and pressure, respectively. As a consequence of the filtering process, the so-called SGS stress tensor appears in the filtered momentum equation, which is defined as $\tau_{ij} \stackrel{\text{def}}{=} \overline{u_i u_j} - \bar{u}_i \bar{u}_j$ and needs to be modelled in order to close the above system of governing equations.

2.1.1 Sub-grid scale stress models

In order for LES models to successfully and accurately simulate turbulent flows, the SGS model must accurately reproduce the effects of the small eddies. Many SGS models have been proposed during the past few decades and studies have been performed examining the performance of such models. Two SGS stress models are used in this research: namely, the conventional Smagorinsky model (SM) [51] and the Dynamic Smagorinsky model (DSM) of Lilly [52] which are now presented.

(1) Smagorinsky Model

The SM is based upon the equilibrium hypothesis which assumes that the small scales adjust quicker to flow perturbations because they contain shorter time scales than the large eddies. Under the equilibrium hypothesis, the viscous dissipation, is related to the SGS stress according to the relationship $-\tau_{ij}\bar{S}_{ij} = \epsilon$. By rewriting the eddy viscosity in terms of the strain-rate tensor and an unknown constant C_s, the following equation for modeling the SGS viscosity ν_T is obtained [51].

$$\nu_T = \left(C_s\bar{\Delta}\right)^2 |\bar{S}| \tag{2.5}$$

where $|\bar{S}| = (2\bar{S}_{ij}\bar{S}_{ij})^{1/2}$ is the norm of the resolved strain rate tensor, $\bar{\Delta}$ is the fiters size, and C_s is the model coefficient. To evaluate the Smagorinsky constant C_s, the presence of an inertial-range spectrum $E(k) = C_K\epsilon^{2/3}k^{-5/3}$ is assumed. Letting ϵ represent the total dissipation over the entire region and letting the Kormogorov constant be $C_k = 1.41$, an approximation for $|\bar{S}|$ is obtained by integrating the dissipation spectrum over the entire range of wave numbers as shown, viz.

$$|\bar{S}|^2 = 2\int_0^{\pi/\bar{\Delta}} k^2 E\left(k\right) dk = \frac{2}{3}C_K\epsilon^{2/3}\left(\frac{\pi}{\bar{\Delta}}\right)^{4/3} \tag{2.6}$$

Under the equilibrium hypothesis, the solution to Equation 2.6 leads to a value of $C_s = 0.18$. In the presence of shear flow, the value of C_s is found to yield excessive damping, and consequently, values of 0.65 to 0.1 for C_s are common [53]. For instance, in the original paper of Smagorinsky, [51], the SM coefficient is set to $C_s = 0.167$.

(2) Dynamic Smagorinsky Model

The DSM proposed by Lilly [52] expresses the SGS stress tensor as

$$\tau_{ij}^* = -2C_S\bar{\Delta}^2|\bar{S}|\bar{S}_{ij} \quad , \tag{2.7}$$

where $\bar{\Delta}$ is the grid-level filter size, $\bar{S}_{ij} \stackrel{\text{def}}{=} (\partial \bar{u}_i/\partial x_j + \partial \bar{u}_j/\partial x_i)/2$ is the resolved strain rate tensor, $|\bar{S}| = (2\bar{S}_{ij}\bar{S}_{ij})^{1/2}$ is the norm of the resolved strain rate tensor, and $(\cdot)^*_{ij} = (\cdot)_{ij} - (\cdot)_{kk}\delta_{ij}/3$ denotes the trace-free format of a tensor. Here, δ_{ij} is the Kronecker delta. The optimal dynamic model coefficient C_S is obtained using the least squares method, viz.

$$C_S = -\frac{M_{ij}\mathcal{L}_{ij}}{M_{ij}M_{ij}} \quad , \tag{2.8}$$

where $\mathcal{L}_{ij}$ is the resolved Leonard type stress defined as $\mathcal{L}_{ij} \stackrel{\text{def}}{=} \widetilde{\bar{u}_i\bar{u}_j} - \tilde{\bar{u}}_i\tilde{\bar{u}}_j$, and $M_{ij} \stackrel{\text{def}}{=} \alpha_{ij} - \tilde{\beta}_{ij}$ is a differential tensor. Here, $\alpha_{ij} \stackrel{\text{def}}{=} 2\tilde{\bar{\Delta}}^2|\tilde{\bar{S}}|\tilde{\bar{S}}_{ij}$ and $\beta_{ij} \stackrel{\text{def}}{=} 2\bar{\Delta}^2|\bar{S}|\bar{S}_{ij}$ are the test-grid and grid level base stress tensors, respectively. For the LES approach considered in this research, the resolved/filtered quantities at the grid level are denoted using an over-bar, while quantities filtered at the test-grid level for the dynamic procedure are denoted using a tilde.

2.2 RANS governing equations

In RANS, the governing equations are derived by decomposing the flow variables of the Navier-Stokes equations into mean and fluctuating components. An ensemble averaging procedure is then applied to the decomposed equations resulting in the RANS equations. In the context of an incompressible flow, the continuity and momentum equations take the following forms:

$$\frac{\partial \bar{u}_i}{\partial x_i} = 0 \tag{2.9}$$

$$\frac{\partial \bar{u}_i}{\partial t} + \frac{\partial}{\partial x_j}\left(\bar{u}_j\bar{u}_j\right) = -\frac{1}{\rho}\frac{\partial \bar{p}}{\partial x_i} + \nu\frac{\partial^2 \bar{u}_i}{\partial x_j \partial x_j} - \frac{\partial \tau_{ij}}{\partial x_j} \tag{2.10}$$

where $\bar{u}_i$ and $\bar{p}$ represents the averaged velocity and pressure respectively. As a

consequence of the averaging procedure, the so-called Reynolds averaged stress tensor, defined as $\tau_{ij} \stackrel{\text{def}}{=} \overline{u_i u_j}$, appears in the momentum equations and needs to be modelled in order to close the above system of governing equations. In this research, the k-ω-SST turbulence model is used for all RANS simulations. The k-ω-SST turbulence model has been shown to better predict the wake zone and near wall region near wall region around an airfoil [54].

2.2.1 k-ω-SST turbulence model

The k-ω-SST turbulence model (in Equation 2.11) proposed by Menter [55] is based upon two fundamental RANS turbulence models the k-ϵ and k-ω turbulence models. Complete descriptions of these turbulence models are found in Versteeg and Malalasekera [10]. By comparing the two fundamental RANS turbulence models, Menter noted that the results of the k-ϵ model are much less sensitive to the assumed free-stream values, meanwhile, the prediction of near wall turbulence under adverse pressure gradients is unsatisfactory compared to the $k-\omega$ model. In the k-ω-SST model, the computation of the Reynolds stress and the k-equation are the same as in the original k-ϵ model, however, the ϵ-equation is transformed into an ω-equation using the substitution $\epsilon = k\omega$, which reads

$$\frac{\partial(\rho\omega)}{\partial t} + \nabla\cdot(\rho\omega U) = \nabla\cdot\left[\left(\mu + \frac{\mu_t}{\sigma_{\omega,1}}\right)\nabla\omega\right] + \gamma_2\left(2\rho S_{ij}\cdot S_{ij} - \frac{2}{3}\rho\omega\frac{\partial U_i}{\partial x_j}\delta_{ij}\right) - \beta_2\rho\omega^2 + 2\frac{\rho}{\sigma_{\omega,2}}\frac{\partial k}{\partial x_k}\frac{\partial\omega}{\partial x_k} \tag{2.11}$$

The model constants are given as follows: $\sigma_k = 1$, $\sigma_{\omega,1} = 2$, $\sigma_{\omega,2} = 1.17$, $\gamma_2 = 0.44$ and $\beta_2 = 0.083$.

2.3 Comparison of turbulence models

There are many methods with which to simulate turbulent flow around a kinetic turbine which include empirical correlations, RANS, LES and DNS. While empirical models provide the simplest means with which to investigate the flow around turbines, the applications of such models are limited to a basic control volume analysis. DNS provides the most comprehensive description of the flow field, however, the computational costs of DNS are too high for most kinetic turbine applications and representative Reynolds numbers, $Re_d = 1 \times 10^6$ to 1×10^7 are too demanding computationally. Because of this, the most practical methods mentioned for analyzing kinetic turbines are the RANS and LES turbulence methods.

To put the computational costs of LES into perspective, based on the study of Choi and Moin [56], the nodal requirements of LES are on the order of $Re_{L_x}^{13/7}$ whereas the nodal requirements for DNS are on the order of $Re_{L_x}^{37/14}$. Based upon the computational requirements, LES performs calculations at Reynolds Numbers several orders of magnitudes greater than those of DNS [50], however, the computational costs are still high in comparison to RANS. While LES was known to struggle with unstructured meshing, transitional flows, relaminarized flows and separated flows numerous developments have significantly improved the performance of LES in these areas [57–59]. According to Bouffanais [60], for most industrial applications, the computational costs associated with LES outweigh the potential benefits of the method.

Table 2.1 provides a summary of several different CFD studies comparing the effectiveness of RANS and LES both quantitatively and qualitatively for the same test cases against each other. While there are numerous studies which compare the RANS and LES turbulence models, few studies perform direct comparisons of these turbulence models for turbine related applications and geometries. Even though most

Table 2.1: Comparison of LES and RANS turbulence models on identical test cases

Author	Title	Simulation	Reynolds Number	Parameters Examined	RANS Results	LES Results	Ref
S. Murakami	Current status and future trends in computational wind engineering	Literature Review	$Re \approx 10^4$	Flow visualization and computational time	Many models contain flaws such as over-predicting the k in stagnation regions which limit accuracy for flow around bodies	significantly more computational in the order of $2-30$ times that of RANS	[61]
W. Rodi	Comparison of LES and RANS calculations of the flow around bluff bodies	Flow around a square cylinder	2.2×10^4	U, TKE	RANS under-predicts periodic motions and the results. Simulation time for RANS was 2h	LES is able to decipher the flow details accurately. Simulation time for LES was 73h.	[62]
W. Rodi	Comparison of LES and RANS calculations of the flow around bluff bodies	flow around a surface mounted cube	4×10^4	U, TKE	RANS over-predicts the k in stagnation regions causing poor results compared to experiments.	Results from LES are quantitatively similar to experimental results.	[62]
Y. Cheng, F. Lien, E. Yee and R. Sinclair	A comparison of LES with a standard $k\epsilon$ RANS model for the prediction of a fully developed turbulent flow over a matrix of cubes	fully developed turbulent flow over a matrix of cubes	3.8×10^3	U, FV, Reynolds Stresses, TKE	LES captured all the flow features and provided a good quantitative agreement with experimental data. LES required 100 times the computational cost.	RANS overestimates the recirculation zone causing an increased boundary layer amongst other flow differences.	[63]
M. Caciolo, P. Stabat and D. Marchio	Numerical simulation of single-sided ventilation using RANS and LES and comparison with full-scale experiments	single-sided ventilation using both RANS and LES for two windward cases and one leeward case	—	FV, U, N	For the windward cases LES equals or exceeds the flow prediction of RANS. RANS over-predicts the strength and length of the mixing layers.	LES requires 30 times more computational power but produces better results. Largest difference in N for RANS is 49% compared to 33% for LES.	[64]
M. Caciolo, P. Stabat and D. Marchio	Numerical simulation of single-sided ventilation using RANS and LES and comparison with full-scale experiments	Simulation of a single-sided ventilation using both RANS and LES for leeward case	—	FV, U, N	For the leeward case the results from LES and RANS are very similar, LES has a slightly improved turbulence prediction compared to RANS.	LES requires 30 times more computational power but produces better results. Largest difference in N for RANS is 49% compared to 33% for LES.	[64]
I. Afgan, J. McNaughton, S. Rolfos, D. Apsley, T. Stallard and P. Stansby	Turbulent flow and loading on a tidal stream turbine by LES and RANS	Simulation of turbulent flow and loading on a tidal stream turbine by LES and RANS	1.2×10^5	U, TKE, P, TI, C_p	C_p predicted to within 3% for LES all TSR. RANS predicts C_p to within 10% for $TSR < 6$ however matches LES at $TSR < 6$.	LES captures the blade tip vortices and interactions with the supporting structures. RANS under-predicts the TKE and suction pressure. Does not predict the thrust and torque as well as LES.	[65]
C. Li, S. Zhu, Y. Xu and Y. Xiao	2.5D large eddy simulation of vertical axis wind turbine in consideration of high angle of attack flow	Comparison of LES and URANS with experimental results for a VAWT with high AOA	3×10^5	FV, C_D, C_P, C_T, C_N, C_p	RANS overestimates C_T and delays dynamic stall leading to results which substantially deviate from experimental results.	LES has excellent agreement with experiments at low TSR and approximates the flow better than URANS at higher TSR though it does deviate from the experimental results.	[66]

studies examine different geometries, the results from these studies are examined in order to understand the potential advantages and disadvantages of the RANS and LES turbulence models. In kinetic turbine applications, many different flow phenomena are present as the wake alone can possess re-circulation zones, stagnation zones, flow separation and reattachment zones. Therefore, the flow features examined within the studies are applicable to kinetic turbine applications.

As described within Table 2.1, RANS turbulence models are known to overpredict turbulent kinetic energy in stagnation zones, overpredict the size of re-circulation zones and under-predict periodic flow motions [61–63]. In his study, Cheng *et al.* [63] is unable to simulate the re-circulation zones located behind the matrix of cubes regions due to what he describes as problems in the fundamental assumptions used in creating the RANS turbulence model. The literature study of Murakami further reinforces the notion that LES is able to out-predict the RANS turbulence modelling technique.

Two of the studies listed in Table 2.1 involve the use of both RANS and LES for turbine applications and their results are consistent with previously noted investigations. Afgan *et al.* [65] examines the flow directly over a tidal stream turbine. Afgan is able to conclude that overall LES produces higher quality results compared to RANS simulations, however, at lower tip speed ratios (TSR), the RANS results are matched against the LES results. Li *et al.* [66] is more critical of the performance of RANS claiming that LES out-performed RANS substantially for vertical axis turbines with high angles of attack.

Tables 2.2 present studies using LES and RANS for kinetic turbines applications. Due to the turbulence modeling methods and the computational resources available to the different researchers, the Reynolds numbers varied from 1×10^5 to 1×10^7. Kang *et al.* [67] noted that to perform LES around horizontal marine turbine examining

only the turbine rotor at a Reynolds number of 4.5×10^5 required 800 cores to perform the simulations. In their study of two different wind turbine arrays using LES, Meyers and Meneveau [68] show a 5% improvement in the power coefficient for a staggered configuration in comparison to an aligned configuration. Turnock *et al.* [69] examine tidal turbine arrays using a RANS with a k-ω-SST turbulence model and also conclude that staggered configurations provide a performance increase. Gebrelassie *et al.* expand upon the research into staggered arrays and show that closely spaced turbines within the spanwise direction result in a performance increase due to an increase in the blockage ratio of the flow.

Table 2.2: Examination of LES turbulence models on hydrokinetic and wind turbines

Author	Title	Experiment	Reynolds Number (Re_d)	Parameters Examined	Results	Ref
Q. Guo, L. Zho, Y. Xiao and Z. Wang	Flow field characteristics analysis of a horizontal axis marine current turbine by large eddy simulation	LES simulation of a horizontal axis marine turbine using LES with an actuator disk turbine model for flow field visualization	$Re_d \approx 1.2 \times 10^6$	Velocity field	LES captured the spiral vortices developing from the blade tip and the non-uniformity of the flow upstream and downstream caused by the discrete number of blades.	[70]
S. Kang, I. Borazjani, J. Colby and F. Sotiropoulos	Numerical simulation of 3D flow past a real-life marine hydrokinetic turbine	LES simulation of a horizontal axis marine turbine using only the turbine rotor	$Re = 4.5 \times 10^5$ and 6.0×10^5	Velocity field, pressure coefficients	LES captures wake contains three main regions containing spiral tip vortices. For $U_{\text{inf}} = 1.5$, LES predicts $C_p = 0.282$ compared to experimental value $C_p = 0.296$. Simulation used up to 185 million nodes and 800 cores.	[67]
M. Calaf, C. Meneveau and J. Meyers	Large eddy simulation study of fully developed wind-turbine array boundary layers	Numerical simulation of a wind turbine array using LES with a drag disk turbine model	High Re	Velocity field, roughness height, TKE	LES simulation predicts vertical TKE fluxes of the same order of magnitude as the power extracted from the turbines. LES simulation yields larger roughness heights than those predicted by the Frandsen empirical correlation.	[71]
Y.T. Wu and F. Port-Agel	Large-eddy simulation of wind-turbine wakes: evaluation of turbine parameterizations	Numerical simulation of a wind turbine using LES with both actuator disk and rotating actuator disk turbine models	High Re	Velocity Field, TI	LES a velocity minimum at $x/D = 5$. LES provides good velocity and TI agreement with experimental results. The simulation accuracy limited by the turbine model and not the LES turbulence model.	[72]
A. Jimenez, A. Crespo, E. Migoya and J. Garcia	Advances in large-eddy simulation of a wind turbine wake Numerical simulation of a wind turbine using LES and a drag forces turbine model.	LES simulation of the flow around a wind turbine	$Re \approx 2 \times 10^7$	Velocity field, TI	Every component of the Reynolds Stress tensor was in good agreement with analytical data of [73]. Results indicate that even using rotor simplifications the LES model can simulate the turbulent wake characteristics. LES provides detailed flow oscillations and eddy scales.	[74]
J. Meyers and C. Meneveau	Large Eddy Simulations of large wind-turbine arrays in the atmospheric boundary layer	Numerical simulation of two wind turbine arrays with different turbine configurations using LES and an actuator disk turbine model		Force coefficients, flow field	LES showed that the staggered arrays yielded 5% more power compared to aligned arrays. Tangential forces had the largest impact on the mean streamwise velocity.	[68]
M. Gebreslassie, G. Tabor and M. Belmont	Numerical simulation of a new type of cross-flow tidal turbine using OpenFOAM - Part II: Investigation of turbine-to-turbine interaction	Numerical simulation of a cross-flow tidal turbine using the immersed body force turbine model		Turbine power and spacing	LES results indicate laterally close turbine to turbine interactions could improve performance due to blockage effect. Sufficient spacing required in the longitudinal direction to minimize power losses.	[75]
X. Bai, E. Avital and J. Williams	Numerical simulation of a marine current turbine in free surface flow	Numerical simulation of marine current turbine using an immersed body force turbine model	$Re = 1.38 \times 10^6$	Power coefficients and rotational speed	Compared the power coefficients from the numerical simulations to experimental results and obtain good agreement between the results. Minor deviations in the results can be attributed to the grid resolution.	[76]

M. Churchfield, Y. Li and P. Moriarty	A large-eddy simulation study of wake propagation and power production in an array of tidal-current turbines	LES simulation of a tidal turbine array with an actuator line turbine model examining the effect of rotation.	—	Velocity field, power	LES showed an average maximum relative power of $1.041J$ for the case of all turbines rotating clockwise. Counter-clockwise rotation caused a 3% increase and cross-stream spacing has little effect. LES provided useful unsteady information about wakes and power.	[77]
J. McNaughton, F. Billard and A. Revell	Turbulence modelling of low Reynolds number flow effects around a vertical axis turbine at a range of tip-speed ratios	RANS simulation using a SST model around vertical axis turbine	$Re_C = 1.5 \times 10^5$	Skin friction and power coefficients, flow field	$k-\omega$ SST model significantly overpredicts the power coefficient however the low Reynolds model correctly predicts the laminar separation which allows the correct reproduction of the flow characteristics agreeable with LES results	[78]
T. Maitre, E. Amet and C. Pellone	Modeling of the flow in a Darrieus water turbine: Wall grid refinement analysis and comparison with experiments	2D RANS of a Darrieus cross-flow marine turbine using ANSYS-Fluent	$Re_C = 1.2 \times 10^5$	y^+, power coefficient, flow field	Computed power is significantly lower than the experimental data and at lower TSR the power curve differs significantly. The $2D$ model does not adequately represent the dynamic stall in the turbine.	[79]
S. Turnock, A. Phillips, J. Banks and R. Nicholls-Lee	Modelling tidal current turbine wakes using a coupled RANS-BEMT approach as a tool for analyzing power capture of arrays of turbines	Simulation of a tidal turbine using RANS-BEMT turbulence modelling and a coupled blade momentum approach	$Re_d \approx 4 \times 10^7$	Power coefficient, separation distance, flow field	Minimizing the lateral spacing with a small number of staggered rows spaced longitudinally as far apart as practical provided the best results. Wake growth is significantly dependent upon the mesh resolution when performing RANS.	[69]
I. Dobrev and F. Massouh	CFD and PIV investigation of unsteady flow through Savonius wind turbine	RANS and Detached eddy simulation (DES) simulation of the flow around a Savonius turbine using a SST turbulence model	$Re \approx 1.4 \times 10^5$ to 1.7×10^5	Velocity field	SST model produced results much higher than the experimental results. $3D$ SST model produced similar phase averaged velocities but did not match the instantaneous velocities. DES produced comparable results to the experimental data and the DES model enables accurate representation of the turbulence of the detached flow.	[80]
D. Gaden	An investigation of river kinetic turbines: performance enhancements, turbine modelling techniques and an assessment of turbulence models	RANS simulations to examine the influence of a diffuser on hydrokinetic turbines.	$Re \approx 1 \times 10^6$	Turbulence model, velocity field	SST models show a peculiar downward motion in the core of the wake and large asymmetry. Eddy-viscosity models show less asymmetry, but the asymmetry is larger than expected. Eddy-viscosity models do not show the recirculation zones at the trailing edge however RST contains some of the recirculation zones. RST predicts less turbulence than eddy viscosity and the two models produce entirely different flow structures. Errors in comparison to experimental data range from 2.2% to 99% and the large variation could be due to the inlet condition. Downstream tapering not observed in PIV data.	[81]

Chapter 3

Turbulent wake behind a single and two cylinders

The current chapter examines the influence of the SGS model for LES of the flow around a single cylinder with $Re_D = 3,900$ and the wake interactions between two buff bodies by examining staggered and side-by-side cylinder arrangements with $Re_D = 3,000$ as shown in Figure 1.3 on page 9. For side-by-side cylinders, the spanwise separation distance is set to $T/D = 1.5$, and for the staggered cylinders, the spanwise and streamwise separation distances are set to $T/D = 1.5$ and $L/D = 1.5$, respectively. The simulations are performed using the wall-resolved LES approach with two sub-grid scale stress models. The streamwise evolutions of the velocity profiles of the single, side-by-side and two staggered cylinders are then compared. The dynamics of the turbulent wake flows and their interactions behind the cylinders are investigated by examining the first- and second-order velocity statistics, the pressure and force coefficients around the surface of the cylinders, vortex shedding frequencies and the energy spectrum. Table 3.1 shows the computational test matrix for the current chapter.

Table 3.1: Computational matrix for a single and two cylinders

Case	Reynolds Number	L/D	T/D	Why
Single cylinder	3,900	—	—	Test two SGS models—the SM and DSM—and determine which model provides the best prediction of the flow. Compare the results to experimental results available in the literature.
Side-by-side cylinders	3,000	1.5	0	To gain an understanding of the influence of positioning and wake interactions on the resolved flow field and the drag coefficients.
Staggered cylinders	3,000	1.5	1.5	To gain an understanding of the influence of positioning and wake interactions on the resolved flow field and the drag coefficients.
Details				
All simulations are performed using OpenFOAM v2.3.0 using wall-resolved LES with explicit filtering. To ensure accurate results a minimum grid resolution of $\Delta x^+ < 30$, $\Delta y^+ < 1$ and $\Delta z^+ < 30$ is used throughout all the simulations. The side-by-side and staggered simulations are performed using the SM model.				

LES of the wake and vortex dynamics in turbulent flow around circular cylinders represents an interesting and challenging topic in computational fluid dynamics. There are many important applications of cylinder flows in engineering practice, e.g. the flow inside a shell-tube heat exchanger and wind field around a symmetrical building structure. The challenge of this type of study comes from the need for an improved understanding of the physics of the flow and dynamic interactions of different types of turbulent structures triggered by buff bodies, which in turn imposes further challenges to the numerical simulations in terms of turbulence modelling and predictive accuracy. The interaction of the wake behind cylinders represents an important topic, as the physics can provide an understanding of the interactions between two airfoils applicable in hydrokinetic turbines.

In this chapter, the velocities $\langle \bar{u} \rangle$ and $\langle \bar{v} \rangle$ are non-dimensionalised by U_∞ and the Reynolds stresses $\langle \bar{u}'\bar{u}' \rangle$ and $\langle \bar{v}'\bar{v}' \rangle$ are non-dimensionalised by U_∞^2; the averaged statisitics are collected over a minimum averaging period of 40 vortex shedding periods. Furthermore, during the initial stages of the simulation the solutions of the velocity and pressure feilds do not fully satisfy the governing equations and any unphysical initial conditions are not taken into account.

3.1 Computational domain and boundary conditions for cylinders

As the majority of the CFD simulations use an unstructured grid for RANS simulations with an upwind numerical dissipation scheme for discretizing the convection term, few simulations exisit for LES based on unstructured grids. LES cannot use the upwind numerical dissipation scheme due to suffering from accuracy losses associated with the scheme and the exact effects of unstructured grids on the simulations are still relatively unknown [50]. Most LES simulations tend to use structured grids in which the results have been well documented [57]. For flow around a single cylinder, the most common types of grids are structured O-grid, and C-grids and the exact selection of a grid system depends of the shape and size of the domain.

For the cylinder cases, the computational domains consist of a rectangular domain with an O-grid mesh encompassing a small region around the cylinders. Due to the implicit filtering methods used to generate the governing equations, the filter size is directly related to the grid resolutions and refining the grid causes the simulations to become closer to DNS [50]. Consequently, for LES with implicit filtering no accepted method exist to test grid independence, however, Piomelli [50] suggests that for wall-resolved LES that the grid resolution needs to satisfy $\Delta x^+ < 150$, $\Delta y^+ < 2$ and $\Delta z^+ < 30$. For all the cylinder LES simulations, the grid spacings are set such that $\Delta x^+ < 30$, $\Delta y^+ < 1$ and $\Delta z^+ < 30$. For the single cylinder validation case, the domain width is set to be $5D$ and the cylinder is positioned along the centerline of the domain, $5D$ downstream from the inlet, $5D$ away from the top and bottom sides and $15D$ upstream of the outlet. The dimensions of the computational domain are selected to ensure that the boundaries are sufficiently far away from the cylinder such

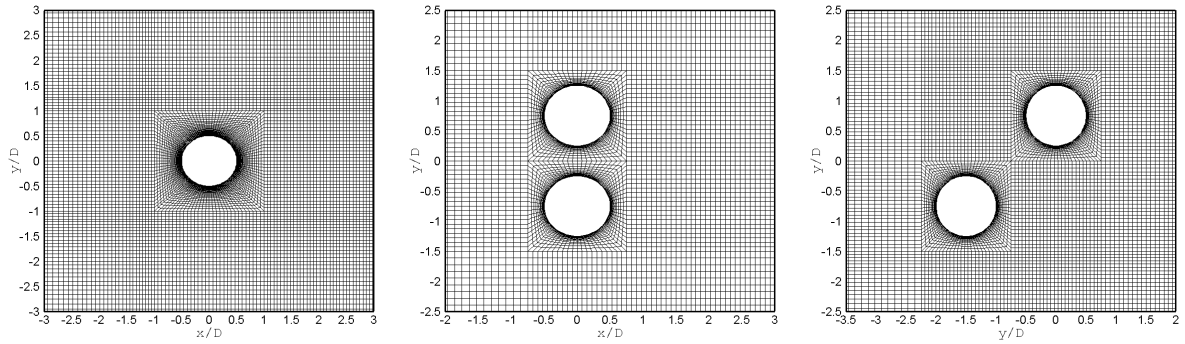

(a) Single cylinder (b) Side-by-side cylinders (c) Staggered cylinders

Figure 3.1: Snapshots of the meshes for the cylinder configurations

that the impact from the boundary conditions does not significantly affect the wake within any regions of interest. Figure 3.1 shows the computational domains for all the cylinder simulations.

As shown in Figure 3.1, for the staggered and side-by-side cylinder configurations the mesh remains similar to the single cylinder validation case. The changes between the two cylinder meshes compared to the single cylinder include the addition of a secondary O-grid, an increase in the computational domain size to accommodate two obstructions, and some slight refinement of the mesh in the near wall region of the wake to ensure the wake interaction point is accurately captured. No turbulent intensity is added to the inlet velocity as Breuer [18] determined that the fine mesh near the surface of the cylinders would dampen out these fluctuations causing no influence on the wake results. At the outlet, a zero gradient boundary condition is applied. Wall, no-slip, boundary conditions are applied to the surface of each cylinder with the normal and tangential velocity components of the flow are set to zero. For the front, back, top and bottom sides cyclic boundary conditions are applied. Cyclic boundary conditions are quasi-similar to the symmetry boundary conditions as both types of boundary conditions are used on repeating flows, however, symmetry boundary conditions assume that no flow nor scalar flux can cross the

boundary and function only for a single repeating pattern crossing a boundary. Cyclic boundary conditions allow the flow to pass through the boundary and function for multi-repeated patterns.

3.2 Cylinder results

In this subsection, the results of LES for the single cylinder, side-by-side cylinders and staggered cylinder flows are presented. The analysis examines the first- and second-order velocity statistics, the pressure and force coefficients around the surface of the cylinders, vortex shedding frequencies and the energy spectrum. For the single cylinder case, the results of the simulations are primarily compared quantitatively and qualitatively against the experimental results of Lourenco and Shih [16] within the near wall region and the experimental results of Ong and Wallace [12] in the far wall region. The effects of the SGS model is also examined for the single cylinder simulation by comparing the results from the SM and DSM models. For the two cylinder configuration, based on an extensive literature review, the experimental studies are either performed at high Reynolds numbers greater than $10,000$ or present no data which can be quantitatively compared. There are a few numerical simulations for the side-by-side case and the results will be compared to these studies when applicable. No comparative data is available in the open literature for the staggered case. The lack of such data is indicative of the significant contribution remaining to optimise hydro-kinetic turbine farms.

3.2.1 Validation case: single cylinder

Figure 3.2 shows the instantaneous velocity $\bar{v}/U_\infty$, for the flow around a single cylinder. Besides showcasing the wake region and the signature alternating vortex

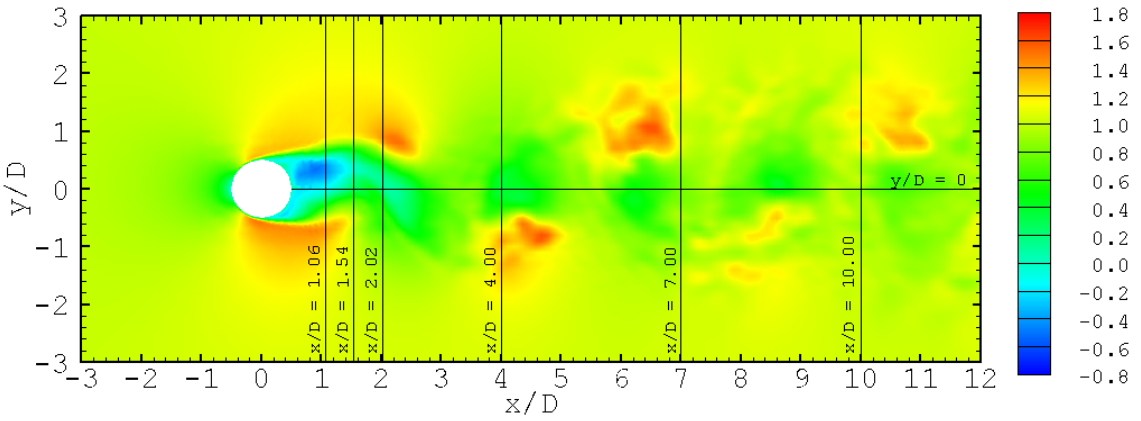

Figure 3.2: Instantaneous streamwise velocity $\bar{u}/U_\infty$ for the flow around a single cylinder using the SM at time $tU_\infty/D = 585$. The six cutting lines and centreline in the figure are used throughout the analysis of the flow around a single cylinder.

shedding pattern of a cylinder, Figure 3.2 presents the locations of 6 cutting lines which are used during the analysis of the flow around a single cylinder. Additional contour plots of the flow around a single cylinder are available in Appendix A.

To qualitatively analyse the differences between the turbulence models, Figure 3.3 displays the non-dimensional mean streamwise velocity $\langle\bar{u}\rangle/U_\infty$ within the central spanwise plane, $y/D = 0$. The negative velocity observed in the immediate vicinity behind the cylinder reflects the presence of the recirculation region. The size of the recirculation region can be determined by measuring the location at which the velocity becomes zero. Compared to the experimental data of Lourenco and Shih [16], both SGS models under-predict the length of the recirculation region; however, the result from the SM is closer to the experimental results. Immediately following the recirculation region, the streamwise velocity increases rapidly. In comparison with the experimental data of Ong and Wallace [12], the DSM slightly under-predicts the magnitude of this increase.

To further understand the predicitive accuracy of the turbulence models Figure 3.4 shows the non-dimensional mean velocity $\langle\bar{u}\rangle/U_\infty$ at the six different streamwise

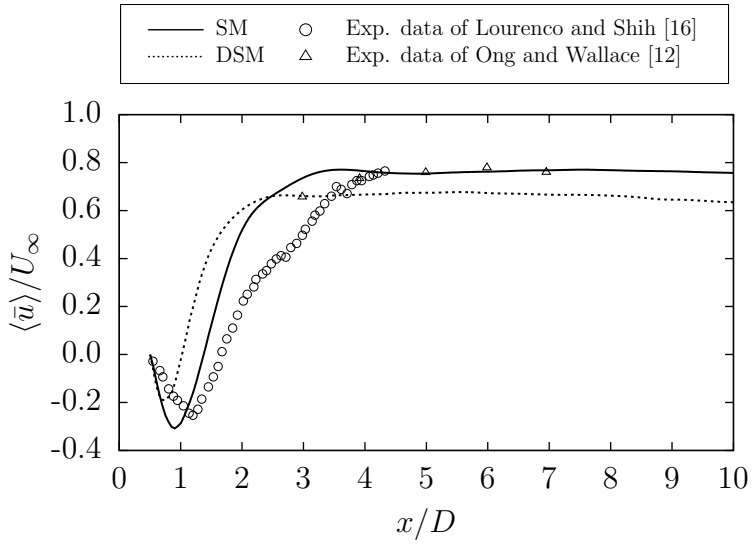

Figure 3.3: Non-dimensional $\langle\bar{u}\rangle/U_\infty$ velocity profile behind a single cylinder along the centeral spanwise plane $y/D = 0$.

locations shown in Figure 3.2. The LES results are compared against the experimental data of Lourenco and Shih [16] in the immediate downstream regions of the cylinder at $x/D = 1.02$, 1.54, and 2.02 against the experimental data of Ong and Wallace [12] in the far downstream regions of the cylinder at $x/D = 4$, 7 and 10. Both SM and DSM under-predict the velocity at near-cylinder locations for $x/D = 1.02$, 1.54 and 2.02. However, the results predicted by the SM are closer to the experimental data of Lourenco and Shih [16] than those by the DSM. In the far downstream locations for $x/D = 4$, 7 and 10, the DSM slightly over-predicts the spanwise velocity. As is observed from Figure 3.4, the spanwise velocity profiles obtained by the LES are symmetrical about the plane $y/D = 0$.

Figure 3.5 shows the non-dimensional mean $\langle\bar{v}\rangle/U_\infty$ velocity. In the near wall region, both models perform similarly, however, in the far wall region the results from the DSM model either overpredicts or underpredicts the normal velocity compared to the SM model. As is noted by Beaudan and Moin [11], at the location $x/D = 1.06$, an asymmetrical pattern appears in the measured profile of Lourenco and Shih [16],

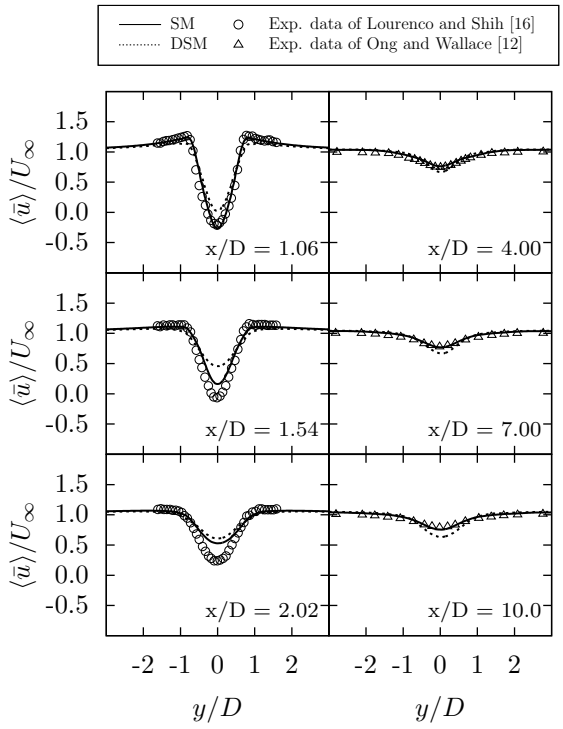

Figure 3.4: Non-dimensional $\langle\bar{u}\rangle/U_\infty$ profiles at six different streamwise locations behind a single cylinder.

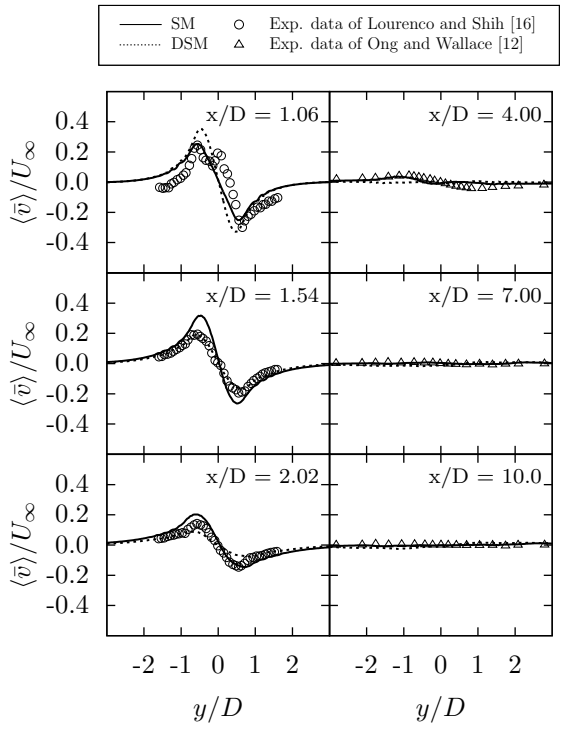

Figure 3.5: Non-dimensional $\langle\bar{v}\rangle/U_\infty$ profiles at six different streamwise locations behind the single cylinder.

and this unphysical result is most likely caused by some flow perturbation within the experiment.

Figure 3.6 compares the numerical predictions of the non-dimensional Reynolds normal stress component $\langle\bar{u}'\bar{u}'\rangle/U_\infty^2$ with the experimental measurements of both Lourenco and Shih [16] and Ong and Wallace [12]. The profile $\langle\bar{u}'\bar{u}'\rangle/U_\infty^2$ exhibits a dual-peak pattern. The two peaks are located around $|y/D| = 0.5$ where the maximum kinetic energy production occurs due to the strong shear layers created by both cylinder sides. As shown in the figure, in comparison with the experimental data of Lourenco and Shih [16], the DSM significantly overestimates the value of the $\langle\bar{u}'\bar{u}'\rangle/U_\infty^2$ at $x/D = 1.06$; however, at other downstream locations, the predictions by the SM and DSM are similar, both of which are in agreement with the experimental data.

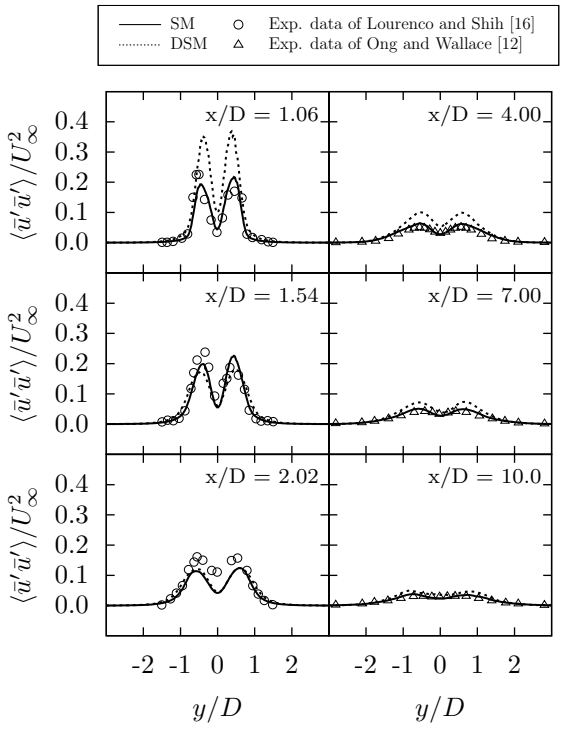

Figure 3.6: Profiles of non-dimensional Reynolds normal stress component $\langle \bar{u}'\bar{u}' \rangle / U_\infty^2$ at six different streamwise locations for a single cylinder.

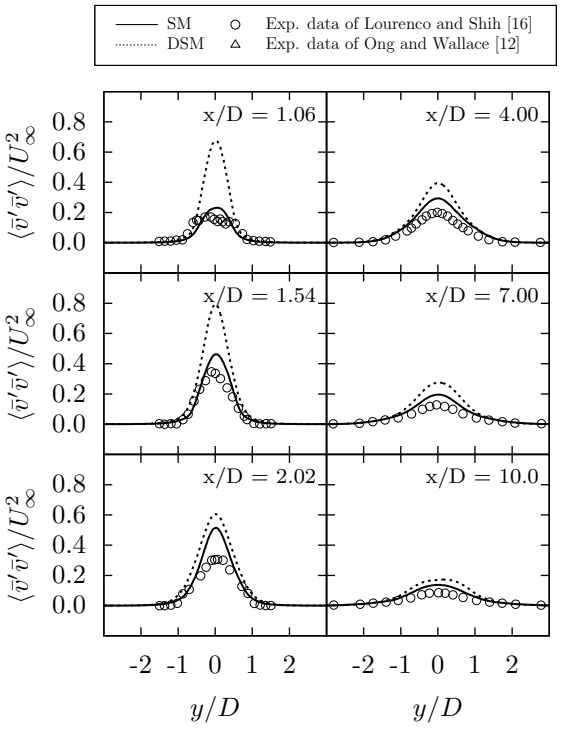

Figure 3.7: Profiles of non-dimensional Reynolds normal stress component $\langle \bar{v}'\bar{v}' \rangle / U_\infty^2$ at six different streamwise locations for a single cylinder.

Figure 3.7 compares the numerical predictions of the non-dimensional Reynolds normal stress component $\langle \bar{v}'\bar{v}' \rangle / U_\infty^2$ with the experimental measurements of both Lourenco and Shih [16] and Ong and Wallace [12]. The profile $\langle \bar{v}'\bar{v}' \rangle / U_\infty^2$ exhibits single peak located on the centerline behind the cylinder. As shown in the figure, in comparison with the experimental data of Lourenco and Shih [16], the DSM over-estimates the $\langle \bar{v}'\bar{v}' \rangle / U_\infty^2$ component of the Reynolds stresses and a significant over-estimation occurs directly behind the cylinder at $x/D = 1.06$. The SM also tends to slightly over-estimate the $\langle \bar{v}'\bar{v}' \rangle / U_\infty^2$, however, this over-estimation is consistent with other numerical results such as those by Lysenko *et al.* [19].

For the flow around a circular cylinder, three distinct pressure regions are usually observed within the vicinity of the cylinder: a stagnation region located upstream of the cylinder typically containing the highest static pressures, a recirculation region

in the rear region of the cylinder typically containing the lowest pressure of the flow field, and an outer flow region dominated by the free stream in the far spanwise region of the cylinder. The pressure coefficient is defined as:

$$C_p = (p - p_\infty) / q_\infty \tag{3.1}$$

where p_∞ is the static pressure and $q = \frac{1}{2}\rho U_\infty^2$ is the dynamic pressure of the free-stream flow. Due to the pressure difference between these three flow regions, a net form drag force acts on the cylinder. The drag coefficient is defined according the relationship:

$$C_D = \frac{F_D}{\frac{1}{2}\rho_\infty U_\infty^2 S} \tag{3.2}$$

where $S = D \times H$ represents the frontal area of the cylinder and H is the height of the cylinder. Figure 3.8 displays the time-averaged pressure coefficients along the surface of the cylinder compared to the experimental data of Norberg [15]. The stagnation point is located at $\theta = 0°$. The average drag coefficient predicted by the SM is around 1.236, which is in agreement with the LES data of Lysenko *et al.* [19].

The periodic Kármán vortex shedding behind a single cylinder is characterized using the Strouhal number defined as $St = fD/U_\infty$. The frequency f for a cylinder is determined from a fast Fourier transform of the time series of the lift coefficient [82]. The Strouhal number predicted by the SM and DSM is $St = 0.214$ and 0.219, respectively. According to the systematic study of Lysenko *et al.* [19] on the Strouhal numbers for single cylinder flow at $Re = 3,900$, the predicted St values by the SM and DSM are in good agreement with other reported experimental and numerical ranges from 0.20 to 0.22.

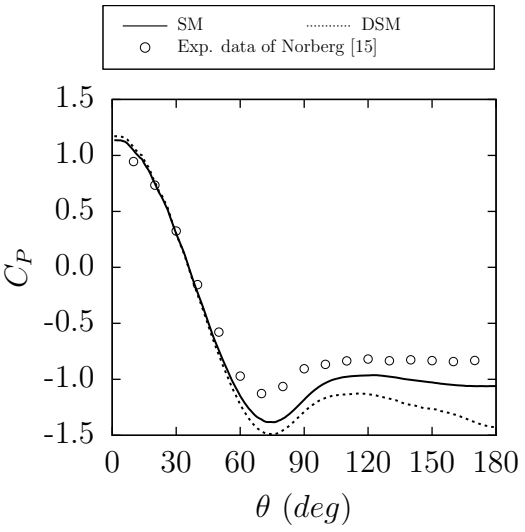

Figure 3.8: Average pressure coefficients along the surface of a single cylinder.

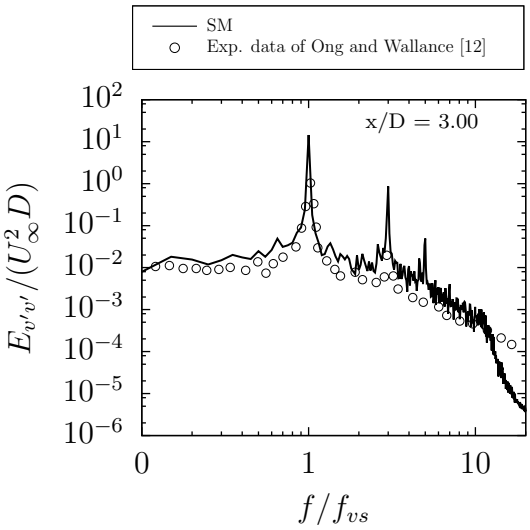

Figure 3.9: $E_{v'v'}$ energy spectrum behind a single cylinder.

Figure 3.9 shows the energy spectrum for the wall normal fluctuating velocity $E_{v'v'}$ at the location $x/D = 3$ in the central vertical plane ($y/D = 0$). The frequency was non-dimensionalized using the vortex shedding frequency and over 40 vortex shedding periods are collected in order to calculate the energy spectrum. In the figure, the spectrum predicted by SM is compared against results of Ong and Wallace [12]. Three distinct sub-ranges are observed: the first sub-range contains the large-scale eddy motions featuring Kármán vortices at the low frequencies; the second sub-range is the so-called inertial subrange where the energy cascade is conserved across the spectrum featuring a constant slope of $-5/3$; and the third sub-range is the viscous dissipation range featuring eddy motions at the high frequencies [83]. The LES results show peaks at the fundamental frequency $f/f_{vs} = 1$ and the second harmonic $f/f_{vs} = 3$, which are in good agreement with the experimental data of Ong and Wallace [12].

3.2.2 Side-by-side cylinders

According to literature, there are two characteristic apparent flow regimes which can be readily identified using the instantaneous force coefficients, as a spike in the force coefficients appears when the transition between the two regimes occurs. This regime transition shall hereafter be referred to as a "flip". The wake statistics and averaged force coefficients are selected over the vortex flipping phenomena as they provide insight into the interactions between two buff bodies. Based on the observation of the satisfactory performance of the SM in LES of the single cylinder flow, the side-by-side configuration is only examined with the SM due to the large computational costs required for performing LES (See Table 3.1 for the computational test matrix).

Figure 3.10 shows the instantaneous velocity $\bar{u}/U_\infty$ for the flow around side-by-side cylinders. Besides showing the wake and wake interactions for the flow around two side-by-side cylinders, Figure 3.10 presents the locations of 6 cutting lines which are used throughout the analysis of the flow around side-by-side cylinders. Additional contour plots of the flow around side-by-side cylinders are available in

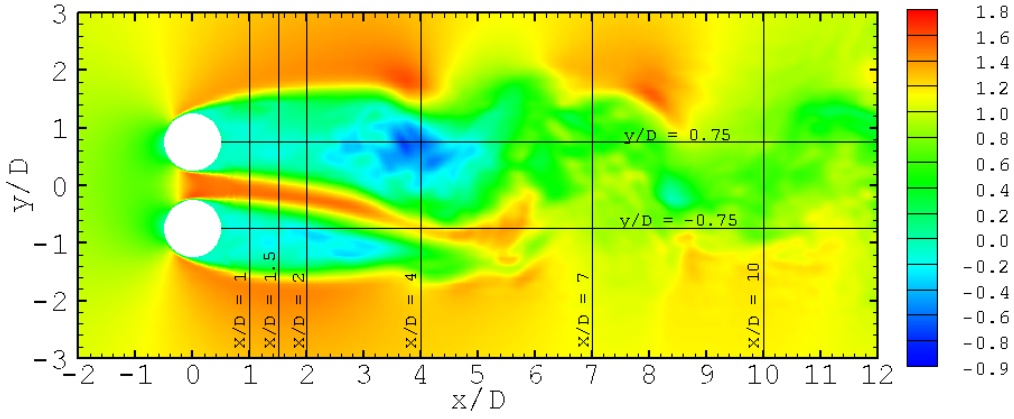

Figure 3.10: Instantaneous streamwise velocity $\bar{u}/U_\infty$ for the flow around two side-by side cylinders separated by $T/D = 1.5$ at time $tU_\infty/D = 990$. The six cutting lines and two centrelines in the figure are used throughout the analysis of the flow around two side-by-side cylinders

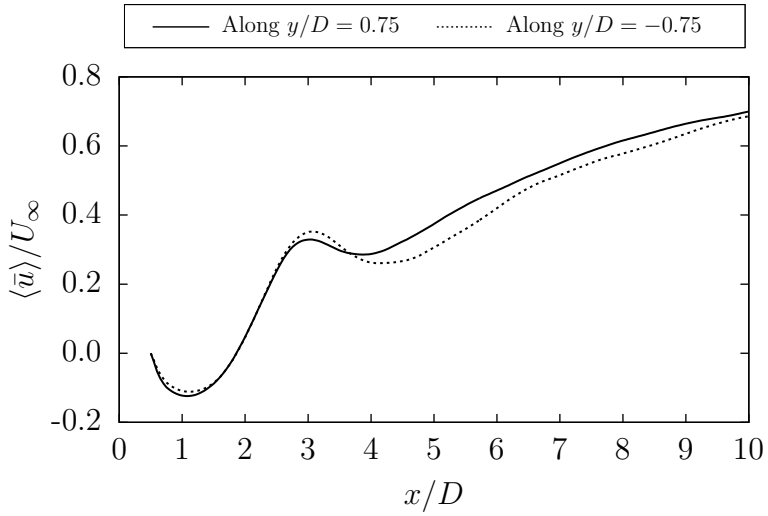

Figure 3.11: Non-dimensional $\langle\bar{u}\rangle/U_\infty$ velocity profile behind two side-by-side cylinders with spanwise separation distance $T/D = 1.5$. The profiles are located along the centrelines behind the cylinders.

Appendix A.

To quantitatively characterize the velocity defect for the flow around side-by-side cylinders, Figure 3.11 presents the mean non-dimensional streamwise velocity $\langle\bar{u}\rangle/U_\infty$ within the central plane for the side-by-side configuration. Due to the symmetrical geometry, similar velocity profiles are expected behind the two cylinders. Within the near wall region, identical velocity profiles are obtained, however, at $x/D = 3$ the slight variation between the profiles is attributed to the small number of flips which occurred when collecting statistics, however, a satisfactory agreement is still observed. Another feature of interest within the flow is located at $x/D = 4$ in which the mixing of the two wakes causes a slight decrease in the streamwise velocity.

To further understand the flow, Figure 3.12 presents the mean non-dimensional spanwise velocity profiles $\langle\bar{u}\rangle/U_\infty$ for the staggered configuration at six different streamwise locations for $x/D = 1$, 1.5, 2, 4, 7 and 10 as shown in Figure 3.10. As can be seen within Figure 3.12, the profiles at $x/D = 1$, 1.50 and 2 show the formation of a wake behind both of the cylinders as the mean streamwise velocity is

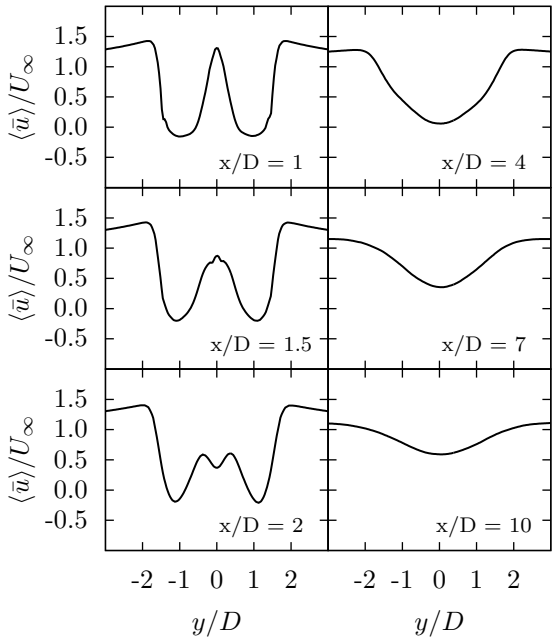

Figure 3.12: Non-dimensional spanwise x-velocity profiles at six different streamwise locations behind side-by-side cylinders separated by $T/D = 1.5$.

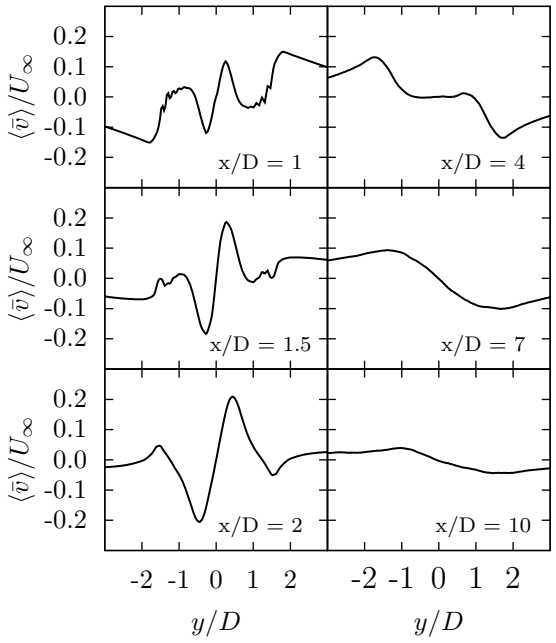

Figure 3.13: Non-dimensional spanwise y-velocity profiles at six different streamwise locations behind side-by-side cylinders separated by $T/D = 1.5$.

negatively valued. At $x/D = 4.0$, a complete merging of the wakes is observed as only a single peak is visible along the centerline between the two cylinders. The profiles at $x/D = 7$ and $x/D = 10$ show the merging of the wake into the freestream flow.

Figure 3.13 shows the non-dimensional mean normal velocity $\langle\bar{v}\rangle/U_\infty$ at the same six streamwise locations as the spanwise velocity. At $x/D = 1$, the merging of the spanwise velocities is already noticeable due to the large span of the wake as two independent dual peak profiles cannot be observed within the figure. The merging of the spanwise velocity profiles is consistent with the spanwise velocity profiles indicating a complete merging of the wake around $x/D = 7$.

The numerical predictions of the non-dimensional Reynolds normal stress component $\langle\bar{u}'\bar{u}'\rangle/U_\infty^2$ is shown in Figure 3.14. The profile $\langle\bar{u}'\bar{u}'\rangle/U_\infty^2$ exhibits a quad-peak pattern within the near wall region. Two smaller peaks are located around $y/D = \pm 1.25$

indicating the outter edges of the cylinders; whereas two large peaks appear around $y/D = \pm 0.25$ which correspond to the inner edges of the cylinders. The larger peaks indicate that the separation gap has a significant influence on the maximum turbulent kinetic energy production and that the presence of the other cylinder significantly influences the formation of the shear layer on the other cylinder. At $x/D = 4$, the merging of the wakes is observed by the presence of only two peaks. At $x/D = 7$ and $x/D = 10$, far downstream of the two cylinders, the merged wake becomes less sensitive to the presence of the cylinders and gradually recovers the background free-stream speed.

The numerical predictions of the Reynolds normal stress component $\langle \bar{v}'\bar{v}' \rangle / U_\infty^2$ is shown in Figure 3.15. The profiles of the $\langle \bar{v}'\bar{v}' \rangle / U_\infty^2$ exhibits a single peak along the centeral line of the separation gap at the streamwise location $x/D = 1$. This indicates

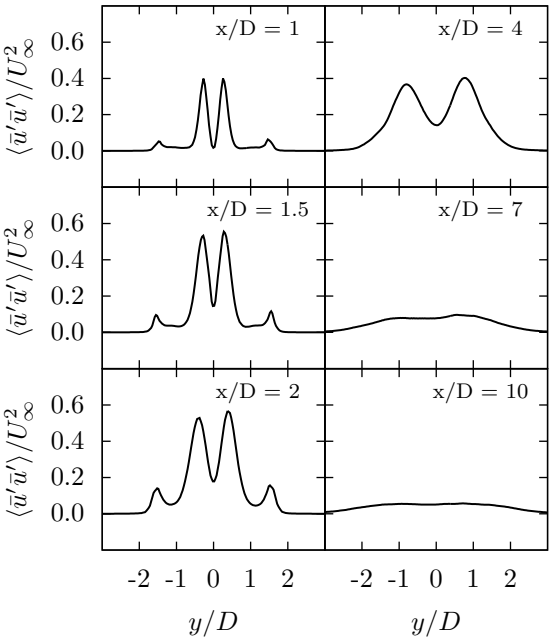

Figure 3.14: Profiles of non-dimensional Reynolds normal stress component $\langle \bar{u}'\bar{u}' \rangle / U_\infty^2$ at six different streamwise locations for side-by-side cylinders separated by $T/D = 1.5$.

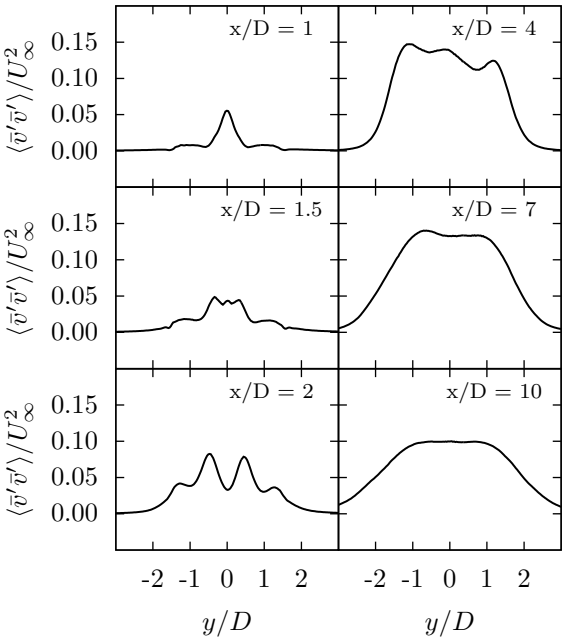

Figure 3.15: Profiles of non-dimensional Reynolds normal stress component $\langle \bar{v}'\bar{v}' \rangle / U_\infty^2$ at six different streamwise locations for side-by-side cylinders separated by $T/D = 1.5$.

an increase in turbulent kinetic energy and showes the effect of the separation gap on the formation of the wake. At $x/D = 1.50$, a widening of the $\langle \bar{v}'\bar{v}' \rangle / U_\infty^2$ peak can be observed, and at $x/D = 2$, the peaks located directly behind the two cylinders appear. At $x/D = 4$, a significant increase in $\langle \bar{v}'\bar{v}' \rangle$ can be observed which is attributed to the merging of the two wakes as a single peak begins forming. At $x/D = 7$, only a single peak can be seen, indicating that the merging of the wakes is complete.

To understand the drag coefficients acting upon two side-by-side cylinders, it is required to present the pressure coefficients acting around the side-by-side cylinders as shown in Figure 3.16. The pressure coefficients are measured in a clockwise direction around both cylinders. While the pressure coefficients displayed a symmetry about the plane $\theta = 180°$ for the single cylinder simulations, an asymmetry is observed in the side-by-side case. The asymmetry is caused by a lower pressure region which forms within the separation gap between the cylinders which reduces the pressure coefficient on the gap side of the cylinders. The lower pressure also causes an increase in the velocity of the flow passing through the gap, and as observed within Figure 3.12, a higher velocity of the flow is observed at the location of the separation gap at the

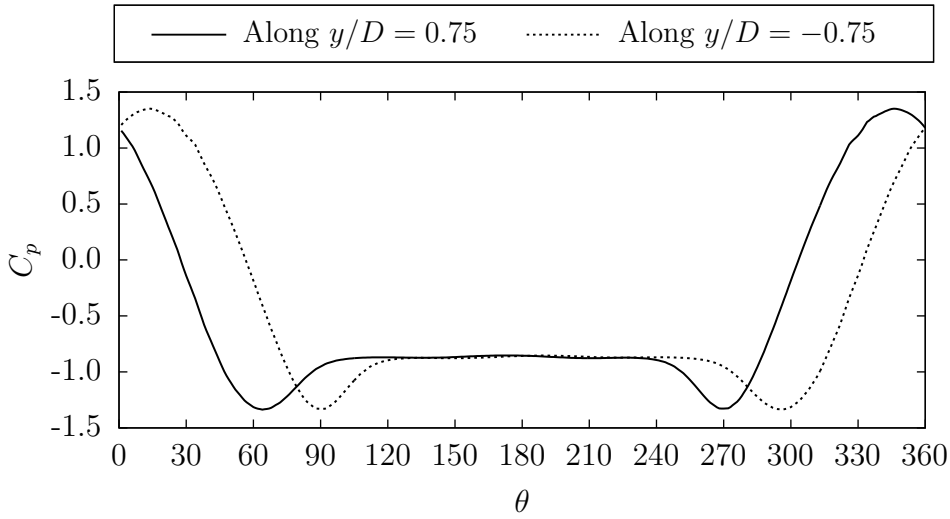

Figure 3.16: Average pressure coefficients along the surface of side-by-side cylinders. The stagnation point is located at $\theta = 0°$.

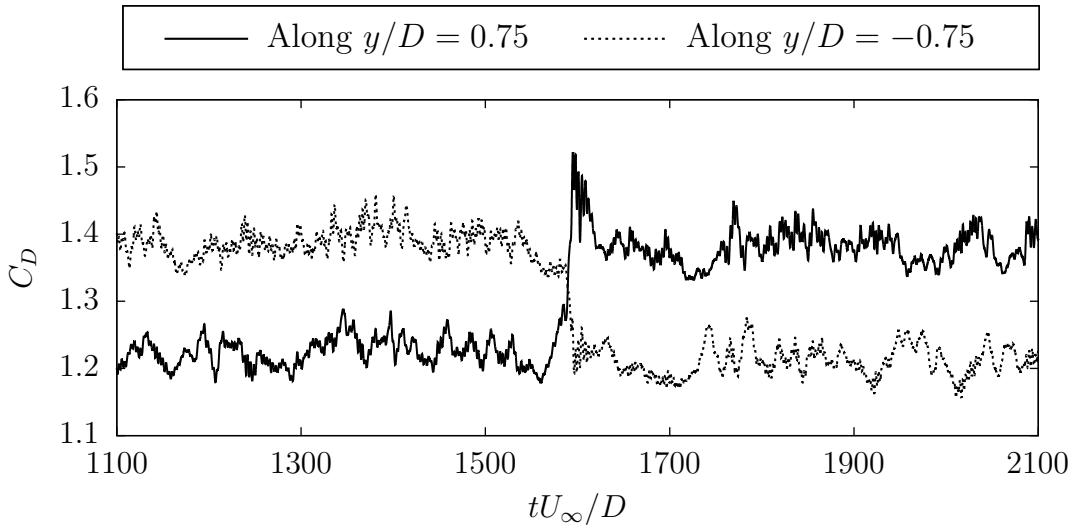

Figure 3.17: Instantaneous drag coefficients for the flow around side-by-side cylinders

locations $x/D = 1$ and $x/D = 1.50$.

The drag coefficients acting on side-by-side cylinders are determined to be $C_D = 1.299$ and 1.306 whereas the lift coefficients acting on the cylinders are determined to be $C_L = -0.3539$ and 0.3558. Due to the symmetry of the domain, the value of the force coefficients are expected to be the same on each of the cylinders but vary during a vortex period. The average force coefficients are in good agreement with each other as the average drag coefficients different by less than 1% and the average lift coefficients differ by less than 2%. Throughout the simulations, the instantaneous drag coefficient peaked at a maximum value of 1.522, which along with the flipping phenomena, can be seen in Figure 3.17.

3.2.3 Staggered cylinders

Based on the observation of the satisfactory performance of the SM in LES of the single cylinder flow, the staggered configuration is only examined with the SM due to the large computational costs required for performing LES (See Table 3.1 for the

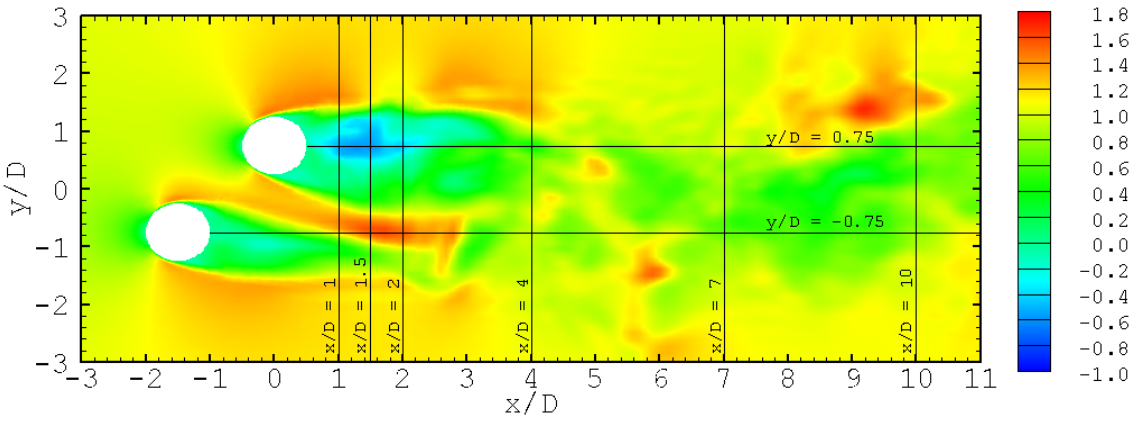

Figure 3.18: Instantaneous streamwise velocity $\bar{u}/U_\infty$ for the flow around two side-by side cylinders separated by $T/D = L/D = 1.5$ at time $tU_\infty/D = 450$. The six cutting lines in the figure are used throughout the analysis of the flow around two staggered cylinders.

computational test matrix).

Figure 3.18 shows the instantaneous velocity $\bar{u}/U_\infty$ for the flow around staggered cylinders. Besides showing the wake and wake interactions for the flow around two staggered cylinders, Figure 3.18 presents the locations of 6 cutting lines which are used throughout the analysis of the flow around staggered cylinders. The interactions and positioning of the staggered cylinders could influence the formation of eddies around the cylinder resulting in a decrease in the drag coefficients. Additional contour plots of the flow around staggered cylinders at a Reynolds number of $Re_D = 3,900$ separated by $T/D = L/D = 1.5$ are available in Appendix A.

To qualitatively characterize the velocity defect for the flow around staggered cylinders, Figure 3.19, presents the non-dimensionalized streamwise profile of $\langle\bar{u}\rangle\ U_\infty$; the recirculation zones behind both cylinders are clearly observable. In this figure, the location $x/D = 0$ corresponds to the center of the upstream cylinder. As shown in the figure, the streamwise velocity profiles indicate a larger recirculation region behind the downstream cylinder. However, it needs to be indicated that as the wake of the upstream cylinder is angled away, the full length of the upstream wake is not

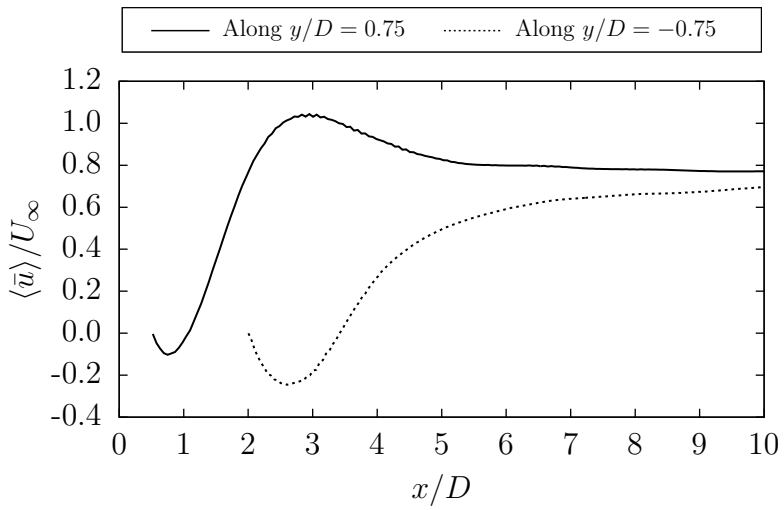

Figure 3.19: Non-dimensional streamwise velocity profile behind two staggered cylinders separated by $T/D = L/D = 1.5$. The profiles are located along the centrelines behind the cylinders.

completely captured by a profile directly behind the centreline of the cylinder. It is also observed that the streamwise velocity profile after the recirculation region takes a significantly longer distance to evolve behind the downstream cylinder in comparison with that behind the upstream cylinder.

To further understand the physics of the flow around staggered cylinders, Figure 3.20 displays the mean non-dimensionalized velocity $\langle\bar{u}\rangle/U_\infty$ for the staggered configuration at six different streamwise locations for $x/D = 1$, 1.50, 2, 4, 7 and 10. The location $x/D = 0$ corresponds to the center of the downstream cylinder and the location $y/D = 0$ corresponds to the center of the separation gap between the two staggered cylinders. The first three profiles show two distinct peaks, located behind each of the two cylinders, where the pattern is in agreement with that described by Sumner [24]. Due to the asymmetrical geometry, the difference in the magnitudes of these two peaks is expected. Furthermore, in comparison with the single cylinder case, it is clear that the spanwise location, $y/D = 1.25$, of the peak for the upstream cylinder does not correspond to the centreline, $y/D = 0.75$, across the cylinder.

Instead, a high pressure region caused by the downstream cylinder forces the wake to deviate away, resulting in the peak to be offset from the centreline of the upstream cylinder. In regions further downstream of the recirculation zone for $x/D = 4$ to 10, the wake behind two cylinders merge and the profiles of $\langle \bar{u} \rangle$ U_∞ exhibits a single-peaked pattern. For both cylinders, a recirculation region develops in their downstream region. The recirculation zone featuring negative streamwise velocities behind the downstream cylinder is evident in Figure 3.20.

Figure 3.21 shows the mean non-dimensionalized normal velocity $\langle \bar{v} \rangle / U_\infty$. The first profile shows four distinct peaks corresponding to individual wakes formed behind the two cylinders, however, even at $x/D = 1$ the wakes are already starting to merge. The profiles at $x/D = 1.50$ and $x/D = 2$ show three distinct peaks indicating that the two central peaks have merged. The two peaked pattern at $x/D = 4$ indicates a complete merging of the wakes although, a bias towards the downstream cylinder is observable within the wake. At $x/D = 7$ and $x/D = 10$, the merged wake becomes less sensitive to the presence of the cylinders and gradually recovers the background freestream speed.

The predicted non-dimensionalized streamwise Reynolds normal stress component $\langle \bar{u}'\bar{u}' \rangle / U_\infty^2$ and the predicted non-dimensionalized Reynolds normal stress component $\langle \bar{v}'\bar{v}' \rangle / U_\infty^2$ are shown in Figures 3.22 and 3.23 respectively. The first three profiles of $\langle \bar{u}'\bar{u}' \rangle / U_\infty^2$ exhibit a quadruple peak pattern and the four peaks correspond to locations of maximum turbulent kinetic energy produced by the strong shear layers on both sides of each cylinder. Similarly, first three profiles of $\langle \bar{v}'\bar{v}' \rangle / U_\infty^2$ exhibit a dual peak pattern and the two peaks correspond to locations of maximum turbulent kinetic energy. Due to the asymmetry of the geometry caused by the separation distances $T/D = 1.5$ and $L/D = 1.5$, the magnitude of the peaks behind the downstream cylinders are significantly larger than those of the upstream cylinder as

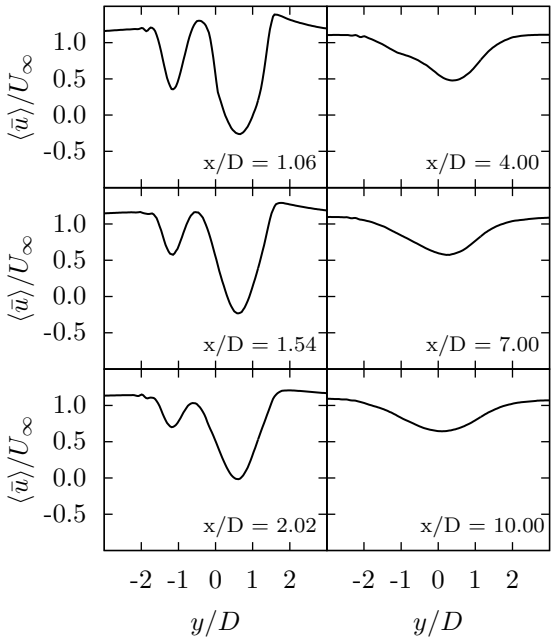

Figure 3.20: Non-dimensional spanwise x-velocity profiles at six different streamwise locations behind two staggered cylinders separated by $T/D = L/D = 1.5$.

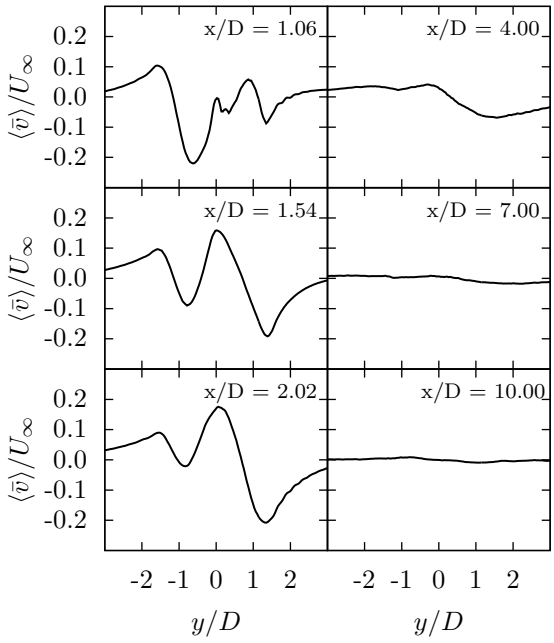

Figure 3.21: Non-dimensional spanwise y-velocity profiles at six different streamwise locations behind two staggered cylinders separated by $T/D = L/D = 1.5$.

expected [24]. Furthermore, as the wake of the upstream cylinder is diverted by the downstream cylinder, the two peaks created by the upstream cylinder are also shifted away accordingly. It is interesting to observe that at $x/D = 2$, the merged peaks are still biased towards the location of the downstream cylinder. As the distance from the two staggered cylinders further increases, the wakes behind two cylinders become fully mixed due to turbulent convection and diffusion in the spanwise direction. The profile of $\langle\bar{u}'\bar{u}'\rangle/U_\infty^2$ becomes increasingly symmetrical in the spanwise direction whereas the profile of $\langle\bar{v}'\bar{v}'\rangle/U_\infty^2$ remains biased towards the downstream cylinder. As shown in Figures 3.22 and 3.23, in the far downstream region of the two cylinders for $x/D = 4$ to 10, the magnitude of $\langle\bar{u}'\bar{u}'\rangle/U_\infty^2$ and $\langle\bar{v}'\bar{v}'\rangle/U_\infty^2$ decreases and the patterns smear out.

As the flow passes the staggered cylinders, a stagnation zone and a recirculation zone

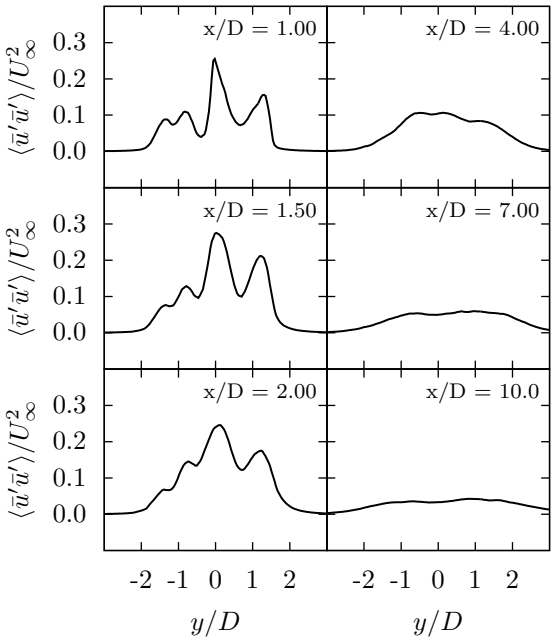

Figure 3.22: Profiles of non-dimensional Reynolds normal stress component $\langle \bar{u}'\bar{u}' \rangle / U_\infty^2$ at six different streamwise locations for staggered cylinders separated by $T/D = L/D = 1.5$.

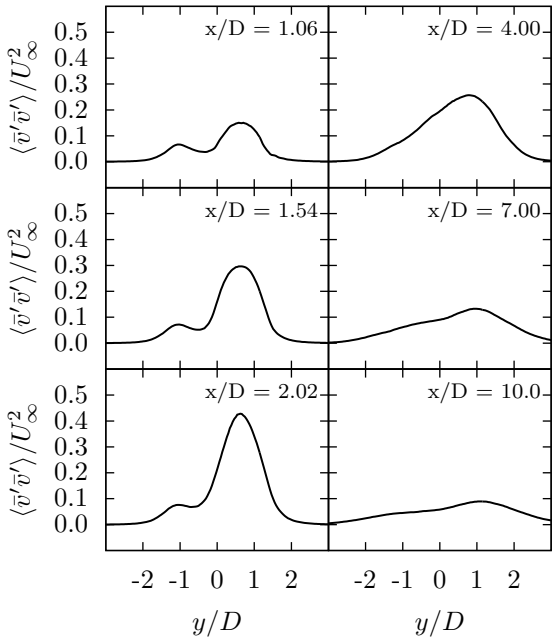

Figure 3.23: Profiles of non-dimensional Reynolds normal stress component $\langle \bar{v}'\bar{v}' \rangle / U_\infty^2$ at six different streamwise locations for staggered cylinders separated by $T/D = L/D = 1.5$.

appear in the front and rear of the cylinder respectively. The pressure distribution around the cylinders is similar to that of the single cylinder case. Furthermore, both cylinders induce wakes, which dynamically interact with each other in the downstream region and this creates a significant impact on the pressure distribution. The time-averaged pressure coefficients around the two cylinder surfaces are shown in Figure 3.24, which exhibits a similar shape to that of the single cylinder flow shown previously in Figure 3.8. Due to the pressure difference acting on the staggered cylinders, a net drag force forms on the cylinders. The average drag coefficients predicted by the SM is 1.252 for the upstream cylinder and 1.152 for the downstream cylinder which is lower than the drag forces acting on the side-by-side cylinders.

Similar to the single cylinder case, the periodic vortex shedding instability behind

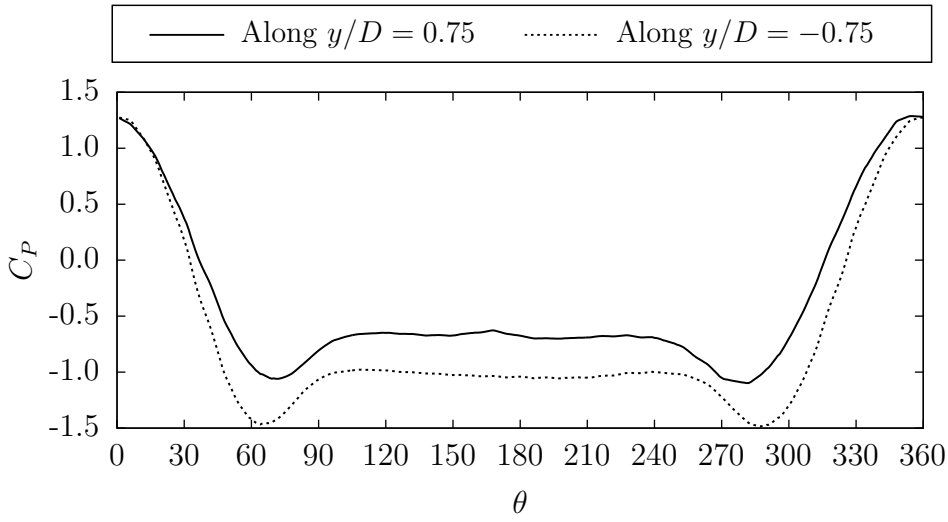

Figure 3.24: Average pressure coefficients along the surface of both staggered cylinders. The stagnation point is located at $\theta = 0°$.

both cylinders can be characterized using the Strouhal number. Based on the SM, the LES prediction of the Strouhal numbers for the staggered cylinder case is 0.263 for the upstream cylinder and 0.167 for the downstream cylinder respectively. This current result that the Stouhal number for the upstream cylinder is larger than that of the downstream cylinder qualitatively agrees with the data presented by Sumner [24].

3.2.4 Investigation into the drag inducing flow phenomena for cylinder configurations

By identifying the flow phenomena that can increase or decrease the drag coefficients acting upon two cylinder configurations, the knowledge can be applied to the problem of optimising hydro-kinetic turbines by positioning the turbines the increase favorable drag reducing flow phenomena while minimising unfavorable drag increasing flow phenomena. Figure 3.25 presents contour plots of the instantaneous streamwise velocity $\bar{u}\,U_\infty$, the mean streamwise velocity $\langle\bar{u}\rangle\,U_\infty$ and the mean pressure coefficients

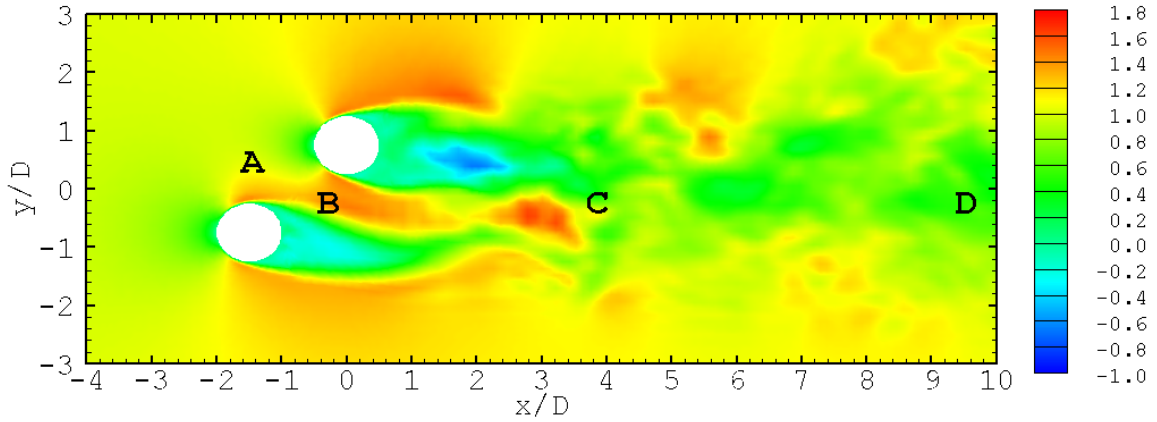

(a) Instantaneous streamwise velocity $\bar{u}/U_\infty$ around two staggered cylinders separated by $T/D = L/D = 1.5$ for time $tU_\infty/D = 450$.

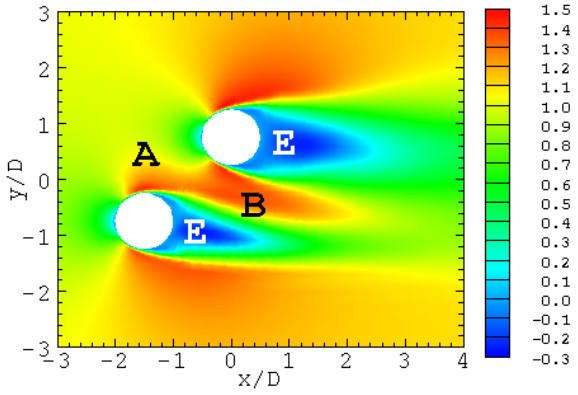

(b) Mean streamwise velocity $\langle\bar{u}\rangle/U_\infty$ around two staggered cylinders separated by $T/D = L/D = 1.5$.

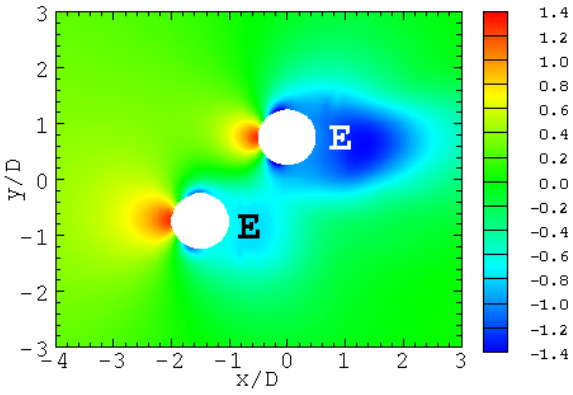

(c) Average pressure coefficients C_p around two staggered cylinders separated by $T/D = L/D = 1.5$.

Figure 3.25: Contour plots of the flow around two staggered cylinders separated by $T/D = L/D = 1.5$ highlighting flow phenomena which could influence the drag coefficients.

C_p for staggered cylinders. Figure 3.25 highlights features which could influence the drag coefficients acting on the cylinders. Contour plots for the side-by-side configuration are located in Appendix A.

When any obstruction is positioned in a flow, in order to satisfy the principle of conservation of momentum, the flow passing around the obstruction experiences an increase in velocity. In Figure 3.25, point A represents the velocity increase associated with the flow passing around the upstream cylinder. Depending upon the separation distance between the cylinders in the spanwise direction, the downstream cylinder

can be located partially or completely within the higher velocity flow passing around the upstream cylinder. Based upon the Equation 1.1, an increase in velocity can be attributed to a decrease in the drag coefficients acting upon a cylinder.

Point B is influenced by the streamwise and spanwise gap between the staggered cylinders. For staggered cylinders, the general trends indicate that decreasing the separation gap results in a decrease in the drag coefficients acting around the cylinders [24, 32, 34]. The reason for the drag reduction is explained as follows: by decreasing the size of the gap for staggered cylinders, the blockage ratio of the configuration is increased and this causes an overall increase in the velocity of the flow passing around the cylinders and through the separation gap. Furthermore, Igarashi [22] and Williamson [23] both show that the separation gap influences the flow phenomena within the cylinder wakes. The separation gap can be linked to flow properties such as turbulence generation, the length of the wake and the pressure coefficients.

The region shown by point C represents the wake interaction point. The wake interactions in the flow cause a significant increase the turbulence levels in the wake. Depending on the separation distance between the cylinders, the wake interaction point can cause higher turbulence levels in the near wall region of the cylinders resulting in earlier flow separation on the cylinders. Earlier flow separation can increase the size of the recirculation region behind the cylinders and increase the pressure difference between the front and back sides of the cylinder causing an increase in the drag coefficients. It is interesting to note that the staggered configuration contained lower turbulence levels and lower drag coefficients for both the upstream and downstream cylinders.

While point D does not influence the drag coefficients acting upon either of the two staggered cylinders shown in Figure 3.25, for hydro-kinetic turbine farm applications,

the length of the wake can significantly influence the streamwise spacing between turbine rows. Furthermore, should the turbines have to be positioned within the wake due to spacing constraints, the lower wake velocity can contribute to an increase in the drag coefficients acting upon the turbines, a decrease within the power generated by the turbines and an increase the levelized cost of energy for the turbine farm.

The low pressure region which forms directly behind each of the two staggered cylinders is represented by point E. In their study of tandem and side-by-side cylinders using LES Vu *et al.* [84] showed that increasing the pressure difference between the front and back of the cylinders increased the drag coefficients acting on the cylinders. The results from Vu *et al.* are consistent with the current research as the pressure difference is higher within the side-by-side configuration in comparison to the staggered configuration. As the drag caused by the pressure difference on the front and back of a cylinder represents a large component of the total drag force [85], the increased drag coefficients for the side-by-side configuration can be directly related to the increase in the pressure difference. We postulate that the increased turbulence levels of the side-by-side configuration influence the formation of the low pressure regions and which contribute to the increase in the drag coefficient.

3.3 Summary of the Chapter

As a first approach to understanding turbine optimization, current chapter examined wall resolved LES of the turbulent wake around a single, side-by-side and staggered cylinders for $Re = 3,900$, $3,000$ and $3,000$, respectively, as shown in Table 3.1. For the single cylinder case, the results on the mean and fluctuating velocities for the single cylinder case were in good agreement with reported experimental results available in the literature. The flow structures around a single and staggered cylinder have been

investigated through a variety of methods based upon the first- and second-order streamwise velocity statistics and the pressure and drag coefficients acting around the surface of the cylinder. In the single cylinder case, the energy spectrum at $x/D = 3$ is also examined. Furthermore, the effect of the SGS model was also explored and the SM was found to produce the most accurate results. For the two cylinder simulations, only the SM was used. In the side-by-side cylinder case, a bi-stability within the flow was observed. The results from the side-by-side cylinders were examined by averaging the results over equal periods within the two flow regimes. Symmetrical flow statistics which were obtained correlated well with the geometry of this case. The merging of the two wakes were also clearly observed within the results. Within the staggered cylinder case, the merging of the wakes was also, clearly observable and furthermore, it was noted that the wake behind the upstream cylinder was diverted away from the downstream cylinder due to the pressure difference created by it, exhibiting an asymmetrical pattern in the spanwise direction. Finally, the configurations were examined to determine the flow features which influenced the drag coefficients. It was found that increased upstream velocity regions, wake turbulence, pressure coefficients and geometry were the influential factors on the drag coefficients. Table 3.2 summarises the three cases examined within the current chapter and which objectives have been fulfilled within the simulations.

Table 3.2: Computational matrix for a single and two cylinders

Simulation	**Reynolds Number**	**Objective Number on page 5**	**Findings**
Single cylinder	$3,900$	1	SM model produced better results compared to the DSM. Results obtained are in agreement with experimental data obtained from the literature
Side-by-side cylinders	$3,000$	2	Side-by-side cylinders contained two flow regimes. The simulations contained higher drag coefficients, pressure coefficients and Reynolds normal stresses in comparison to the staggered configuration.
Staggered cylinders	$3,000$	2	Staggered cylinders contained lower drag coefficients, pressure coefficients and Reynolds normal stresses in comparison to the side-by-side configuration. The pressure drag corresponds to the largest source of drag on a cylinder and a lower pressure difference between the front and back of the staggered cylinders is the primary factor in the reduction of the drag coefficient.

The results from the cylinder simulations provide a simple means with which to familiarize with the interactions between two buff bodies. Due to the significant geometry differences between cylinders and hydro-kinetic turbines, and the presence of unique flow features caused by the geometry the lower drag experience by the staggered simulations compared to the side-by-side simulation cannot be correlated directly to turbine or airfoil applications.

Chapter 4

Turbulent wake behind two stationary airfoils

Simulations using LES as a tool around two stationary airfoils represents an interesting challenge to optimize the position of hydrokinetic turbines in a farm. The objective is to build upon the two cylinder studies to better understand the wake and vortex dynamics using a more representative airfoil geometry compared to a cylinder.

The methodolgy applied is to examine the turbulent wake and the wake interactions behind two infinite length NACA 0021 airfoils within a side-by-side and staggered configuration, for $Re_c = 3,000$, with an angle of attack of 2° using wall resolved LES. Based upon the observation of its satisfactory predictive performances in LES of cylinder flows, the SM is employed for conducting LES in this chapter. Although there are reported numerical and experimental studies on stationary airfoils and rotating airfoils, most of the reports are given in a qualitative manner. Figure 4.1 defines the side-by-side and staggered configurations for the airfoils based upon the $\frac{1}{4}$ chord point. For the side-by-side configuration, the spanwise separation distance

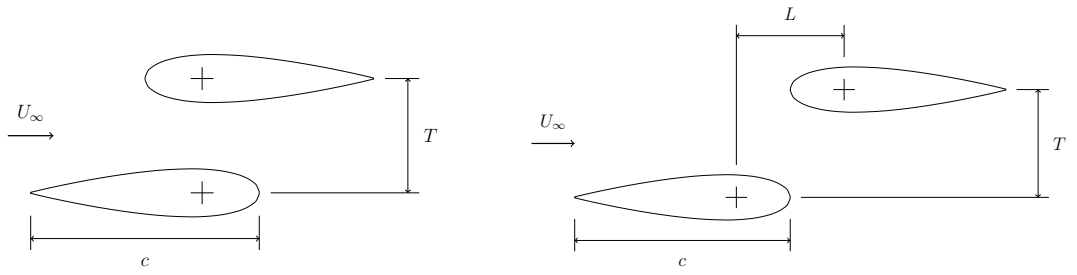

(a) side-by-side airfoils (b) staggered airfoils

Figure 4.1: Configurations for two stationary symmetrical airfoils with an angle of attack of 2°: if $L/c = 0$, the airfoils are side-by-side; if $L/c > 0$ the airfoils are staggered

is set to $T/c = 0.5$, and for the staggered configuration the spanwise and streamwise separation distances are set to $T/c = 0.5$ and $L/c = 0.5$ respectively. Due to the geometry of the airfoils and the streamlined nature of the wake behind an airfoil, in order to ensure wake interactions the non-dimensional spacings are reduced when compared to the cylinder configurations considered in Chapter 3. Table 4.1 shows the computational test matrix for the simulations and validation experiments in this chapter. The velocities $\langle\bar{u}\rangle$ and $\langle\bar{v}\rangle$ are non-dimensionalised by U_∞ and the Reynolds stresses $\langle\bar{u}'\bar{u}'\rangle$, $\langle\bar{u}'\bar{v}'\rangle$ and $\langle\bar{v}'\bar{v}'\rangle$ are non-dimensionalised by U_∞^2.

4.1 Computational domain and boundary conditions

Figure 4.2 shows the computational domains for the airfoil simulations. The computational domains consists of a rectangular domain with a C-grid mesh encompassing the airfoils, which is different from the O-grid mesh used in the previous chapter for the cylinder flow simulations. The C-grid mesh presents several benefits for the airfoil flow simulations. The C-grid reduces the complexity and non-orthogonality of the mesh around the trailing edge of the airfoils, and provides grid

Table 4.1: Computational matrix for side-by-side and staggered NACA 0021 airfoils

Numerical Simulations				
Case	**Reynolds Number**	**L/c**	**T/c**	**Objective**
Side-by-side airfoils	3,000	1.5	0	Focus on the turbulence activities indicated by the second-order moments of the flow field, and the drag coefficients.
Staggered airfoils	3,000	1.5	1.5	Focus on the turbulence activities indicated by the second-order moments of the flow field, and the drag coefficients.
Details				
All simulations are performed using OpenFOAM v2.3.0 using wall-resolved LES with explicit filtering and the SM SGS model. To ensure accurate results a minimum grid resolution of $\Delta x^+ < 30$, $\Delta y^+ < 1$ and $\Delta z^+ < 30$ is used throughout all the simulations. The NACA 0021 airfoils are aligned at the 1/4 chord point with an angle of attack of 2°. The origins for the configurations are kept constant between the simulations and are located at the 1/4 chord point of the upstream airfoil.				
Experiments				
Case	**Reynolds Number**	**L/c**	**T/c**	**Objectives**
Side-by-side airfoils	3,000	1.5	0	To validate the flow around side-by-side airfoils aligned at the $\frac{1}{4}$ chord point.
Staggered airfoils	3,000	1.5	1.5	To validate the flow around staggered airfoils aligned at the $\frac{1}{4}$ chord point
Details				
All experiments are performed using an ADV at two different measurements locations $x/c = 4$ and $x/c = 7$ in a water tunnel. To ensure that all turbulence scales are captured the results are collected for 2 minutes at 200 Hz using an ADV. The NACA 0021 airfoils are aligned at the 1/4 chord point with an angle of attack of 2°. The origin is kept constant between the experiments and is located at the 1/4 chord point of the upstream airfoil.				

refinement in the spanwise direction for the wake behind the airfoils. The simulations are performed using the identical wall resolution criteria as the previous cylinder simulations: $\Delta x^+ < 30$, $\Delta y^+ < 1$ and $\Delta z^+ < 30$. For the airfoil simulations, the domain width is set to be $5c$ with the centreline of the airfoil configurations positioned along the centreline of the domain, $5c$ downstream from the inlet, $5c$ away from the top and bottom sides and $15c$ upstream of the outlet. The dimensions of the computational domains are selected to be consistent with cylinder simulations but also to ensure that the boundaries are far away from the airfoils such that the impact from the boundary conditions does not significantly affect the wake region of interest.

Although the geometry of an airfoil and cylinder differ significantly, as shown in Figure 4.2, the computational domains remain very similar to the cylinder simulations in Chapter 3. The following boundary conditions are used in the simulations: a

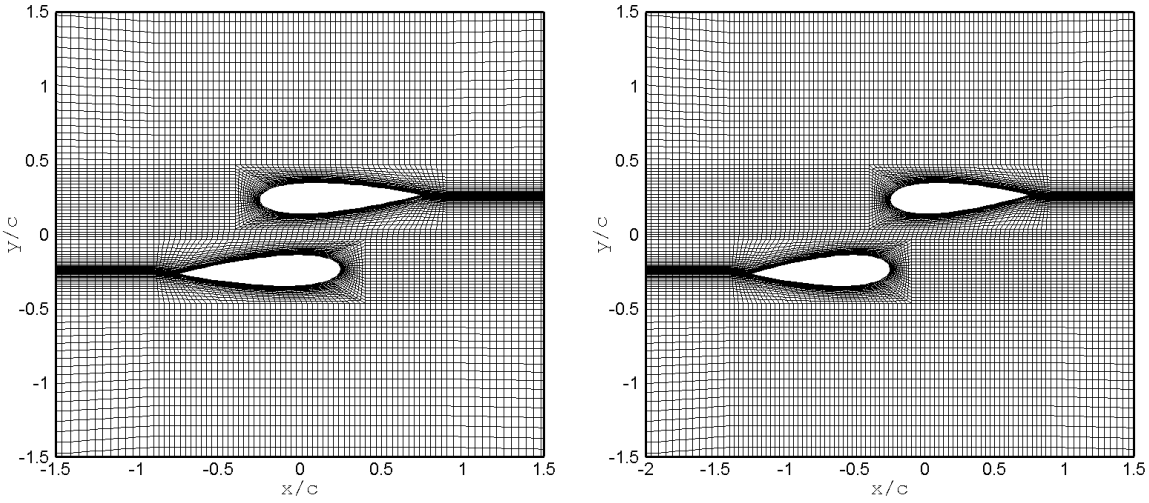

(a) Side-by-side airfoils (b) Staggered airfoils

Figure 4.2: Snapshot of the meshes for the two airfoil configurations

uniform velocity profile is applied at the inlet, a zero gradient is applied at the outlet, the top, bottom, front and back sides are set to periodic and wall, no-slip, boundary conditions are applied to the airfoil surfaces.

4.2 Turbulent wake around two side-by-side and staggered airfoils

The computational LES results of flows around the side-by-side and staggered airfoil configurations are compared. All results are presented with the origin placed at the $\frac{1}{4}$ chord point of the upstream airfoil ($x = 0$). Besides the force coefficients, this research also focuses on the characteristics of turbulence generated by hydrokinetic turbines, as turbulence can have an impact on marine life and the environment [86]. When exposed to turbulence and shear stresses, fish experience differential forces across their body which can result in injury or mortality [86, 87]. In view of this, it is necessary to investigate the characteristics of the Reynolds shear stress component

$\langle \bar{u}'\bar{v}' \rangle / U_\infty^2$.

Figure 4.3 shows the instantaneous filtered velocity $\bar{u}/U_\infty$ around side-by-side and staggered airfoils aligned at the 1/4 chord point at different times. Similar to the cylinder results, shown in the previous chapter, the configuration of the airfoils can influence the formation of the eddies, the turbulence levels within the wake and the pressure coefficients acting upon the airfoils in such a way as to reduce the drag coefficients acting upon airfoils. Figure 4.3 also presents the locations of several lines which are used throughout the analysis of the flow around side-by-side and staggered airfoils. Due to the additional streamwise length of the staggered configuration and the fixed origin, located at the 1/4 chord point of the upstream airfoil, the line $x/c = 1$ is not examined for this configuration.

4.2.1 Velocity statistics

To qualitatively examine length of the velocity defect for the flow around airfoil configurations, Figure 4.4 displays the non-dimensional profiles of the streamwise velocity $\langle \bar{u} \rangle / U_\infty$ along the centerline directly behind each of the airfoils for the side-by-side and staggered configurations. For the upstream airfoils, the profiles for both the staggered and the side-by-side configurations are similar to each other, however, the flow develops slightly quicker within the side-by-side configuration as compared to the staggered configuration. From the figure, it is apparent that in the far downstream region of the airfoils, the non-dimensional streamwise velocity is fully developed and approaches an approximately constant value of $\langle \bar{u} \rangle / U_\infty = 0.8$.

Figure 4.5 displays non-dimensional profiles of the mean spanwise velocity ($\langle \bar{u} \rangle / U_\infty$) for the side-by-side, and staggered configurations with origin placed at the $\frac{1}{4}$ chord point of the upstream airfoils. By comparing the airfoil results to the cylinder results in Figure 4.3, the effects of the streamlined airfoil shape on the turbulent wake are

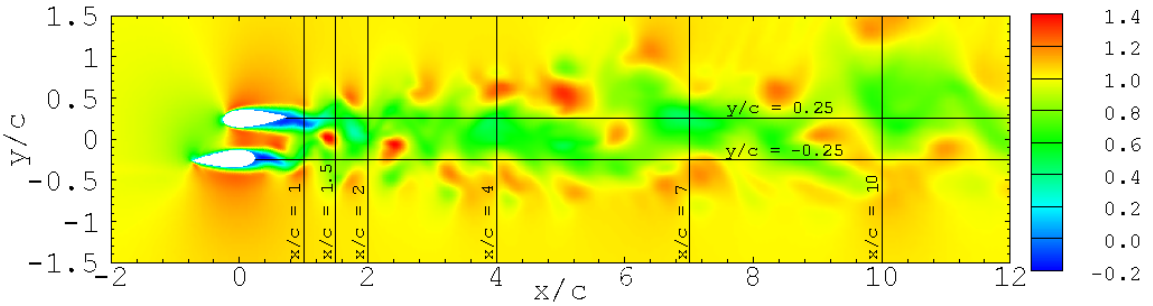

(a) Instantaneous streamwise velocity $\bar{u}/U_\infty$ around two side-by-side airfoils separated by $T/c = 0.5$ at time $tU_\infty/c = 450$. The six cutting lines and two centrelines in the figure are used throughout the analysis of the flow around two side-by-side airfoils.

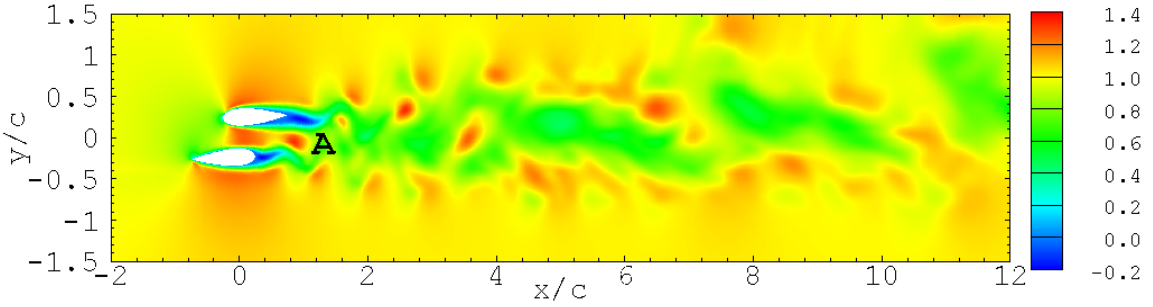

(b) Instantaneous streamwise velocity $\bar{u}/U_\infty$ around two side-by-side airfoils separated by $T/c = 0.5$ at time $tU_\infty/c = 390$. Point A represents the location of the wake interaction point.

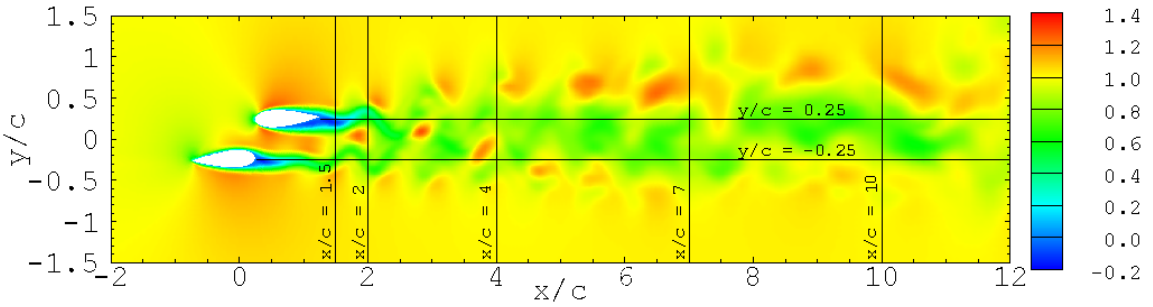

(c) Instantaneous streamwise velocity $\bar{u}/U_\infty$ around two staggered airfoils separated by $T/c = L/c = 0.5$ at time $tU_\infty/c = 600$. The five cutting lines and two centrelines in the figure are used throughout the analysis of the flow around two staggered airfoils.

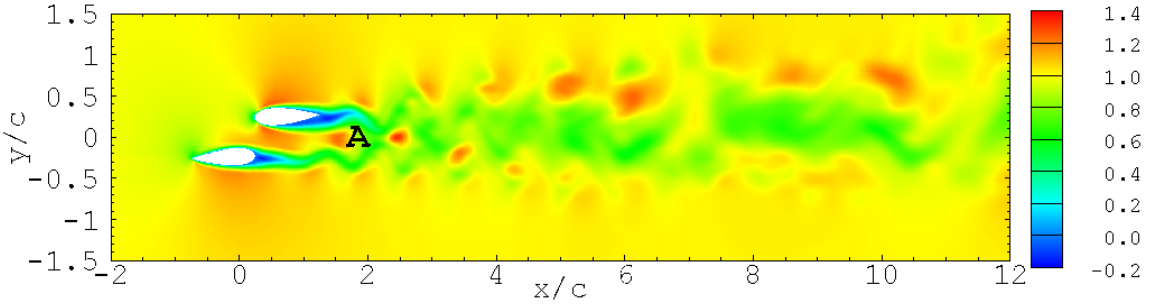

(d) Instantaneous streamwise velocity $\bar{u}/U_\infty$ around two staggered airfoils separated by $T/c = 0.5$ at time $tU_\infty/c = 450$. Point A represents the location of the wake interaction point.

Figure 4.3: Instantaneous streamwise velocity $\bar{u}/U_\infty$ around side-by-side and staggered airfoils aligned at the 1/4 chord point

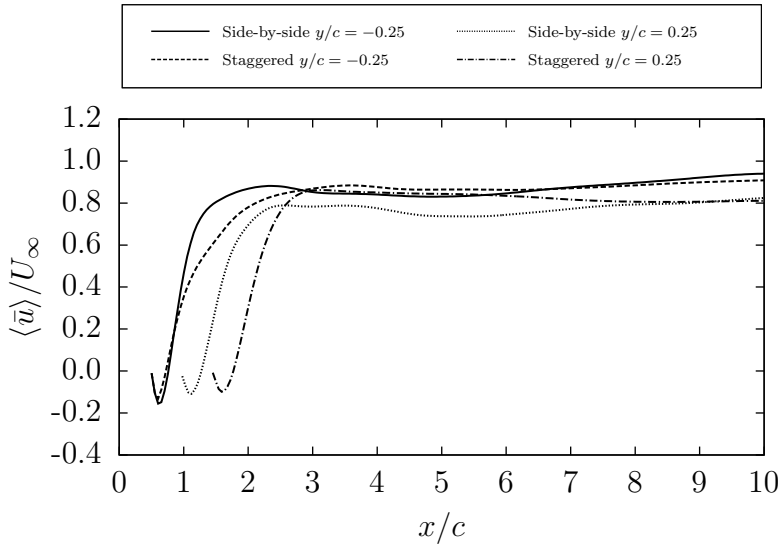

Figure 4.4: Non-dimensional streamwise velocity $\langle\bar{u}\rangle/U_\infty$ profile behind the side-by-side and staggered airfoils. The profiles are located along the centrelines behind the airfoils.

apparent. At $x/c = 1$, only the mean velocity profile for the side-by-side configuration is displayed as this location does not surpass the length of the airfoils for the staggered configuration. It is interesting to observe that the profile of $\langle\bar{u}\rangle/U_\infty$ at $x/c = 1$ for the side-by-side case is similar to that at $x/c = 1.50$ for the staggered case. This shows the mean flow is similar within the near airfoil region before the turbulent wakes of the two airfoils start to merge. At $x/c = 4$, a merging of the wakes can be observed within both the side-by-side and staggered configuration. At $x/c = 7$, the profiles appear very similar to each other indicating a merging of the two wakes. However, as is observable within the staggered configuration for the cylinder simulations, the wakes for the staggered cases, appear biased towards downstream airfoil.

Figure 4.6 displays non-dimensional profiles of the spanwise velocity $\langle\bar{v}\rangle/U_\infty$ for the side-by-side and staggered configurations. The spanwise velocity profiles within the wake appear similar with an exception that at $x/c = 2$, the staggered configuration displays larger spanwise velocities. The higher spanwise velocities are attributable to a smaller distance between the point $x/c = 2$ and the downstream airfoil

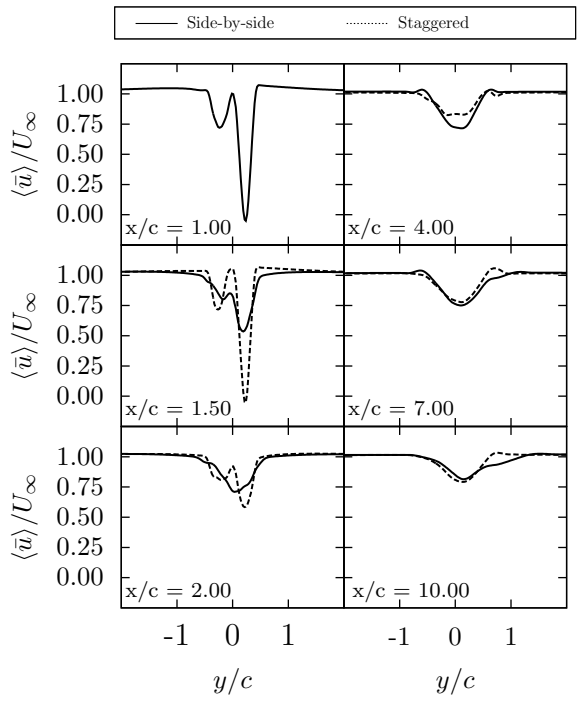

Figure 4.5: Non-dimensional spanwise velocity $\langle\bar{u}\rangle/U_\infty$ profiles at six different streamwise locations behind side-by-side and staggered airfoils. See Figure 4.7 for contours.

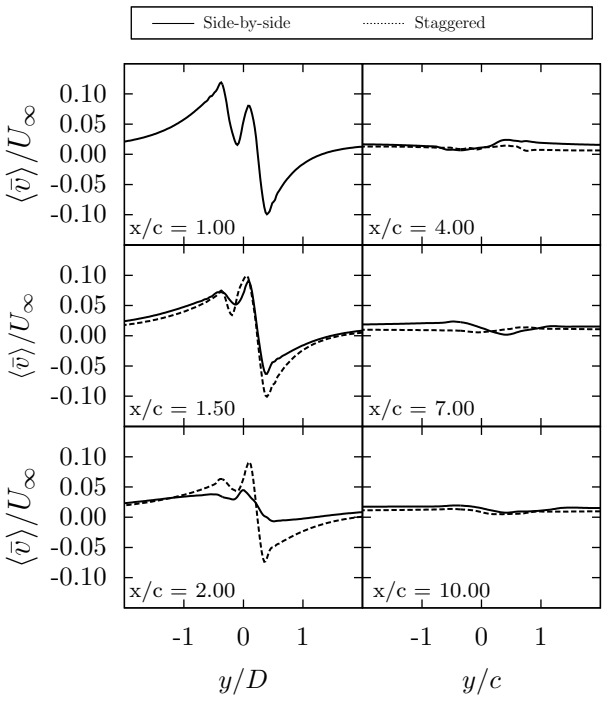

Figure 4.6: Non-dimensional spanwise velocity $\langle\bar{v}\rangle/U_\infty$ profiles at six different streamwise locations behind side-by-side and staggered airfoils. See Figure 4.7 for contours.

within the staggered configuration allowing less time for the flow to merge with the freestream.

Contours of the mean streamwise velocity $\langle\bar{u}\rangle/U_\infty$, presented in Figure 4.5, and mean spanwise velocity $\langle\bar{v}\rangle/U_\infty$, presented in Figure 4.6 around side-by-side and staggered airfoils are shown in Figure 4.7. While the contour plots of the mean streamwise velocities appear similar, a couple of important distinctions are observable. Firstly, a larger streamwise velocity around the airfoils is noted in the side-by-side configuration in comparison to the staggered configuration. The increase in the streamwise velocity identified on the figures at points A and B can be attributed to the increase in the blockage ratio for the side-by-side configuration in comparison to the staggered configuration. While the increase in the streamwise velocity could potentially be

beneficial to the increase the performance of turbines in a farm configuration, this must be weighed against the potential changes in the turbulence levels and the pressure coefficients. Secondly, while the streamwise velocity at points A and B are lower, a velocity increase attributed to the flow passing around the upstream airfoil is observed for the staggered configuration. Depending on the configuration of the airfoils, the downstream airfoil could be located partially or completely within the higher velocity flow passing around the upstream airfoil. The velocity increase for the staggered configuration can also be applied to turbines as Birjandi [36] shows a similar effect occurs for hydrokinetic turbine when an upstream cylinder is positioned in a staggered arrangement to a vertical axis hydrokinetic turbine. Birjandi attributes the decrease in the drag coefficient on the downstream object to the downstream object interacting with the faster flowing fluid moving around the turbine's upstream airfoil. As seen in both the side-by-side and staggered configuration, the spanwise velocity experiences significant increases at the upstream edges of the airfoils, however, the increase within the spanwise velocities are larger within the side-by-side configuration. Similarly, to the streamwise velocity the increase within the spanwise velocities can be related to the increased blockage ratio of the configuration. Due to these significant changes in the velocity and the small magnitude of the spanwise velocities shown in Figure 4.6, the spanwise wake velocities are not distinguishable within the plots, however by examining Figure 4.6 no significant difference which could influence the drag coefficients are observable within the plots.

4.2.2 Turbulence statistics

As the airfoils are much more streamlined in comparison to cylinders, at the low Reynolds number $Re_c = 3000$, the turbulence is caused primarily by the interactions of the wakes.The Reynolds stress needs to be examined as it is related to the

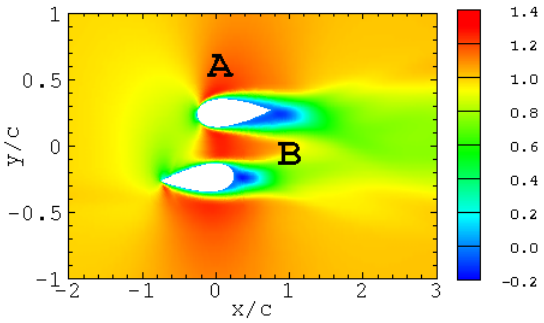

(a) Contour plot of the non-dimensional component streamwise velocity $\langle\bar{u}\rangle/U_\infty$ around side-by-side airfoils separated by $T/c = 0.5$

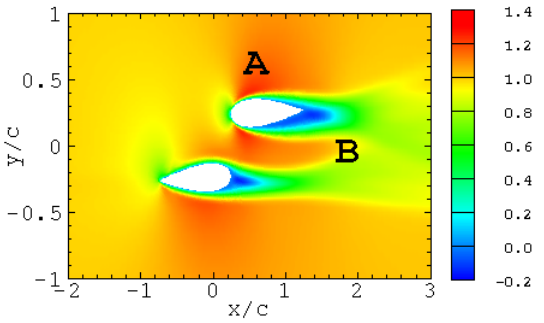

(b) Contour plot of the non-dimensional component streamwise velocity $\langle\bar{u}\rangle/U_\infty$ around staggered airfoils separated by $T/c = L/c = 0.5$

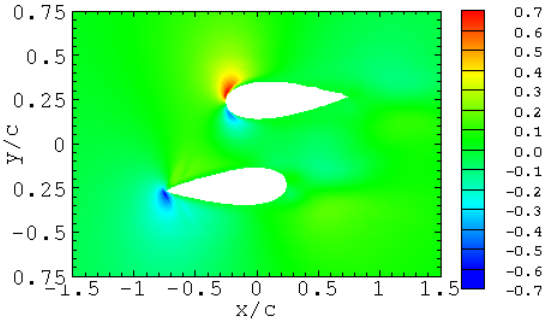

(c) Contour plot of the non-dimensional spanwise velocity $\langle\bar{v}\rangle/U_\infty$ around side-by-side airfoils separated by $T/c = 0.5$

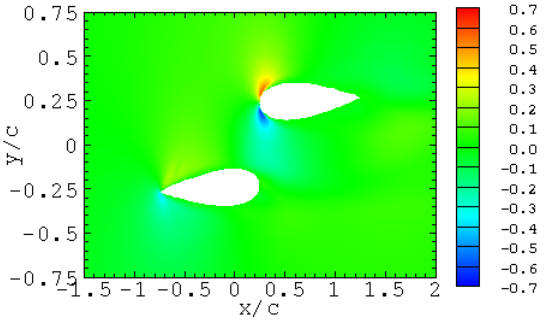

(d) Contour plot of the non-dimensional spanwise velocity $\langle\bar{v}\rangle/U_\infty$ around staggered airfoils separated by $T/c = L/c = 0.5$

Figure 4.7: Contour plots of the velocity $\langle\bar{u}\rangle/U_\infty$ and $\langle\bar{v}\rangle/U_\infty$ around side-by-side and staggered airfoils highlighting several flow differences. For comparative purposes the scales are the same for both the side-by-side and staggered plots.

dissipation and the changes could lead to a mechanism to reduce the drag. Because the wakes are sensitive to the positioning of the airfoils the turbulence level of the flow field varies with the two configurations. Figure 4.8 displays profiles of the Reynolds normal stress component $\langle\bar{u}'\bar{u}'\rangle/U_\infty^2$ around the side-by-side and staggered airfoil configurations. As can be seen from the figure, four distinct peaks are observable within the near wall region for both the side-by-side and the staggered configurations. It should be noted that for the side-by-side configuration, immediate areas of high turbulence are detected within the near-wall region whereas the turbulence levels for the staggered case increase as the interaction point is approached. At $x/c = 7$, the quad peak pattern has transitioned into a dual peak pattern for both configurations;

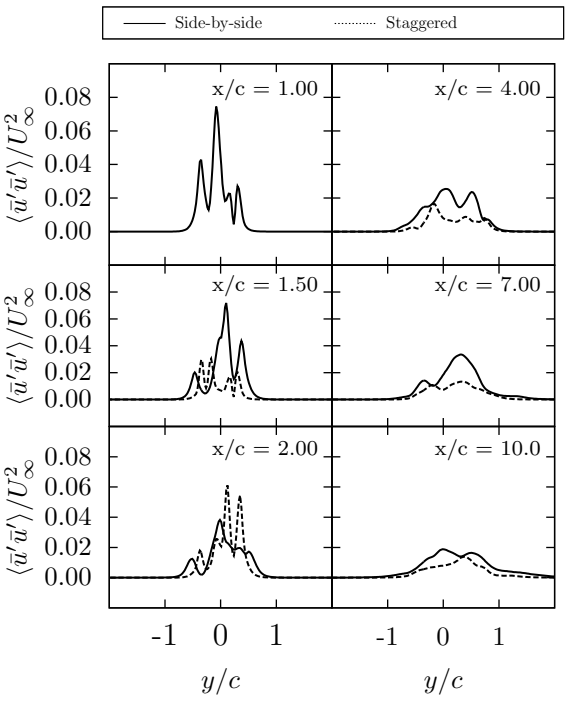

Figure 4.8: Profiles of non-dimensional Reynolds normal stress component $\langle \bar{u}'\bar{u}' \rangle / U_\infty^2$ at six different streamwise locations for side-by-side and staggered airfoils. See Figure 4.10 for contours.

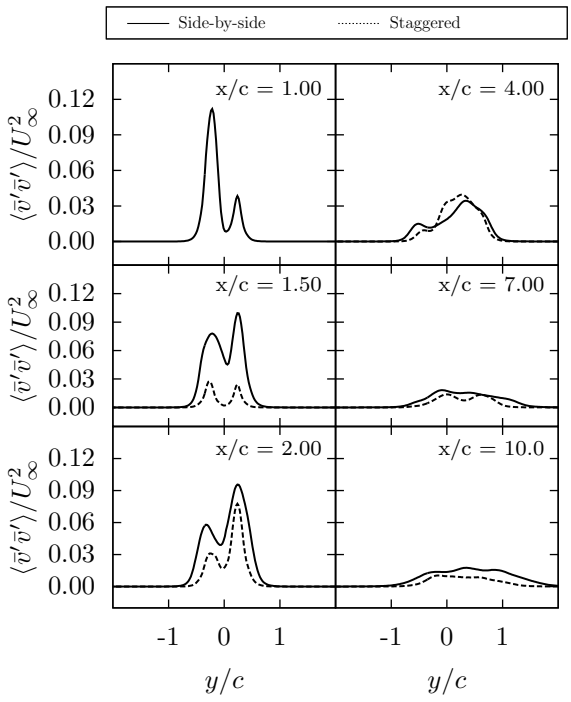

Figure 4.9: Profiles of non-dimensional Reynolds normal stress component $\langle \bar{v}'\bar{v}' \rangle / U_\infty^2$ at six different streamwise locations for side-by-side and staggered airfoils. See Figure 4.10 for contours.

and by $x/c = 10$, the turbulence profiles appear to be very similar.

Figure 4.9 displays profiles of the Reynolds normal stress component $\langle \bar{v}'\bar{v}' \rangle / U_\infty^2$ around the side-by-side and staggered airfoil configurations. As can be seen from the figure, two distinct peaks are observable within the near wall region for both the side-by-side and the staggered configurations. Similarly to the $\langle \bar{u}'\bar{u}' \rangle / U_\infty^2$ component of the Reynolds stress, higher turbulence is detected immediately within the side-by-side configuration in comparison to the staggered configuration. The trend of increased turbulence within the side-by-side configuration is also clearly shown within the previous cylinder flow results within the previous chapter, see Figures 3.14, 3.15, 3.22 and 3.23. At $x/c = 10$, the peaks are merged into a single peak similar to that of a single obstruction.

Similar to the profiles of the Reynolds normal stresses shown in Figures 4.8 and 4.9, the contours of the Reynolds stress components $\langle \bar{u}'\bar{u}' \rangle / U_\infty^2$, $\langle \bar{v}'\bar{v}' \rangle / U_\infty^2$ and $\langle \bar{u}'\bar{v}' \rangle / U_\infty^2$ around the side-by-side and staggered airfoil configurations shown in Figure 4.10 display significantly higher values for the Reynolds stress components within the side-by-side configuration around the upstream airfoil in comparison to that of the staggered configuration. The contour plots have the same scale to ensure an accurate comparison between the two cases and several flow features of interest are highlighted in the plots.

Point A displays four distinct regions of high $\langle \bar{u}'\bar{u}' \rangle / U_\infty^2$ Reynolds stress behind the airfoils in the side-by-side configuration consistent with the formation of two wakes behind each of the airfoils. As the upstream airfoil is facing in the reverse orientation, the flow approaches the tail which behaves as a splitter and gently separates the flow creating less turbulence than the downstream airfoil. The distinct lack of four regions of high $\langle \bar{u}'\bar{u}' \rangle / U_\infty^2$ Reynolds stress behind the staggered airfoils can be attributed to the flow splitting abilities of the backwards facing airfoil, however, for the side-by-side configuration, as the distance from the upstream airfoil is reduced the interaction point of the wakes is closer and the turbulence created causes the flow to separated earlier resulting in the four distinct regions of high $\langle \bar{u}'\bar{u}' \rangle / U_\infty^2$ Reynolds stress. The increased turbulence generated can influence the size of the wake as is observable in the instantaneous velocity contours seen in Figure 4.3. As discussed within the Section 3.2.4, the increased wake size can be attributed to an increase in the drag coefficient.

Similar to point A, points B and C show regions of higher Reynolds stress components $\langle \bar{v}'\bar{v}' \rangle / U_\infty^2$ and $\langle \bar{u}'\bar{v}' \rangle / U_\infty^2$ behind the side-by-side airfoils in comparison to the staggered airfoils. As described for point A, as the proximity of the wake interaction point is closer to the upstream airfoil, the increased turbulence causes earlier

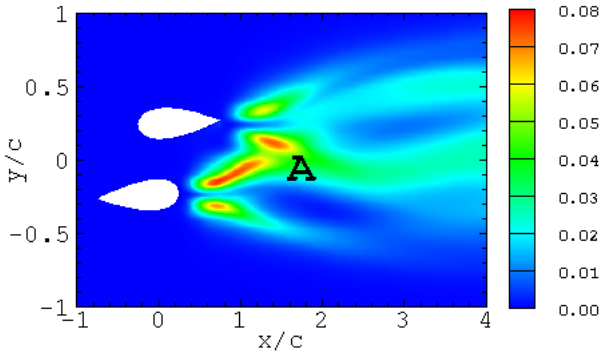

(a) Contour plot of the non-dimensional component of the Reynolds stress $\langle \bar{u}'\bar{u}' \rangle / U_\infty^2$ around side-by-side airfoils separated by $T/c = 0.5$

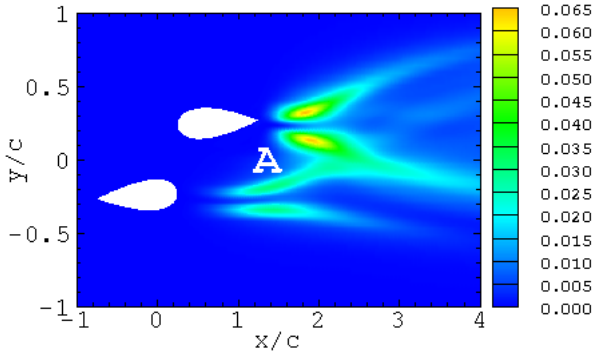

(b) Contour plot of the non-dimensional component of the Reynolds stress $\langle \bar{u}'\bar{u}' \rangle / U_\infty^2$ around staggered airfoils separated by $T/c = L/c = 0.5$

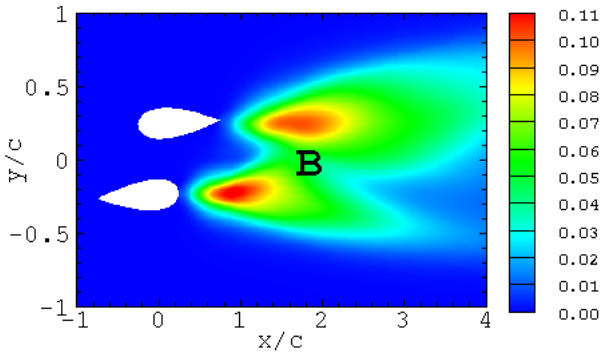

(c) Contour plot of the non-dimensional component of the Reynolds stress $\langle \bar{v}'\bar{v}' \rangle / U_\infty^2$ around side-by-side airfoils separated by $T/c = 0.5$

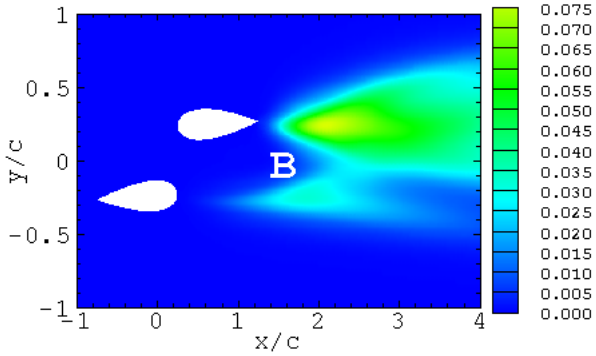

(d) Contour plot of the non-dimensional component of the Reynolds stress $\langle \bar{v}'\bar{v}' \rangle / U_\infty^2$ around staggered airfoils separated by $T/c = L/c = 0.5$

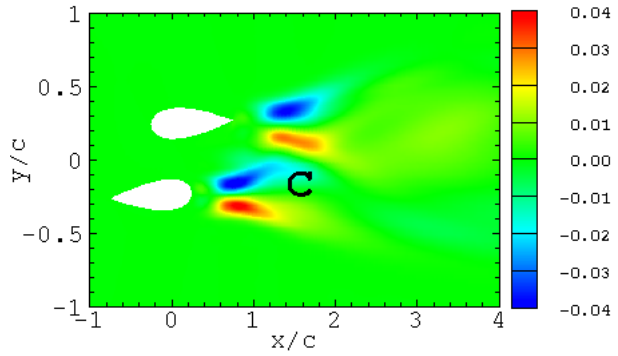

(e) Contour plot of the non-dimensional component of the Reynolds stress $\langle \bar{u}'\bar{v}' \rangle / U_\infty^2$ around side-by-side airfoils separated by $T/c = 0.5$

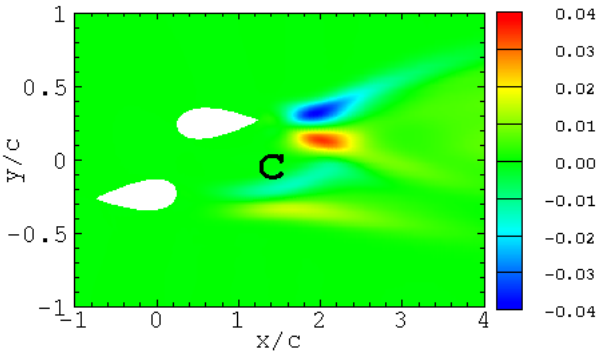

(f) Contour plot of the non-dimensional component of the Reynolds stress $\langle \bar{u}'\bar{v}' \rangle / U_\infty^2$ around staggered airfoils separated by $T/c = L/c = 0.5$

Figure 4.10: Contour plots of the Reynolds stress components $\langle \bar{u}'\bar{u}' \rangle / U_\infty^2$, $\langle \bar{v}'\bar{v}' \rangle / U_\infty^2$ and $\langle \bar{u}'\bar{v}' \rangle / U_\infty^2$ around side-by-side and staggered airfoils highlighting several flow differences. For comparative purposes the scales are the same for both the side-by-side and staggered plots.

separation on the upstream airfoil resulting in an increase within the turbulence behind the airfoils and this can result in an increase to the drag coefficients acting around the airfoils. Furthermore, while the Reynolds shear stress $\langle \bar{u}'\bar{v}' \rangle / U_\infty^2$ increases behind the upstream airfoil for the side-by-side configuration, the levels remain similar to those observed behind the downstream airfoil of the staggered configuration; for the downstream airfoil no significant differences are observed between the configurations. Based upon the contour plots of the $\langle \bar{u}'\bar{v}' \rangle / U_\infty^2$ Reynolds shear stress, the configuration should not present an increased danger to fish. Hammar *et al.* [88] examined the influence of hydrokinetic turbines on fish and determines that arrays are not dangerous to fish, however, they may restrict the passage of fish.

4.2.3 Force coefficients, pressure coefficients and Strouhal number

To understand the drag coefficients acting upon the airfoil configurations, it is required to present the pressure coefficients acting around the side-by-side and staggered airfoils as shown in Figure 4.11. Point A highlights the low pressure region which forms behind the airfoils. As the pressure coefficients are displayed using the same scale, a significantly larger low pressure region is visible within the side-by-side configuration in comparison to the staggered configuration and consequently, as the pressure difference is larger for the side-by-side configuration an increase in the drag coefficient is expected.

Table 4.2 presents the force coefficients acting upon the airfoils. Using the side-by-side configuration as a reference, the staggered configuration exhibits a 19.8% reduction in drag for the upstream airfoil and 19.6% reduction in drag for the downstream airfoil. The results are consistent with the previous chapter in which the staggered cylinders results in less drag than the side-by-side cylinders. Based upon the examination of the

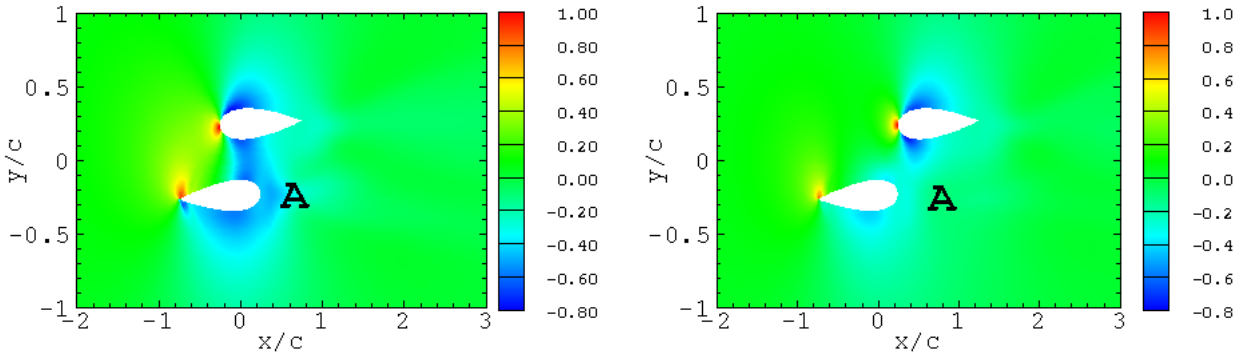

(a) Contour plot of the pressure coefficients around the side-by-side airfoils separated by $T/c = 0.5$

(b) Contour plot of the pressure coefficients around the staggered airfoils separated by $T/c = L/c = 0.5$

Figure 4.11: Contour plots of the pressure coefficients around side-by-side and staggered airfoils with the differences highlighted at point A

Table 4.2: Force coefficients around two stationary airfoils

Side-By-Side Configuration		
	Drag	**Lift**
Upstream Airfoil	0.202	-0.482
Downstream Airfoil	0.134	0.133
Staggered Configuration		
	Drag	**Lift**
Upstream Airfoil	0.161	-0.279
Downstream Airfoil	0.112	0.047

flow around two airfoils, we postulate that the reduction in the drag coefficients for the staggered configuration can be attributed to the positioning of the downstream airfoil being located within the higher velocity flow passing around the upstream airfoil, the decrease in wake turbulence in the $\langle \bar{u}'\bar{u}' \rangle / U_\infty^2$, $\langle \bar{v}'\bar{v}' \rangle / U_\infty^2$ and $\langle \bar{u}'\bar{v}' \rangle / U_\infty^2$ Reynolds stress components and a lower pressure difference between the front the back of the airfoils. It is expected that such results will change when the airfoils rotate and the added complexity of each airfoil rotating will add a further complexity to the physics of minimization of drag.

The periodic Kármán vortex shedding for the side-by-side and staggered airfoils is characterized using the Strouhal number defined as $St = fT/U_\infty$, where T is the spanwise separation distance between the airfoils measured from the outer edges

of the airfoils. The frequency f for each of the airfoils is determined from a fast Fourier transform of the time series of the lift coefficient [82]. For the side-by-side configuration the Strouhal number of the configuration is calculated to be 0.170 and for the staggered configuration the Strouhal number is calculated to be 0.151. Turki *et al.* [89] examined the Strouhal numbers for a square cylinder and determined that the Strouhal number increased with the blockage ratio which is consistent with the current results. Furthermore, a Strouhal number can be calculated for each of the individual airfoils using the chord thickness as the characteristic length. For the side-by-side configuration the Strohaul numbers are calculated to be 0.161 and 0.212 for the upstream and downstream airfoils respectively whereas for the staggered configuration the Strouhal numbers are calculated to be 0.170 and 0.215 for the upstream and downstream airfoils respectively. The results from the Strouhal numbers show that the configuration has a clear influence on the vortex shedding of the airfoils behind each of the airfoils and on the configuration as a whole.

While studies examining the positioning of airfoils for turbine applications are relatively few, positioning is employed by several forms of fauna including geese and herrings. Geese are known for their V-shaped flying formation. There are several theories which attempt to cause of the V-formation including the hypothesis that the V-formation reduces the risk of collisions. An in-line arrangement possesses collision risks should the leading animal stop suddenly whereas a side-by-side arrangement would be susceptible to a strong flanking gust of wind causing a collision [90]. Even so, research shows that the V-formation offers drag reductions ranging from 16% [91] to 36% [92] based upon simplified computational simulations in which the geese are modelled using two airfoils. While the angle of attack, orientation and type of airfoils are different compared to those used in hydrokinetic turbine applications, the drag reductions are comparable to those found in the current study. While fish schools including species such as the herring have been noted to employ the staggered

configurations, the positioning of fish tend to be more unstructured and unsystematic, even so Marras [93] found that any schooling type behaviour of fish tended to decrease the energy output of the fish. Furthermore, Dabiri [38] proposed using schools of fish as the basis for a wind turbine farm set-up, and within the set-up the individual turbines are positioned in a staggered configuration. In the paper, Dabiri [38] shows that the performance of the array would increase with the proposed fish inspired design.

4.3 Experimental validation and wake

The experimental analysis aims to validate the numerical predictions of the flow around side-by-side and staggered stationary airfoils aligned at the $\frac{1}{4}$ chord point by experimentally quantifying the effects of positioning on the wake statistics. To validate the numerical simulations, the airfoils are positioned in the same configurations as the numerical simulations. Figure 4.1 shows the two configurations. As described in the test matrix, see Table 4.1 on page 60, the side-by-side and staggered configurations are examined at two different streamwise locations and the wake statistics are measured using acoustic doppler velocimetry and to make use of the available resources. Unlike Chapter 3, where there was experimental data avaliable from the literature to validate the cylinder results, it was not possible to find such validation data for interacting stationary airfoils with the same geometery as the numerical simulations.

4.3.1 Experimental setup

A recirculating water tunnel facility located at the Univeristy of Manitoba is used to perform the validation experiments. The tunnel has a vertical flow loop configuration

Figure 4.12: Test section of the water tunnel used for the side-by-side and staggered airfoil experiments

with a single stage axial propeller pump to circulate the water and the pump is driven by a variable speed induction motor to control the flow rate of the tunnel. A 61 cm wide by 183 cm long test section allows for a maximum flow rate of 362 L/s at the maximum water tunnel height of 60 cm. For the full water height, a maximum velocity of 1.1 m/s can be achieved within the test section, however, to match the Reynolds number of $Re_c = 3,000$ used within the numerical simulations, a velocity of 0.1 m/s is used throughout all the experiments. The vortices generated by the pump are reduced by an upstream honeycomb causing the turbulence in the test section to be less than 3% of the maximum velocity. Figure 4.12 shows the test section of the water tunnel used throughout the experiments.

Two identical NACA 0021 aluminum airfoils with a chord length of 3 cm are used in the experiments. The airfoils are 75.5 cm in length and are designed such that when positioned on top of a 0.9535 cm plate on the bottom of the water tunnel they can be secured in place using a bar which sits on the two sides of the water tunnel's upper rim. The plate ensures that the airfoils remain stationary within the flow and the

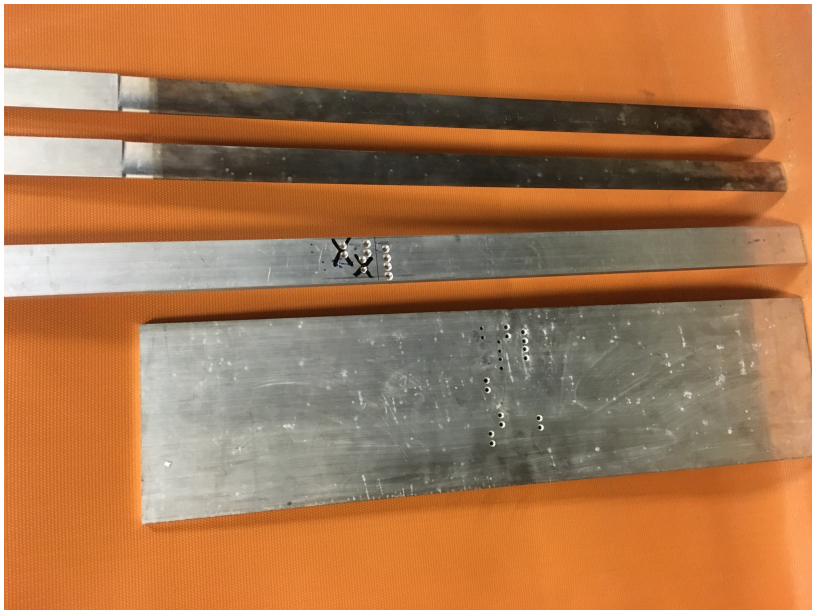

Figure 4.13: Components used in the side-by-side and staggered airfoil experiments. Experimental components include two NACA 0021 airfoils, a bar and a plate shown from top to bottom in the picture.

bar ensures that the airfoils are held under compression minimising vibrations. To facilitate the manufacturing process of the airfoils, a square section of length 15.5 cm is located on the end of the airfoils situated above the water level. Figure 4.13 shows the airfoils, the plate and the bar which are used throughout the experiments.

As can be seen in Figure 4.13, the plate contains sets of holes allowing for the positioning of the airfoils. The pairs of holes on the plate are slightly offset such that when aligned with the holes located on the bottom and top faces of the airfoils, and angle of 2° is imparted to the airfoils. The holes within the top and bottom faces of the airfoils and those on the plates are machined at precise locations in order to obtain separation distances of $T/c = 0.5$ for the side-by-side configuration and $T/c = L/c = 0.5$ for the staggered configuration.

4.3.2 Experimental proceedure

The experiments are performed in the water tunnel shown in Figure 4.12. First the components are secured within the water tunnel. To secure the ADV in the flow, an aluminum frame with a sliding mount is clamped to the two sides of the water tunnel's upper rim. Reference marks located along the upper rim of the water tunnel are used to located the planes $x/c = 4$ and $x/c = 7$. To align the ADV in the spanwise direction the ADV is first aligned with the centerline of the airfoils through reference marks on the top bar and several distance measurements and by noting the position of one edge of the sliding ADV mount, reference marks are imparted onto the aluminum frame. The markings on the frame provide an efficient means with which to determine the spanwise measurement positions at a given streamwise location. As the airfoils can be approximated as infinite length, the depth measurement depth does not influence the results, however, to ensure no contamination of the results due to boundary layer and free-stream effects, the measurements are taken at half the water tunnel depth.

The airfoils are positioned into the water tunnel through the use of reference marks located along the upper rim of the water tunnel. Before being put into the water tunnel the airfoils are securely connected to a plate shown in Figure 4.13. A top bar constrained the airfoils within the tunnel and is used to position the airfoils within the streamwise direction. The configuration of the airfoils, side-by-side versus staggered, is selected via holes in the bottom plate. The plate rests on the bottom of the water tunnel. To ensure no boundary layer effects from the walls the airfoils are positioned near the centerline of the channel. Figure 4.14 shows the set-up for the airfoils in the experiments.

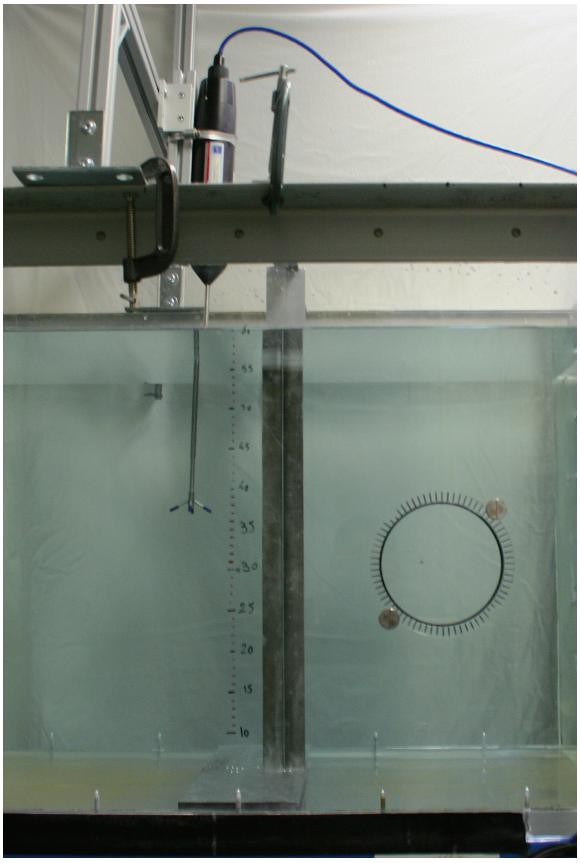

Figure 4.14: Experimental set-up for the side-by-side airfoils in the water tunnel. The ADV is attached to a frame location downstream of the airfoils.

4.3.3 Flow measurements using ADV

An ADV is a point based flow measurement device for velocity and turbulence measurements. The Nortek Vectrino+ ADV is used for the velocity measurements in the vicinity of the airfoils. The ADV and measurement probe is shown in Figure 4.15. The ADV contains four velocity probes, one probe for the streamwise direction, one probe for the spanwise direction and 2 probes for the depth direction. The process of obtaining a velocity measurement involves the emission of a short acoustic pulse from the transmitter elements located on the measurement probe of the ADV. The pulse travels through the fluid to a focal point for the instruments receiver beams and is reflected back by sound-scattering particles present in the water. The particles are assumed to move at the water's velocity and the doppler shift from the echo

of the acoustic pulse for each of the receiver beams is analysed to determine the velocity of the components of the flow. In the experiments 20 μm particles are used to ensure that the signal is reflected. Additionally, the signal to noise ratio and the correlation values are used to determine the quality and accuracy of the data. For accurate ADV measurements, the minimum acceptable correlation is reported to be 80% [94], however for all measurements, the correlation is maintained at about 90%. For these experiments, the laboratory probe is used which can acheive a sampling rate of 200 Hz.

While an ADV is considered to be a highly accurate measurement device with a relative error of $\pm 0.5\%$ of the measured velocity and an absolute error of $\pm$1mm [94], the return signal contains noise and spikes along with the velocity readings. Based upon the studies of Martin [95] and Khorsandi [96], the noise creates an insignificant effect on the mean statistics of the flow, however, spikes within data create a significant effect on the mean flow statistics. ADV data spikes typically occur when air bubbles pass through the acoustic pulses or the focal point of the beams. These spikes can contribute to significant errors in the mean velocity and turbulence, however, these spikes are identifiable as shown in Figure 4.16 and are removed from the dataset using a hybrid procedure developed by Birjandi and Bibeau [97].

As the ADV measurement device is an intrusive device within the flow, a sufficient amount of space is required to accommodate the measurement probe of the device. Due to the small size of the airfoils constrained by the Reynolds number, $Re_c = 3,000$, the closest distance behind the airfoils which could be measured is $x/c = 4$. Due to this constraint, only the locations $x/c = 4$ and 7 are considered.

Figure 4.15: Nortek Vectrino^{+} ADV used for the measurements

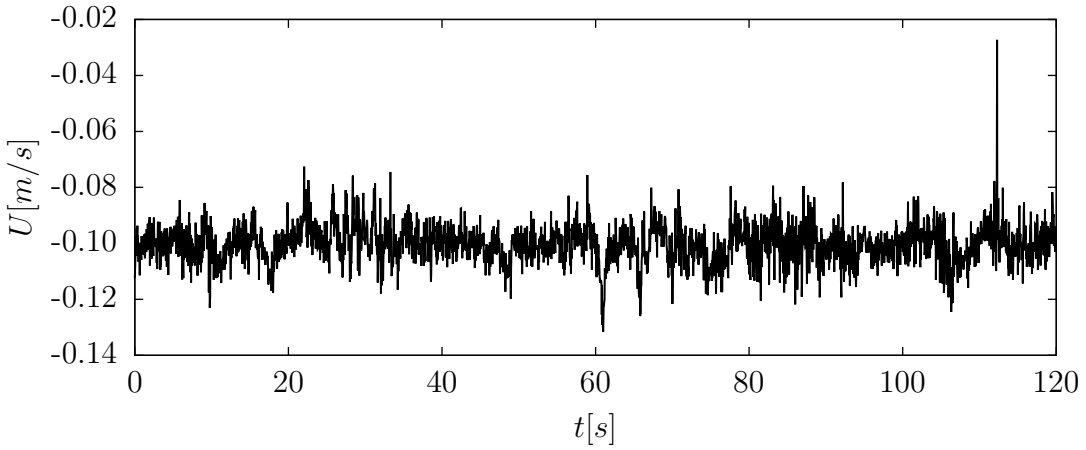

Figure 4.16: Sample ADV dataset for the flow around side-by-side airfoils. A significant spike is located in the dataset around $t = 110$ s and is removed using the filtering proceedure developed in reference [97].

4.3.4 Measurement uncertainty

Reference [98] defines Type A and Type B as two approaches to estimate the uncertainty of a measurement. Type A uncertainty also referred to as the standard deviation of the mean or the standard error of the mean, is calculated from a dataset containing repeated readings whereas Type B uncertainty is calculated from the measurement uncertainty associated with the measurement equipment. The uncertainty of a measurement instrument is typically provided in the calibration certificate of the instrument and the uncertainty reported in the calibration certificate of an instrument is usually assumed to be normally distributed [99]. To obtain an overall quantity for the uncertainty of individual measurements, the individual uncertainties associated with the experiments are estimated and are combined. For the ADV, Type A uncertainty is calculated for a set of readings as follows

$$u_A = \frac{s}{\sqrt{n}} \tag{4.1}$$

where s is the computed estimated standard deviation and n is the number of data points within the dataset. Type B uncertainty is calculated for a dataset according to

$$u_B = \frac{a}{2} \tag{4.2}$$

in which a is the semi-range or the half-width between the upper and lower limits of the uncertainty of the measurement instrument. The combined standard uncertainty is then calculated from Type A and Type B standard uncertainties using the sum of the squares as follows

$$u_C = \sqrt{u_A^2 + u_B^2} \tag{4.3}$$

As the combined standard uncertainty is equivalent to one standard deviation, the confidence interval of the combined uncertainty is 68%. By multiplying the combined standard uncertainty by a coverage factor k, the uncertainty can be computed for higher confidence intervals. A coverage factor of 2 provides a 95% confidence interval and a coverage factor of 3 provides a 99.7% confidence interval.

The ADV measures the flow velocity with an accuracy of ±0.5% of the measured velocity ±1 mm/s. The accuracy of the position measurements is estimated to be ±0.25 mm. While the uncertainty of the streamwise velocity is a function of the measured velocity, due to the low velocity of 0.1 m/s and the very small contribution of 0.5%, the absolute error of the ADV is significantly larger than the relative error. Furthermore, due to the two minute data collection window, the Type A error is also small. Therefore, for all the streamwuse velocity measurements the error is determined to be ±2 mm with a confidence interval of 95%. As the turbulence measurements, vary significantly due to the presence of the wake, the maximum error in the turbulence measurements is determined to the ±0.02 mm. While the streamwise velocity is measurable by the ADV, the spanwise velocity is on the same order of magnitude as the absolute error of the ADV and as no means exist with which to remove the large source of error in the spanwise velocity, only the streamwise velocity characteristics are examined experimentally. For clarity reasons, error bars are not included in the plots presented in the following sections.

4.3.5 Experimental results

In order to determine the water tunnel motor frequency to produce the desired velocity of 0.1 m/s, velocity measurements are taken every 0.1 Hz throughout the frequency range of 5 Hz to 6 Hz, by adjusting the frequency drive. For each of the measurements, the velocity is recorded for one minute at 200 Hz and a motor frequency of 5.9 Hz is found to provide the desired freestream velocity of 0.1 m/s. Based upon ADV flow measurements for the water tunnel, a streamwise turbulence intensity of 1% is obtained. As shown in the test matrix, Table 4.1, for all measurements, the ADV collects data at a frequency of 200 Hz for two minute intervals to obtain flow validation data.

Within the numerical simulations, uniform flow with no turbulence intensity, 0%, is applied at the inlet, however, while the water tunnel used within the experiments uses an upstream honeycomb to reduce the turbulence intensity at the inlet, based upon the calibration tests, a streamwise turbulence intensity of 1% is obtained throughout the channel. Although the turbulence intensity is relatively low, the increased turbulence causes several discrepancies between the numerical and experimental results can be directly attributed to the increased turbulence within the experimental set-up in comparison to the LES simulations.

Figures 4.17 and 4.18 show the non-dimensional streamwise velocity profiles for the experimental and numerical results at two different downstream locations. While both the side-by-side and staggered configurations show an excellent agreement between the experimental and numerical data for $x/c = 4$, a slight overprediction of the streamwise velocity defect within the numerical results compared to the experimental results is noted at $x/c = 7$. The overprediction of the velocity defect is directly attributable to the increased turbulence within the experimental set-up in comparison to the numerical simulations. An increase in the turbulence intensity of the flow causes

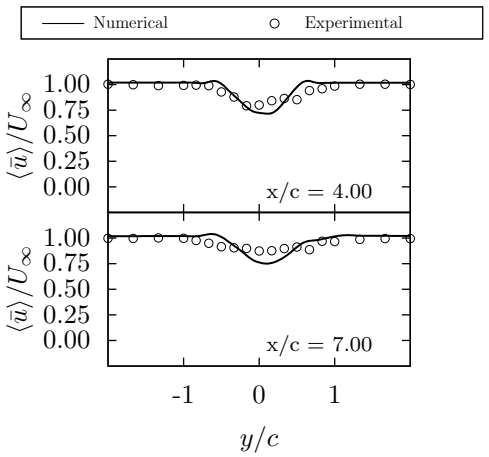

Figure 4.17: Spanwise velocity profiles of $\langle\bar{u}\rangle/U_\infty$ at two different streamwise locations behind side-by-side airfoils compared to the numerical results.

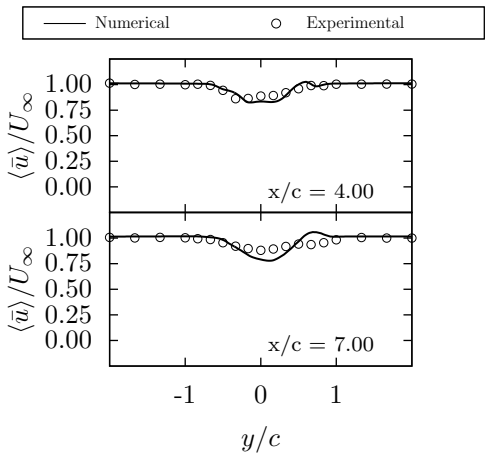

Figure 4.18: Spanwise velocity profiles of $\langle\bar{u}\rangle/U_\infty$ at two different streamwise locations behind staggered airfoils compared to the numerical results.

an increase in mixing and dissipation within the flow resulting in a reduced wake length.

For hydrokinetic turbine farm applications, large turbulence intensities are generated in a river system upwards of 10% in certain case [100], and this can cause significant mixing resulting in significant reductions in the length of the velocity defect. The decreased length of the velocity defect is beneficial to hydrokinetic turbine farms, as the reduced wake length enables turbine rows to be positioned closer together in the streamwise direction resulting in a potential increase to the turbine density and an increased levelized cost of energy for the site.

Figures 4.19 and 4.20 show the non-dimensional Reynolds normal stress component $\langle\bar{u}'\bar{u}'\rangle$ profiles for the experimental and numerical results at two different downstream locations. Due to the low Reynolds number $Re_c = 3,000$ used in the numerical simulations, turbulence is triggered primarily by the wake interactions and the turbulence levels are highly susceptible to the distance between the wake interaction point and the airfoils. In the experiments, however, the increased ambient turbulence levels in the flow, cause earlier separation for the flow around the airfoils in both

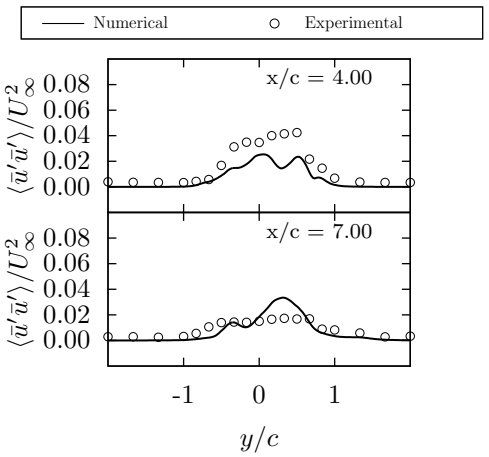

Figure 4.19: Reynolds normal stress component $\langle \bar{u}'\bar{u}' \rangle / U_\infty^2$ at two different streamwise locations behind side-by-side airfoils compared to the numerical results.

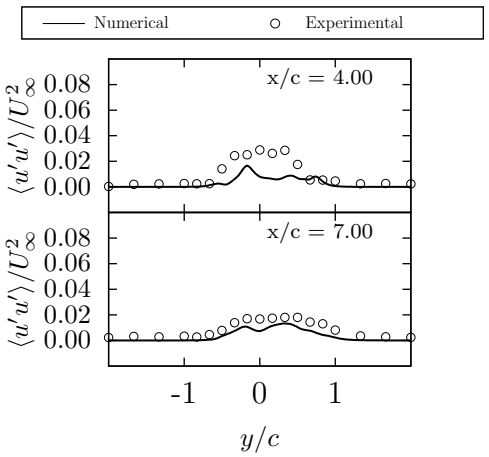

Figure 4.20: Reynolds normal stress component $\langle \bar{u}'\bar{u}' \rangle / U_\infty^2$ at two different streamwise locations behind staggered airfoils compared to the numerical results.

the side-by-side and staggered configurations, and consequently an increase in the turbulence levels within the wake are observed experimentally compared to the numerical simulations. At $x/c = 4$, significantly higher turbulence levels are present in the experiments in comparison to the numerical simulations, however, at $x/c = 7$ the turbulence levels are much closer to the turbulence levels predicted by the numerical simulations due to the additional mixing and dissipation caused by the ambient and increased turbulence. The lack of two distinct peaks at $x/c = 4$, further suggests an increase in mixing as only a single peak is visible after the wakes merge.

Although the turbulence results differ within the experiments in comparison to the numerical simulations, the side-by-side configuration still displays higher turbulence levels in the wake region when compared to the staggered configuration. The increased turbulence levels within the side-by-side configuration validates the turbulence conclusions reached from the numerical results as the results are observable experimentally. Furthermore, the experiments indicate that while the ambient turbulence levels influence the formation of eddies and the vortex shedding around airfoils, the increased turbulence within the side-by-side configuration is caused by the configuration and

should be present within an actual hydrokinetic turbine farm. Furthermore, based upon the conclusions drawn from the numerical airfoil simulations and the cylinder simulations in Chapter 3, an increase in the drag coefficients should be observable in the side-by-side configuration.

4.4 Summary of the Chapter

The current chapter examined wall resolved LES predictions of the turbulent wake around side-by-side and staggered NACA 0021 airfoils for $Re_c = 3,000$. Firstly, due to the streamlined nature of the airfoils, a more streamlined wake develops behind the airfoils. Consequently, the streamwise and spanwise separation distances between the airfoils is set to $L/c = 0.5c$ and $T/c = 0.5c$ to ensure wake interactions between the airfoils. The first order statistics show a more pronounced velocity increase within the separation gap for the side-by-side configuration and the second order statistics show an increase in the generated turbulence from the side-by-side configuration. The increase in turbulence is attributed to an increase in the proximity of the wake interaction point to the upstream airfoil causing a change within the separation point of the flow and the turbulence. Additionally, a decrease in the drag coefficients is be noted for the staggered configuration in comparison to the side-by-side configuration. The staggered configuration exhibits a 19.8% reduction in drag for the upstream airfoil and 19.6% reduction in drag for the downstream airfoil.

Experimental studies are also performed to validate the results from the numerical simulations. Due to an ambient turbulence intensity within the water tunnel during the experiments, the numerical results differ slightly from the measurement data. Furthermore, similar to the numerical simulation, an increase in the turbulence for the side-by-side configuration in comparison to the staggered configuration is

Table 4.3: Findings for side-by-side and staggered stationary airfoils

Simulation/-Experiment	**Reynolds Number**	**Objective Number on page 5**	**Findings**
LES of side-by-side airfoils	3,000	3	Results showed significantly higher levels of turbulence behind the airfoils and a larger low pressure region behind the airfoils. Higher velocities around the airfoils are present due to the increased blockage ratio of the configuration. Increased drag coefficients are noted in comparison to the staggered configuration.
LES of staggered airfoils	3,000	3	Results showed significantly lower levels of turbulence behind the airfoils and a smaller low pressure region behind the airfoils. The staggered configuration exhibits a 19.8% reduction in drag for the upstream airfoil and 19.6% reduction in drag for the downstream airfoil when compared to the side-by-side configuration.
Experimental validation of side-by-side airfoils	3,000	4	Results are validated using an ADV in a water tunnel. Results for the streamwise velocities are in good agreement with the numerical results, however, an increased ambient turbulence level within the water tunnel in comparison to the CFD caused higher turbulence in the experimental results.
Experimental validation of staggered airfoils	3,000	4	Results are validated using an ADV in a water tunnel. Results for the streamwise velocities are in good agreement with the numerical results. While an increased turbulence within the experiments is also noted for the staggered configuration, the turbulence levels found experimentally are significantly lower than those of the side-by-side configuration.

also observed in the experiments. Table 4.3 summarises the two numerical and experimental cases examined within the current chapter and which objectives were addressed in the simulations and experiments.

The results from the airfoil simulations and experiments present the influences of the side-by-side configuration in comparison to the staggered configuration. The results indicate that for hydrokinetic turbine farm applications that staggered turbines will contain lower drag coefficients attributable to the increased wake turbulence and pressure differences within the side-by-side configuration. While both the numerical and experimental results are limited to stationary airfoils in this chapter, in the next chapter, the study is extended to include the effects of two rotating airfoils on the turbulent wakes approaching the physical domain of two interacting hydrokinetic turbines.

Chapter 5

Rotating airfoils

The current chapter examines the effects of turbine positioning and rotational direction on the performance of two vertical axis hydrokinetic turbines in 2-D and low solidarity. The goal is to provide a first level analysis into the interactions between two vertical axis hydrokinetic turbines, as detailed in the 5^{th} objective in Chapter 1 on page 5. The methodology is to use CFD to provide insights into the effects of turbine positioning and rotation on the drag coefficients. The simulated turbines consist of two rotating airfoils and the drag coefficients on both airfoils are examined to analyze the changes in performance. The numerical results are not validated — the CFD results for two rotating turbines could not be validated in the existing water tunnel and there is no experimental data avaliable in the literature.

Although the Reynolds number can fluctuate significantly in the different types of hydrokinetic turbine applications, it is typically situated within the range $Re_d = 5\times10^5$ to 1×10^7 based upon the turbine diameter and the freestream speed of the flow. The tip speed ratio (TSR) of actual hydrokinetic turbines are typically designed to operate within the range $\lambda = 2$ to 3. Because the operational Reynolds number range of hydrokinetic turbines far exceeds the computational resources available for LES, it

is proper to consider the RANS approach in numerical studies. In order to provide a comprehensive investigation into the effects of turbine spacing and rotational direction, 22 numerical simulations are performed using the RANS approach as shown in Table 5.1. Furthermore, in order to compromise the computational expenses, the Reynolds number is reduced to $Re_d = 10,000$ and the TSR is selected to be 2. The well-known k-ω-SST turbulence model is selected as the model has been well documented for kinetic turbine [9], general turbo-machinery [101], and aerospace [10] applications. Table 5.1 displays the test matrix for the current chapter. A particular focus is given to the staggered configurations due to the reduced drag coefficients in the stationary cylinder and airfoils simulations.

Throughout the remainder of the current chapter the 22 configurations are referred to using the identifiers presented in the computational test matrix. For the staggered configurations, the origin is located at the center of the upstream turbine and the upstream turbine is always provided a clockwise rotational direction. The location of the downstream turbine is important to the investigation as the location of the turbine determines the orientation of the two airfoils closest to the separation gap. As discovered within the previous chapter, the orientation of the airfoils can influence the formation of the wake. Throughout this chapter, the individual airfoils are referenced as airfoil 01, airfoil 02, airfoil 03 and airfoil 04. For all configurations, airfoil 01 and airfoil 02 are assigned a counter-clockwise rotational direction during both the co- and counter-rotating simulations. Airfoil 03 and airfoil 04 are assigned counter-clockwise rotation during the co-rotating simulations and clockwise rotation during the counter-rotating simulations. For the staggered configuration, airfoil 03 and airfoil 04 are situated on the downstream turbine, whereas airfoil 01 and airfoil 02 are situated upon the upstream turbine. Figure 5.1 presents four different turbine configurations described in Table 5.1.

Table 5.1: Computational test matrix for the turbine simulations

ID	Configuration	Rotation	T/d	L/d
A	Side-By-Side	Co-rotating	0	1.5
B	Side-By-Side	Co-rotating	0	2
C	Side-By-Side	Co-rotating	0	2.5
D	Side-By-Side	Counter-rotating	0	1.5
E	Side-By-Side	Counter-rotating	0	2
F	Side-By-Side	Counter-rotating	0	2.5
G	Staggered	Co-rotating	1.5	1.5
H	Staggered	Co-rotating	2	2
I	Staggered	Co-rotating	2.5	2.5
J	Staggered	Counter-rotating	1.5	1.5
K	Staggered	Counter-rotating	2	2
L	Staggered	Counter-rotating	2.5	2.5
M	Staggered	Co-rotating	-1.5	1.5
N	Staggered	Co-rotating	-2	2
O	Staggered	Co-rotating	-2.5	2.5
P	Staggered	Counter-rotating	-1.5	1.5
Q	Staggered	Counter-rotating	-2	2
R	Staggered	Counter-rotating	-2.5	-2.5
S	Staggered	Co-rotating	1	2
T	Staggered	Co-rotating	- 1	2
U	Staggered	Counter-rotating	1	2
V	Staggered	Counter-rotating	-1	2
Details				
All simulations are performed using OpenFOAM v2.3.0 using a RANS turbulence model with the k-ω-SST turbulence model. The Reynolds number for all the simulations is $Re_d = 10,000$ based upon the turbine diameter. The TSR remains constant throughout the simulations and is set to $\lambda = 2$. For the staggered simulations the origin is located at the upstream turbine. The individual airfoils are referenced as airfoil 01, airfoil 02, airfoil 03 and airfoil 04.				

5.1 Computational domain and boundary conditions

For the turbine simulations, the computational domains are designed to include two circular regions for each of the hydrokinetic turbines within a stationary 2-D rectangular region. The rectangular region contains two cut-outs to house the circular

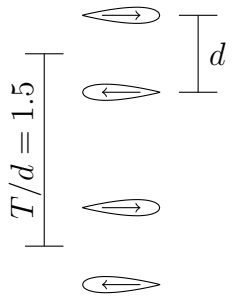

(a) Case A: Co-rotating side-by-side turbines separated by $T/d = 1.5$

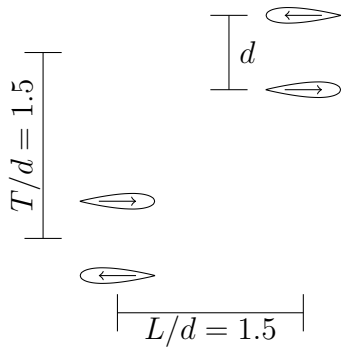

(b) Case J: Counter-rotating staggered turbine configuration separated by $T/d = L/d = 1.5$

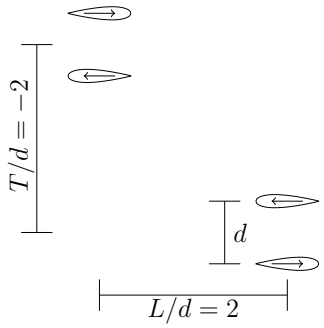

(c) Case Q: Counter-rotating staggered turbines configuration separated by $T/d = -2$ and $L/d = 2$

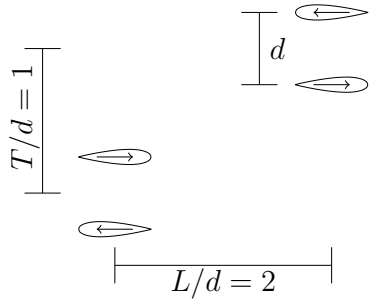

(d) Case U: Counter-rotating staggered turbines configuration A separated by $T/d = 1$ and $L/d = 2$

Figure 5.1: Schematic of several selected side-by-side and staggered turbine configurations under co-rotating and counter-rotating conditions

regions and the circular regions are provided with an angular velocity to create the mesh rotation. The angular velocity is determined based on obtaining a TSR value, $\lambda = 2$. For each turbine, the rectangular and the circular domains are linked only via cyclic boundary conditions to allow for the mesh rotation. The turbines consist of two NACA 0021 airfoils and a small structured region is provided around each airfoil. Within the structured region, a C-grids are selected as the C-grid reduces the complexity and non-orthogonality of the mesh around the trailing edge of the airfoils. Figure 5.2 shows an up-close view of the structured mesh around one of the airfoil pairs within one of the rotating domains.

As can be seen within Figure 5.2, the remainder of the rotating domain is meshed

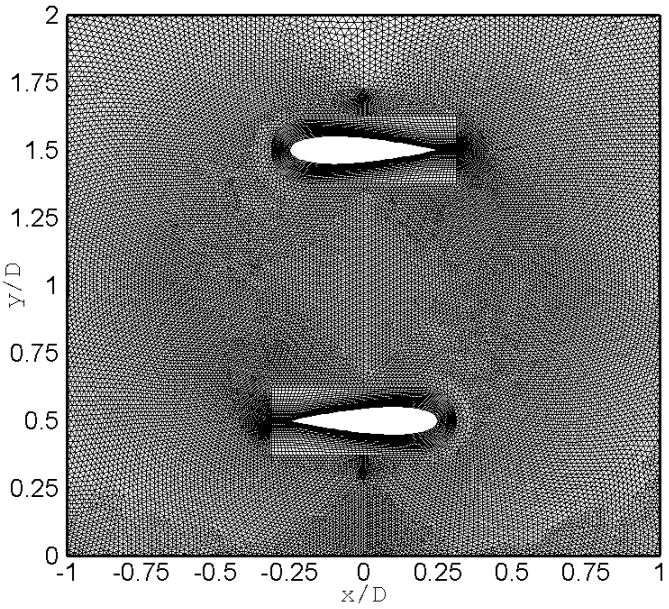

Figure 5.2: Mesh around a pair of rotating airfoil

using an unstructured grid due to the complexity created by the circular shape of the domains. To modify the turbine configuration, the cut-outs and circular mesh regions are shifted around within the rectangular domain. An unstructured mesh is selected for use within the stationary domain. Figure 5.3 shows a view of a few of the domains within the vicinity of the two turbines for several selected cases. The rotational direction of the turbines is also shown in the figure.

The origin for the turbine simulations is set at the centre of the separation gap within the vertical direction whereas within the streamwise direction, the origin is located at the centre of the furthermost upstream turbine. The inlet is positioned $5d$ upstream of the turbine configurations and the domains size is slightly modified to ensure that the configurations are positioned $5d$ away from the upper and lower boundaries of the domain. The outlet is positioned $15d$ downstream of the turbines to ensure that the boundary is sufficiently far away such that any wake interactions are able to develop. It is important to properly capture the wake dynamics and interactions as they affect

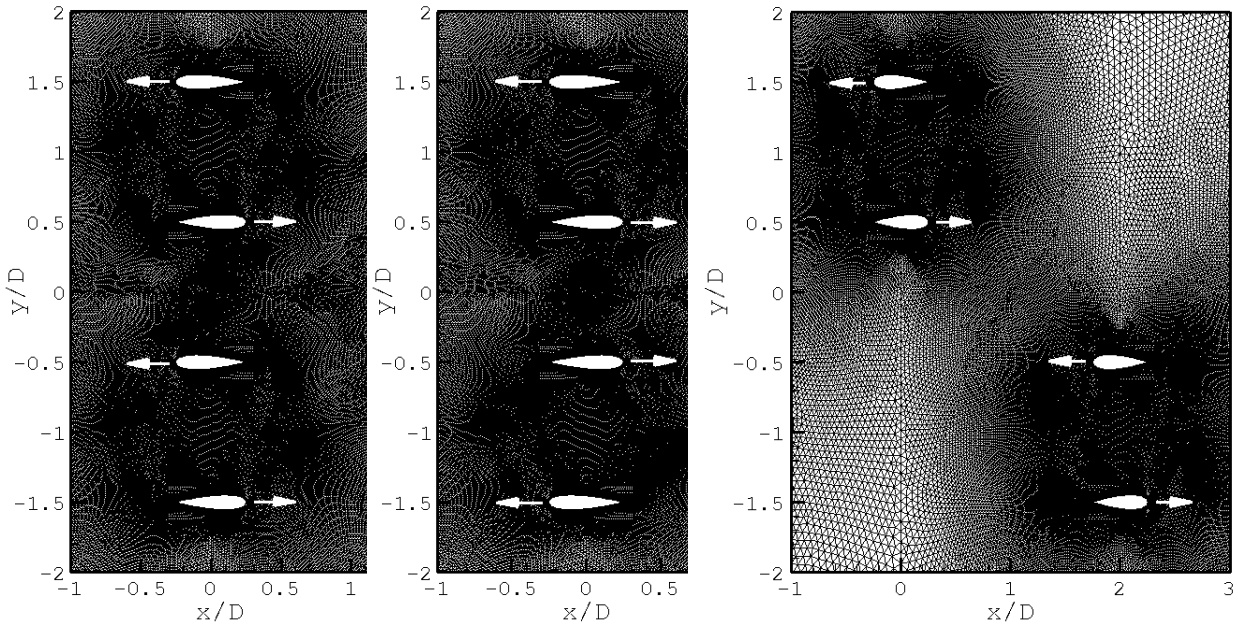

(a) Co-rotating side-by-side turbines with separation distance $T/d = 2$

(b) Counter-rotating side-by-side turbines with separation distance $T/d = 2$

(c) Co-rotating staggered turbines with separation distances $T/d = L/d = 2$

Figure 5.3: Snapshot of the computational domain for case B, E and H

the drag coefficients of the turbine blades. A uniform velocity profile is applied to the inlet, a zero gradient boundary condition is applied to the outlet, and a symmetry boundary condition is applied to the top and bottom edges. As previously stated, cyclic boundary conditions are applied to the edges of the rotating regions so that the edges, or the circular cut-outs, allow the flow to pass between the domains.

5.2 Results

The focus is more on drag results with less focus on the velocity and turbulence results. Time averaged results are not presented due to the computational costs, however, transicent results of the velocity are discussed for several selected cases. Furthermore, the instantaneous force coefficients throughout a single rotational period

Table 5.2: Grid independence test for the co-rotating turbines within a side-by-side configuration with a separation distance of $T/d = 2$.

Average drag coefficient				
	Airfoil 01	Airfoil 02	Airfoil 03	Airfoil 04
Coarse	0.011558	0.011557	0.011567	0.011566
Medium	0.011508	0.011508	0.011554	0.011554
Fine	0.011520	0.011520	0.011555	0.011555
Percent Difference compared to the fine grid				
	Airfoil 01	Airfoil 02	Airfoil 03	Airfoil 04
Coarse	-0.33%	-0.32%	-0.40%	-0.40%
Medium	0.10%	0.10%	-0.30%	-0.30%

are examined to understand how the configuration and rotational direction influence the average force coefficients during a single rotational period. To ensure the quality of the numerical results, a grid independence study is also conducted.

5.2.1 Grid independence test

The current section examines the results from a grid independence test conducted upon the side-by-side turbine with a separation distance of $T/d = 2$ following the approaches of Ferziger [102] and Akbarzadeh [103]. Co-rotation is employed within these simulations. Three different mesh resolutions are examined including a coarse mesh ($50,000$ elements), a medium mesh ($100,000$ elements) and a fine mesh ($200,000$ elements), and the average drag coefficient during a rotational period is compared based on each of the four airfoils. Table 5.2 summarizes the results of the simulations and the percent differences when compared to the fine grid.

As seen in Table 5.2, it is apparent that the average drag coefficients vary by a maximum of 0.4% indicating that grid independent results are obtained. As such, for the 22 simulations, the medium grid is selected. The coarse grid is rejected as it contained several grid spacing challenges which required special attention.

5.2.2 Instantaneous velocity contours

In order to understand the flow around two hydrokinetic turbines in close proximity, Figure 5.4 shows the instantaneous u/U_∞ velocity around configurations A, H and U respectively as defined in Table 5.1. It should be noted that while the contour plots shown a maximum u/U_∞ velocity of 2.2 for all of the cases a maximum u/U_∞ velocity of 5 is observed on the leading edge of the airfoils, however, for clarity the contour plots are scaled to better represent the overall flow.

As can be seen in the figure, the turbine configuration is shown to have a significant impact on the formation and the length of the wake. For configuration A, in which the turbines are positioned side-by-side, a high velocity region is observed in the separation gap between the turbines. The increased velocity within the separation gap is consistent with the preliminary cylinder and airfoil analysis in which higher velocity was observed in the separation gap for the side-by-side configurations. For configurations H and U a significant reduction in the wake length is observed in comparision to the side-by-side turbines.

5.2.3 Average drag coefficients

Table 5.3 presents the drag coefficients on the airfoils for each configuration shown in Figure 5.1. Table 5.4 presents the percent difference between the turbine configurations for the co-rotating cases. Each case is compared to case A, the side-by-side configuration separated by $T/d = 1.5$. Table 5.5 presents the percent difference between the turbine configurations for the counter-rotating cases. Similarly to the co-rotating analysis, each case is compared to the case A, the side-by-side configuration separated by $T/d = 1.5$. Table 5.6 presents the percent difference of the same turbine configuration between the co- and counter-rotations.

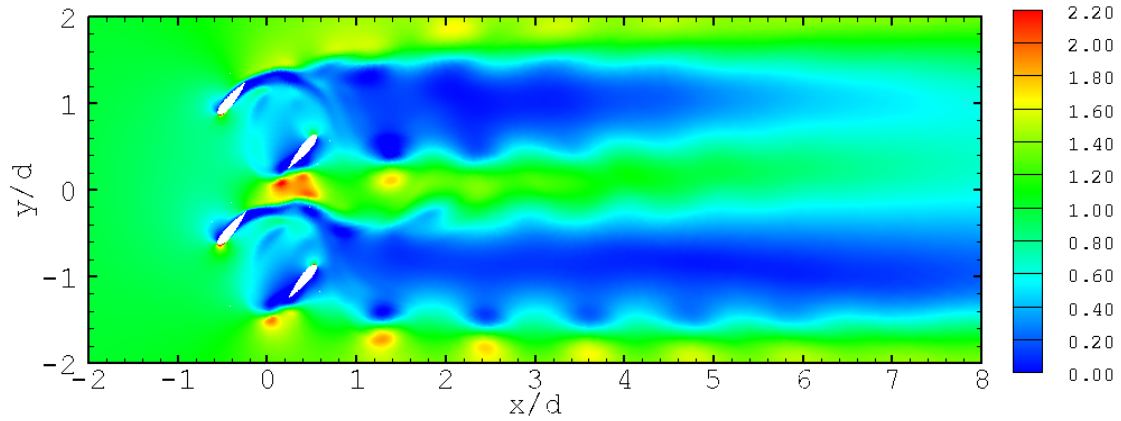

(a) Instantaneous streamwise velocity u/U_∞ around side-by-side turbines separated by $T/d = 1.5$ at time $tU_\infty/d = 406.25$.

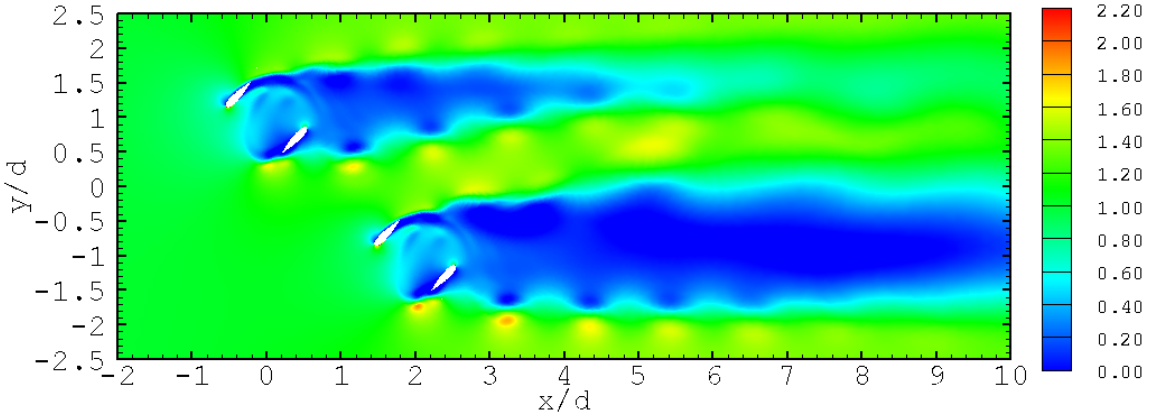

(b) Instantaneous streamwise velocity u/U_∞ around staggered turbines separated by $T/d = L/d = 2$ at time $tU_\infty/d = 410$.

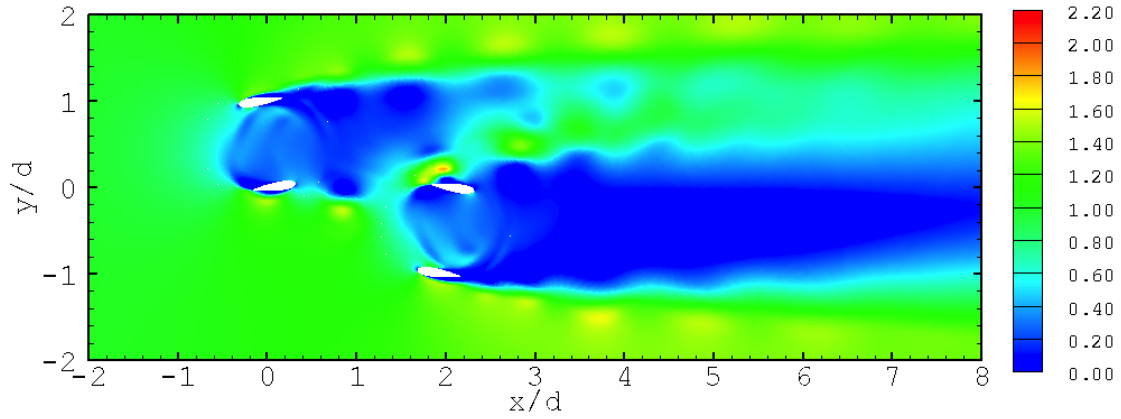

(c) Instantaneous streamwise velocity u/U_∞ around staggered turbines separated by $T/d = 1$ and $L/d = 2$ at time $tU_\infty/d = 456.25$.

Figure 5.4: Instantaneous streamwise velocity u/U_∞ around side-by-side and staggered turbines.

Table 5.3: Average drag coefficient under co- and counter-rotating conditions

Co-rotating Turbines				
ID	Airfoil 01	Airfoil 02	Airfoil 03	Airfoil 04
A	0.01231	0.01231	0.01183	0.01183
B	0.01151	0.01151	0.01155	0.01155
C	0.01121	0.01122	0.01129	0.01129
G	0.01070	0.01070	0.01128	0.01128
H	0.01102	0.01102	0.01165	0.01169
I	0.01139	0.01139	0.01172	0.01173
M	0.01088	0.01088	0.01135	0.01135
N	0.01114	0.01114	0.01157	0.01157
O	0.01144	0.01145	0.01167	0.01167
S	0.01019	0.01019	0.01002	0.01002
T	0.01021	0.01021	0.01048	0.01047
Counter-rotating Turbines				
D	0.01167	0.01167	0.01167	0.01167
E	0.01132	0.01132	0.01131	0.01132
F	0.01110	0.01110	0.01110	0.01110
J	0.01077	0.01077	0.01134	0.01133
K	0.01104	0.01104	0.01165	0.01165
L	0.01136	0.01136	0.01172	0.01172
P	0.01088	0.01089	0.01131	0.01125
Q	0.01116	0.01116	0.01159	0.01160
R	0.01146	0.01146	0.01170	0.01170
U	0.01018	0.01018	0.01060	0.01059
V	0.01020	0.01020	0.00997	0.01003

Table 5.4: Percent difference between the co-rotating turbine configurations (with respect to the side-by-side case A in which $T/d = 1.5$)

ID	Airfoil 01	Airfoil 02	Airfoil 03	Airfoil 04
A	0.00%	0.00%	0.00%	0.00%
B	6.53%	6.53%	6.15%	6.15%
C	8.91%	8.91%	8.30%	8.30%
G	13.06%	13.09%	8.41%	8.35%
H	10.46%	10.51%	5.41%	5.06%
I	7.52%	7.52%	4.78%	4.76%
M	11.60%	11.60%	7.83%	7.84%
N	9.50%	9.50%	6.04%	6.04%
O	7.06%	7.04%	5.25%	5.22%
S	17.23%	17.24%	18.61%	18.62%
T	17.05%	17.06%	14.92%	14.93%

Table 5.5: Percent difference between the counter-rotating turbine configurations (with respect to the side-by-side case A in which $T/d = 1.5$)

	Airfoil 01	Airfoil 02	Airfoil 03	Airfoil 04
D	0.00%	0.00%	0.00%	0.00%
E	3.03%	3.03%	3.05%	3.04%
F	4.87%	4.86%	4.87%	4.86%
J	7.68%	7.69%	2.86%	2.87%
K	5.40%	5.39%	0.19%	0.20%
L	2.66%	2.66%	-0.44%	-0.45%
P	6.76%	6.68%	3.07%	3.59%
Q	4.38%	4.41%	0.67%	0.56%
R	1.77%	1.76%	-0.24%	-0.29%
U	12.74%	12.74%	9.18%	9.24%
V	12.59%	12.63%	14.54%	14.02%

Table 5.6: Percent difference between the co-rotating and counter-rotating conditions for the same configuration

	Airfoil 01	Airfoil 02	Airfoil 03	Airfoil 04
A and D	5.22%	5.22%	1.33%	1.34%
B and E	1.67%	1.67%	2.08%	2.07%
C and F	1.01%	1.01%	1.67%	1.67%
G and J	-0.66%	-0.67%	-0.52%	-0.45%
H and K	-0.14%	-0.20%	-0.01%	0.37%
I and L	0.24%	0.24%	0.02%	0.03%
M and P	0.03%	-0.06%	0.32%	0.84%
N and Q	-0.15%	-0.12%	-0.20%	-0.31%
O and R	-0.18%	-0.16%	-0.27%	-0.30%
S and U	0.08%	0.07%	-5.77%	-5.71%
T and V	0.11%	0.16%	4.80%	4.20%

By examining Table 5.4, several important observations are noted. Firstly, an increase of the separation distance T/d for the side-by-side configuration results in a decrease in the drag coefficients. For the staggered configuration, an increase of the separation distances $T/d = L/d$ results in an increase in the drag coefficients. Furthermore, when $T/d = \pm 1$ and $L/d = 2$, a significant decrease in the drag coefficient is observed compared to all the other configurations, indicating that the vertical separation distance T/d, provides a much more significant influence on the drag coefficient than does the horizontal separation distance L/d.

It is interesting to observe that the results from the co-rotating simulations are consistent with the results for stationary cylinders reported in the literature (see section 1.4). For two side-by-side cylinders, the Sumner [24] shows that for cylinders within the range $1 < T/d < \infty$, the drag coefficient decreases as the separation distance increases. While a decrease in the drag coefficients is noted within the range $T/d < 1$, such a close spacing would be infeasible for hydrokinetic turbines due to safety, maintenance and retrieval concerns. As the force coefficients for the staggered configurations are dependent upon the incidence angle α, to obtain a definitive pattern similar to the side-by-side configuration can be difficult. Nevertheless, the general trends within the literature indicate that as T/d and L/d increase the drag coefficient acting on the cylinders decrease [24, 32].

By examining Table 5.5, similar trends under the co-rotating conditions are observed. The side-by-side configuration results in a decrease in the drag coefficient when the separation distance is increased and the staggered configuration results in a decrease in the drag coefficient when the separation distance is decreased. As is evident in Table 5.6, no statically significant advantages of counter-rotation can be concluded based on the results as all configurations show less than a $\pm 5.5\%$ difference between the results. Furthermore, for most of the configurations, the percent difference between the co- and counter-rotating simulations are within $\pm 1\%$ indicating that the rotational direction produces no discernible impact on the force coefficients.

It should be indicated that although the performance gains for counter-rotation appear to have statistically insignificant impacts with respect to the value of the force coefficients, there are many other parameters (such as the thrust coefficient, power coefficients and wake properties) that are important for evaluating improvement to the performance of vertical axis hydrokinetic turbines. Furthermore, due to the simplifications used within the CFD processes, other factors such as 3-D effects could

influence the wakes and force coefficients.

5.2.4 Instantaneous drag coefficients

Figure 5.5 and 5.6 show the instantaneous drag coefficients acting upon each of the four airfoils over a single rotational period for both side-by-side and staggered configurations under co- and counter-rotating conditions. For the side-by-side configuration, the separation distance is set to $T/d = 2$, and for the staggered configuration, the separation distance is set to $T/d = L/d = 2$. As can be seen by examining the Figures 5.5 and 5.6, the instantaneous force coefficients of airfoil 01 and airfoil 02 appear very similar. This further leads to the identical averaged drag coefficients. Due to the differences in the rotational direction applied to airfoil 03 and airfoil 04 for the co- and counter-rotating simulations, their profiles appear mirrored. This shows that while counter-rotation does influence the position at which the maximum drag coefficients occurs, the magnitude of the maximum drag coefficient remains unchanged.

Figure 5.7 compares the drag coefficients for the side-by-side configuration with separation distance $T/d = 2$ and the staggered configuration with separation distance $T/d = L/d = 2$. As can be seen from Figure 5.7, a significantly lower peak drag coefficient is observed within the staggered configuration in comparison to the side-by-side configuration. Furthermore, within the remainder of the profile, a very similar drag coefficient is observed between the staggered and side-by-side configuration, indicating that the drag coefficient reduction in the staggered configurations results from a reduction in the peak drag coefficient of the airfoils.

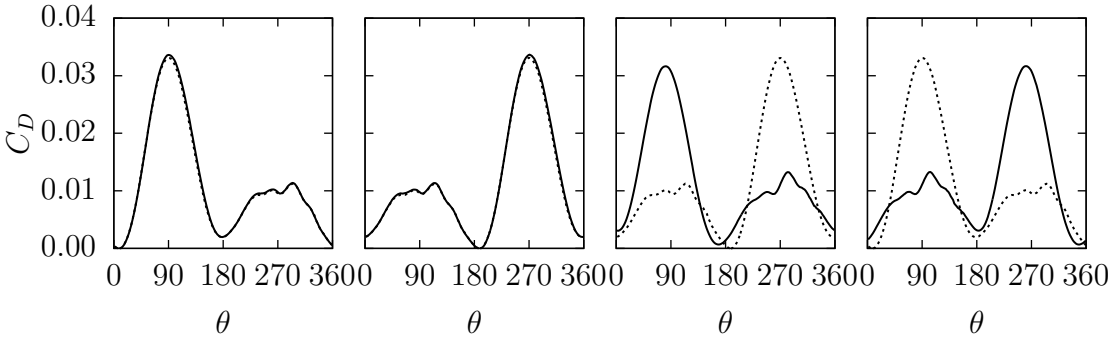

(a) Airfoil 01 (b) Airfoil 02 (c) Airfoil 03 (d) Airfoil 04

Figure 5.5: Drag coefficient during a single rotational period for the side-by-side configuration with $T/d = 2$. Solid line: co-rotation, dashed line counter-rotation

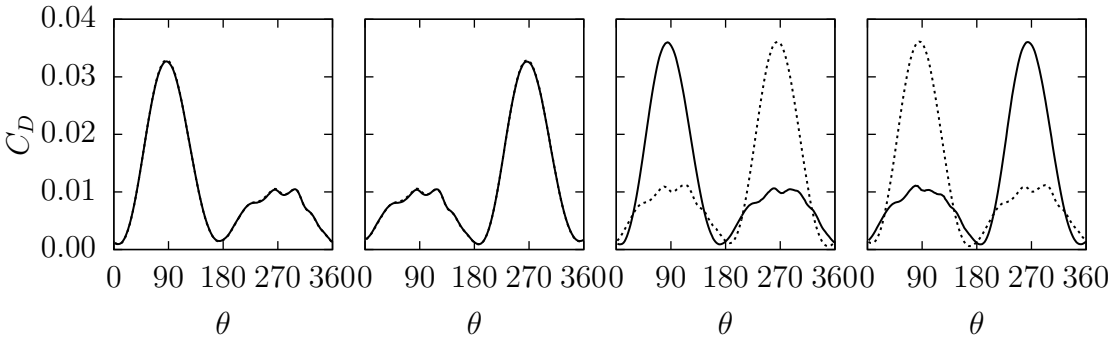

(a) Airfoil 01 (b) Airfoil 02 (c) Airfoil 03 (d) Airfoil 04

Figure 5.6: Drag coefficient during a single rotational period for the staggered configuration with $T/d = L/d = 2$. Solid line: co-rotation, dashed line: counter-rotation

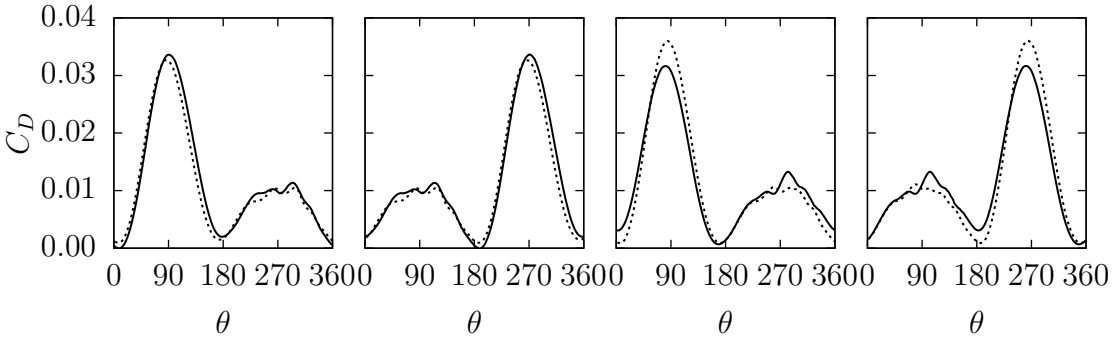

(a) Airfoil 01 (b) Airfoil 02 (c) Airfoil 03 (d) Airfoil 04

Figure 5.7: Comparison of the drag coefficient during a single rotational period for the side-by-side configuration with $T/d = 2$ and the staggered configuration with $T/d = LD = 2$. Solid line: side-by-side, dashed line: staggered

5.3 Summary of the Chapter

The current chapter examined the effects of turbine positioning and rotation on two hydrokinetic turbines operating in close proximity using a RANS turbulence modelling approach. The current chapter performed multiple simulations of the flow around two vertical axis turbines using RANS for $Re_d = 10,000$ to determine the effects of positioning and rotation on the lift and drag coefficients as detailed in the 5^{th} objective in Chapter 1 on page 5. For the side-by-side configurations, an increase of the separation distance T/d causes a decrease in the drag coefficients whereas for the staggered configurations, an increase of the separation distance T/d and L/d leads to an increase in the drag coefficients. The trends observed from the turbine simulations are similar to as those observed in the literature for two cylinder configurations. When identical spacings are used to examine the effects of co-rotation versus counter-rotation, no statistical differences were observed. An examination of the instantaneous drag coefficients over a single rotational period was conducted, and the results show the apparent differences the side-by-side and staggered simulations, however, minimal differences are observed between the co- and counter-rotating conditions. Finally, it should be indicated that although the simulations provide valuable insight into the effects of turbine positioning and rotation on the performance, there are other parameters (such as the thrust and power coefficients) which require closer examinations to fully understand the effects of positioning and rotational direction on the performance of two closely spaced vertical axis hydrokinetic turbines.

Chapter 6

Conclusions and Future Studies

CFD demonstrates that the positioning of two closely spaced hydrokinetic turbines is an important parameter on the performance of these devices. In the current research, LES and RANS are used to investigate the effects of position and rotation. Firstly a single, side-by-side and staggered stationary cylinders arrangements are investigated using wall resolved LES, with the SM. Secondly, side-by-side and staggered airfoil arrangements are examined uses wall resolved LES along with ADV measurements to validate the numerical results. Finally, 22 rotating turbine cases are examined using the RANS method with the k-ω-SST turbulence model.

Chapter 3 examines the interactions between two cylinders using wall resolved LES. For the single cylinder case, the SM and the DSM are examined and the SM is found to provide results in greater agreement with the experimental data of Lourenco and Shih [16] and Ong and Wallace [12]. For the side-by-side configuration with a separation distance of $T/D = 1.5$, the flow is found to be bi-stable and fluctuate between two different regimes whereas the staggered configuration contains only a single regime. The research examines the velocity and turbulence profiles, the pressure coefficients around the cylinders and the force coefficients. Based on a comprehensive

literature review, it is believed that Chapter 3 presents the first comprehensive set of wake profiles for the side-by-side configuration averaged over both regimes and the first comprehensive set of wake profiles for the flow over staggered cylinders. The profiles enable a deeper understanding of how two wakes merge and interact. A drag coefficient of $C_D = 1.299$ and 1.306 is obtained for the side-by-side cylinders compared to $C_D = 1.252$ and 1.152 for the staggered cylinders. The higher velocity passing around the upstream cylinder, lower wake turbulence and decreased pressure difference between the front and back of the cylinders is attributed to the decrease in the drag coefficients.

Chapter 4 performes wall resolved LES for turbulent wakes around the airfoils aligned at the $\frac{1}{4}$ chord point. A decrease in turbulence is observed within the staggered configuration due to the increased distance from the airfoils to the wake interaction point. The drag coefficient results are also examined and determined to be consistent with the results from the cylinder simulations; for the side-by-side airfoils, drag coefficients of $C_D = 0.202$ and 0.134 are obtained and for the staggered airfoils, drag coefficients of $C_D = 0.161$ and 0.112 are obtained. A Strouhal number of 0.170 is obtained for the side-by-side configuration compared to 0.151 for the staggered configuration. Experimental studies are also performed in a water tunnel to validate the results from the numerical simulations. Due to an ambiant turbulence intensity within the water tunnel, the numerical results differ slightly from the measurement data.

Chapter 5 examines the influence of positioning and rotational direction of two hydrokinetic turbines. The goal of this section is to examine the trends between the results and for this application the RANS turbulence modelling method is more than sufficient. Three major trends are observed and are summarized as follows:

(1) An increase of the separation distance results in a decrease in drag for the side-

by-side configuration.

(2) A decrease of the separation distance results in a decrease in drag for the staggered configuration.

(3) Counter-rotation results in a statistically insignificant change within the drag coefficients compared to an equivalent co-rotating case.

A maximum drag reduction of 17.06% is obtained for the co-rotating staggered turbines separated by $T/D = -1$ and $L/D = 2$ when compared to a base case of co-rotating side-by-side turbines separated by $T/D = 1.5$. The maximum difference between co- and counter rotation was determined to be 5.77%, however, on average the results differed by less than 1%.

6.1 Recommendations for future research

The following research subjects are recommended for further study on the effects of turbine positioning and the effect of rotational direction on the performance of vertical-axis hydrokinetic turbines:

1. Perform turbine interaction simulations using the LES turbulence modelling technique instead of the RANS technique. While LES adds significantly to the computational costs, the additional physics provided by the simulations allow for a greater understanding of the mechanisms involved.

2. Examine the influence of turbine positioning and rotational direction on additional parameters such as the lift, thrust, torque and power. All these parameters are important to the performance of vertical-axis hydrokinetic turbines. Furthermore, an extended examination into the effects of the TSR and the Reynolds number on the spacing requirements and turbine rotation

are required to develop a more comprehensive understanding of the turbine performances.

3. In this research, turbulent flows around cylinders and airfoils of infinite height are studied, which implies that the flows are statistically homogeneous along the cylinders and airfoils. In future studies, it would be beneficial to consider finite-height cylinders and airfoils. As such, the operating characteristics of a realistic 3-D model of a vertical-axis hydrokinetic turbine can be investigated, which will provide further insights into the effects of the supporting parts of the turbine, free surface and turbulent coherent structures on the boundary layers and turbulent wakes. In addition, the realistic 3-D model of a vertical-axis hydrokinetic turbine can also include the number of turbine blades as an important variable for investigation.

4. Investigate the effects of differences between the two interacting turbines specifically if different turbine diameters or rotational velocities can influence the performance of vertical-axis hydrokinetic turbines.

5. Examine the influence of riverine systems using CFD on the performance of hydrokinetic turbines by including actual river geometries and river profiles to determine how a riverine system can influence the performance of hydrokinetic turbines.

6. Develop an experimental procedure and set-up for studying the interactions between two scale hydrokinetic turbines in a water channel. Depending upon the set-up of the scale turbines, the experimental approach may be able to examine the influence of two hydrokinetic turbines more efficiently than using CFD (due to the intense computational expenses required and restrictions on the number of selected variables that can be modelled and tested). Furthermore, the experimental data acquired during the experiments can be used for validation

of the numerical results obtained by new CFD approaches in the future.

7. Preform experimental field measurements using two actual full-size vertical-axis hydrokinetic turbines in a river system. As the velocity and turbulence levels of the flow enter the turbine differs significantly compared to the flow used in the current CFD and water-tunnel experiments, the in field measurements are needed at the certain stage of this continuing research project.

8. Examine the influence of turbine positioning and rotational direction on marine life. As is clear from this research, positioning can cause significant variations within the turbulence levels for the stationary cases and of rotational direction can influence the turbulence levels. Both these factors have a significant influence on the injury and mortality rates of fish passing through the hydrokinetic turbines.

9. Investigate the influence of multiple vertical-axis hydrokinetic turbines and determine the influence of the additional turbines on the turbine performances by developping a turbine farm efficiency factor to characterize the potential of hydrokinetic turbine farms. This work will lead towards obtaining the ideal spacing for commercial turbine farm applications.

Bibliography

[1] United Nations, "World population prospects the 2012 revision," United Nations, Report, 2013.

[2] U.S. Department of Energy, "International energy outlook 2013," Energy Information Administration, Report, 2013.

[3] A. Evans, V. Strezov, and T. J. Evans, "Assessment of sustainability indicators for renewable energy technologies," *Renewable and Sustainable Energy Reviews*, vol. 13, no. 5, pp. 1082–1088, 2009.

[4] Natural Resources Canada, "Charting the course canada's marine renewable energy technology roadmap," Natural Resources Canada, Report, 2011.

[5] R. Karsten, J. McMillan, M. Lickley, and R. Haynes, "Assessment of tidal current energy in the minas passage, bay of fundy," *Proceedings of the Institution of Mechanical Engineers, Part A: Journal of Power and Energy*, vol. 222, no. 5, pp. 493–507, 2008.

[6] Electrical Power Research Institute, "Asessment and mapping of the riverine hydrokinetic resource in the continental united states," Electrical Power Research Institute, Report, 2012.

[7] French Environment and Energy Management Agency, "Roadmap for renewable marine energy," French Environment and Energy Management

Agency, Report, 2011.

[8] M. Khan, M. Iqbal, and J. Quaicoe, "A technology review and simulation based performance analysis of river current turbine systems," in *Electrical and Computer Engineering, 2006. CCECE.*, May 2006, pp. 2288–2293.

[9] F. Villalpando, M. Reggio, and A. Ilinca, "Assessment of turbulence models for flow simulation around a wind turbine airfoil," *Modelling and Simulation in Engineering*, vol. 2011, p. 8, 2011.

[10] H. Versteeg and W. Malalasekera, *An introduction to computational fluid dynamics - The finite volume method*. Pearson Education Limited, 2007.

[11] P. Beaudan and P. Moin, "Numerical experiments on the flow past a circular cylinder at sub-critical reynolds numbers," CTS Annual Research Briefs, NASA Ames/Stanford University, Technical Report, 1994.

[12] L. Ong and J. Wallace, "The velocity field of the turbulent very near wake of a circular cylinder," *Experiments in Fluids*, vol. 20, no. 6, pp. 441–453, 1996.

[13] P. Parnaudeau, J. Carlier, D. Heitz, and E. Lamballais, "Experimental and numerical studies of the flow over a circular cylinder at reynolds number 3900," *Physics of fluids*, vol. 20, no. 8, 2008.

[14] S. Dong, G. Karniadakis, A. Ekmekci, and D. Rockwell, "A combined direct numerical simulation-particle image velocimetry study of the turbulent near wake," *Journal of fluid mechnaics*, vol. 569, pp. 185–207, 2006.

[15] C. Norberg, "An experimental investigation of the flow around a circular cylinder: influence of aspect ratio," *Journal of Fluid Mechanics*, vol. 258, pp. 287–316, 1994.

[16] L. Lourenco and C. Shih, "Characteristics of the plane turbulent near wake of a circular cylinder, a particle image velocimetry study," CTR Annual Research Briefs, NASA Ames/Stanford University, Technical report, 1994.

[17] X. Ma, G. Karamanos, and G. Karniadakis, "Dynamics and low-dimensionality of a turbulent near wake," *Journal of fluid mechanics*, vol. 410, pp. 29–65, 2000.

[18] M. Breuer, "Large eddy simulation of the subcritical flow past a circular cylinder: numerical and modeling aspects," *International journal for numerical methods in fluids*, vol. 28, no. 9, pp. 1281–1302, 1998.

[19] D. Lysenko, G. Ertesv, S. Ivar, and K. Rian, "Large-eddy simulation of the flow over a circular cylinder at reynolds number 3900 using the openfoam toolbox," *Flow Turbulence and Combustion*, vol. 89, no. 4, pp. 491–518, 2012.

[20] R. Mittal, "Large-eddy simulation of flow past a circular cylinder," Center for Turbulence Research, NASA Ames/Stanford Univ., Report, 1995.

[21] M. Zdravkovich, "The effects of interference between circular cylinders in cross flow," *Journal of Fluids and Structures*, vol. 1, no. 2, pp. 239–261, 1987.

[22] T. Igarashi, "Characteristics of the flow around two circular cylinders arranged in tandem (second report, unique flow phenomenon at small spacing)," *Bulletin of the JSME*, vol. 27, no. -, pp. 2380–2387, 1984.

[23] C. Williamson, "Evolution of a single wake behind a pair of bluff bodies," *Journal of Fluids Mechanics*, vol. 159, pp. 1–18, 1985.

[24] D. Sumner, "Two circular cylinders in cross-flow: a review," *Journal of Fluids and Structures*, vol. 26, no. 6, pp. 849–899, 2010.

[25] J. Shao and C. Zhang, "Large eddy simulations of the flow past two side-by-side circular cylinders," *International Journal of Computational Fluid Dynamics*,

vol. 22, no. 6, pp. 393–404, 2008.

[26] *Fine large eddy simulation of the flow around one and two side-by-side infinite cylinders at subcritical Reynolds numbers*, 2010.

[27] I. Afgan, Y. Kahil, S. Benhamadouche, and P. Sagaut, "Large eddy simulation of the flow around single and two side-by-side cylinders at subcritical reynolds numbers," *Physics of Fluids*, vol. 23, no. 7, 2011.

[28] C. Ng and N. Ko, "Flow interaction behind two circular cylinders of equal diameter - a numerical study," *Journal of Wind Engineering and Industrial Aerodynamics*, vol. 54, pp. 277–287, 1995.

[29] M. Alam, M. Moriya, and H. Sakamoto, "Aerodynamic characteristics of two side-by-side circular cylinders and application of wavelet analysis on the switching phenomenon," *Journal of Fluids and Structures*, vol. 18, no. 34, pp. 325–346, 2003.

[30] P. Bearman and A. Wadcock, "The interaction between a pair of circular cylinders normal to a stream," *Journal of Fluid Mechanics*, vol. 61, no. 3, pp. 499–511, 1973.

[31] *The interfecence between struts in various combinations*, 1933.

[32] D. Sumner, M. Richards, and O. Akosile, "Two staggered circular cylinders of equal diameter in cross-flow," *Journal of Fluids and Structures*, vol. 20, no. 2, pp. 255–276, 2005.

[33] O. Akosile and D. Sumner, "Staggered circular cylinders immersed in a uniform planar shear flow," *Journal of Fluids and Structures*, vol. 18, no. 5, pp. 613–633, 2003.

[34] D. Sumner and M. Richards, "Some vortex-shedding characteristics of the staggered configuration of circular cylinders," *Journal of Fluids and Structures*, vol. 17, no. 3, pp. 345–350, 2003.

[35] M. Alam, H. Sakamoto, and Y. Zhou, "Determination of flow configurations and fluid forces acting on two staggered circular cylinders of equal diameter in cross-flow," *Journal of Fluids and Structures*, vol. 21, no. 4, pp. 363–394, 2005.

[36] A. Birjandi, "Effect of flow and fluid structures on the performance of vertical river hydrokinetic turbines," Ph.D. dissertation, The University of Manitoba, 2012.

[37] J. Dabiri, "Potential order-of-magnitude enhancement of wind farm power density via counter-rotating vertical-axis wind turbine arrays," *Journal of Renewable and Sustainable Energy*, vol. 3, no. 4, 2011.

[38] R. Whittlesey, S. Liska, and J. Dabiri, "Fish schooling as a basis for vertical axis wind turbine farm design," *Bioinspiration and Biomimetics*, vol. 5, no. 3, 2010.

[39] M. Kinzel, Q. Mulligan, and J. Dabiri, "Energy exchange in an array of vertical-axis wind turbines," *Journal of Turbulence*, vol. 13, 2012.

[40] *A parameter study of the influence of struts on the performance of a vertical-axis marine current turbine.*, 2009.

[41] J. Barthelmie, S. Frandsen, M. Nielsen, S. Pryor, P. Rethore, and H. Jrgensen, "Modelling and measurements of power losses and turbulence intensity in wind turbine wakes at middelgrunden offshore wind farm," *Wind Energy*, vol. 10, no. 6, pp. 517–528, 2007.

[42] A. Birjandi, E. Bibeau, and J. Woods, "Investigation of macro-turbulent flow structures interaction with a vertical hydrokinetic river turbine," *Renewable*

Energy, vol. 48, no. 0, pp. 183 – 192, 2012.

[43] K. Golecha, T. Eldho, and S. Prabhu, "Study on the interaction between two hydrokinetic savonius turbines," *International Journal of Rotating Machinery*, 2012.

[44] A. Shigetomi, Y. Murai, Y. Tasaka, and Y. Takeda, "Interactive flow field around two savonius turbines," *Renewable Energy*, vol. 36, no. 2, pp. 536–545, 2011.

[45] *The effect of boundary proximity upon the wake structure of horizontal axis marine current turbines*. The American Society of Mechanical Engineers, 2008.

[46] T. Burton, D. Sharpe, and N. Jenkins, *Wind energy handbook*. John Wiley and Sons Ltd., 2001.

[47] A. Betz, *Wind-energie und ihre ausnutzung durch windmühlen*. Vandenhoeck, 1926.

[48] J. Manwell, J. McGowan, and A. Rogers, *Wind energy explained: theory desing and application*. John Wiley and Sons Ltd., 2009.

[49] B. Kirke, "Tests on ducted and bare helical and straight blade darrieus hydrokinetic turbines," *Renewable Energy*, vol. 36, no. 11, pp. 3013–3022, 2011.

[50] U. Piomelli, "Large-eddy and direct simulation of turbulent flows," 2001.

[51] J. Smagorinsky, "General circulation experiments with primitive equations: I. the basic experiment," *Monthly Weather Review*, pp. 99–164, 1963.

[52] D. Lilly, "A proposed modification of the germano subgridscale closure method," *Physics of Fluids A: Fluid Dynamics*, vol. 4, no. 3, pp. 633–635, 1992.

[53] M. Germano, U. Piomelli, P. Moin, and W. Cabot, "A dynamic subgridscale eddy viscosity model," *Physics of Fluids A: Fluid Dynamics (1989-1993)*, vol. 3, no. 7, pp. 1760–1765, 1991.

[54] F. Menter, M. Kuntz, and R. Langtry, "Ten years of industrial experience with the sst turbulence model," *Turbulence, heat and mass transfer*, vol. 4, no. 1, 2003.

[55] F. Mentor, "Performance of popular turbulence models for attached and separated adverse pressure gradient flow," *AIAA*, vol. 30, pp. 2066–2072, 1992.

[56] H. Choi and P. Moin, "Grid-point requirements for large eddy simulation: Chapman's estimates revisited," *Physics of Fluids*, vol. 24, no. 1, 2012.

[57] P. Moin, "Advances in large eddy simulation methodology for complex flows," *International Journal of Heat and Fluid Flow*, vol. 23, no. 5, pp. 710–720, 2002.

[58] U. Piomelli, "Large-eddy simulation: achievements and challenges," *Progress in Aerospace Sciences*, vol. 35, no. 4, pp. 335–362, 1999.

[59] S. Pope, "Ten questions concerning the large-eddy simulation of turbulent flows," *New Journal of Physics*, vol. 6, no. 1, 2004.

[60] R. Bouffanais, "Advances and challenges of applied large-eddy simulation," *Computers and Fluids*, vol. 39, no. 5, pp. 735–738, 2010.

[61] S. Murakami, "Current status and future trends in computational wind engineering," *Journal of Wind Engineering and Industrial Aerodynamics*, vol. 6768, no. 0, pp. 3–34, 1997.

[62] W. Rodi, "Comparison of les and rans calculations of the flow around bluff bodies," *Journal of Wind Engineering and Industrial Aerodynamics*, vol. 6971, no. 0, pp. 55–75, 1997.

[63] Y. Cheng, F. Lien, E. Yee, and R. Sinclair, "A comparison of large eddy simulations with a standard k reynolds-averaged navierstokes model for the prediction of a fully developed turbulent flow over a matrix of cubes," *Journal of Wind Engineering and Industrial Aerodynamics*, vol. 91, no. 11, pp. 1301–1328, 2003.

[64] M. Caciolo, P. Stabat, and D. Marchio, "Numerical simulation of single-sided ventilation using rans and les and comparison with full-scale experiments," *Building and Environment*, vol. 50, no. 0, pp. 202–213, 2012.

[65] I. Afgan, J. McNaughton, S. Rolfo, D. Apsley, T. Stallard, and P. Stansby, "Turbulent flow and loading on a tidal stream turbine by les and rans," *International Journal of Heat and Fluid Flow*, vol. 43, no. 0, pp. 96–108, 2013.

[66] C. Li, S. Zhu, Y. Xu, and Y. Xiao, "2.5d large eddy simulation of vertical axis wind turbine in consideration of high angle of attack flow," *Renewable Energy*, vol. 51, no. 0, pp. 317–330, 2013.

[67] S. Kang, I. Borazjani, J. Colby, and F. Sotiropoulos, "Numerical simulation of 3d flow past a real-life marine hydrokinetic turbine," *Advances in Water Resources*, vol. 39, no. 0, pp. 33–43, 2012.

[68] *Large Eddy Simulations of large wind-turbine arrays in the atmospheric boundary layer*, 2010.

[69] S. Turnock, A. Phillips, J. Banks, and R. Nicholls-Lee, "Modelling tidal current turbine wakes using a coupled rans-bemt approach as a tool for analysing power capture of arrays of turbines," *Ocean Engineering*, vol. 38, no. 1112, pp. 1300–1307, 2011.

[70] *Flow field characteristics analysis of a horizontal axis marine current turbine by large eddy simulation*, 2013.

[71] M. Calaf, M. Parlange, and C. Meneveau, "Large eddy simulation study of scalar transport in fully developed wind-turbine array boundary layers," *Physics of Fluids (1994-present)*, vol. 23, no. 12, 2011.

[72] Y. Wu and F. Port-Agel, "Large-eddy simulation of wind-turbine wakes: evaluation of turbine parametrisations," *Boundary-Layer Meteorology*, vol. 138, no. 3, pp. 345–366, 2011.

[73] W. Cleijine, "Results of sexbierum wind farm report," MT-TNO Apeldoorn, Report, 1992.

[74] A. Jimenez, A. Crespo, E. Migoya, and J. Garcia, "Advances in large-eddy simulation of a wind turbine wake," *Journal of Physics: Conference Series*, vol. 75, no. 1, 2007.

[75] M. Gebreslassie, G. Tabor, and M. Belmont, "Numerical simulation of a new type of cross flow tidal turbine using openfoam part ii: Investigation of turbine-to-turbine interaction," *Renewable Energy*, vol. 50, no. 0, pp. 1005–1013, 2013.

[76] X. Bai, E. Avital, A. Munjiza, and J. Williams, "Numerical simulation of a marine current turbine in free surface flow," *Renewable Energy*, vol. 63, no. 0, pp. 715–723, 2014.

[77] M. Churchfield, Y. Li, and P. Moriarty, "A large-eddy simulation of wake propagation and power production in an array of tidal-current turbines," *Philosophical Transactions of the Royal Society*, vol. 371, no. 1985, 2013.

[78] J. McNaughton, F. Billard, and A. Revell, "Turbulence modelling of low reynolds number flow effects around a vertical axis turbine at a range of tip-speed ratios," *Journal of Fluids and Structures*, vol. 47, no. 0, pp. 124–138, 2014.

[79] T. Matre, E. Amet, and C. Pellone, "Modeling of the flow in a darrieus water turbine: Wall grid refinement analysis and comparison with experiments," *Renewable Energy*, vol. 51, no. 0, pp. 497–512, 2013.

[80] I. Dobrev and F. Massouh, "Cfd and piv investigation of unsteady flow through savonius wind turbine," *Energy Procedia*, vol. 6, no. 0, pp. 711–720, 2011.

[81] D. Gaden, "An investigation of river kinetic turbines: Performance enhancemens, turbine modelling techniques, and an assessment of turbulence models," Master's thesis, The University of Manitoba, 2007.

[82] P. Pritchard, *Fox and McDonald's Introduction to Fluid Mechanics, 8th Edition*. John Wiley & Sons, 2010.

[83] H. Tennekes and J. Lumley, *A first course in turbulence*. MIT, USA, 1972.

[84] H. Vu, J. Ahn, and J. Hwang, "Numerical simulation of flow past two circular cylinders in tandem and side-by-side arrangement at low reynolds numbers," *KSCE Journal of Civil Engineering*, pp. 1–11, 2015.

[85] J. Anderson, *Fundamentals of Areaodynamics*. McGraw Hill International, 2007.

[86] Electric Power Research Institute, "Environmental effects of hydrokinetic turbines on fish: desktop and laboratory flume studies 2012," Electric Power Research Institute, Report, 2012.

[87] M. Odeh, J. Noreika, A. Haro, A. Naynard, and T. Castro-Santos, "Evaluation of the effects of turbulence on the behavior of migratory fish," Glenn F. Cada - Oak Ridge National Laboratory, Report, 2012.

[88] L. Hammar, S. Andersson, L. Eggertsen, J. Haglund, M. Gullstrm, J. Ehnberg, and S. Molander, "Hydrokinetic turbine effects on fish swimming behaviour,"

PLoS ONE, vol. 8, no. 12, 2013.

[89] S. Turki, H. Abbassi, and S. Nasrallah, "Effect of the blockage ratio on the flow in a channel with a built-in square cylinder," *Computational Mechanics*, vol. 33, no. 1, pp. 22–29, 2003.

[90] I. Bajec and F. Heppner, "Organized flight in birds," *Animal Behaviour*, vol. 78, no. 4, pp. 777–789, 2009.

[91] J. Maeng, J. Park, S. Jang, and S. Han, "A modeling approach to energy savings of flying canada geese using computational fluid dynamics," *Journal of Theoretical Biology*, vol. 320, pp. 76–85, 2013.

[92] F. Hainsworth, "Precision and dynamics of positioning by canada geese flying in formation," *Journal of Experimental Biology*, vol. 128, no. 1, pp. 445–462, 1987.

[93] S. Marras, S. Killen, J. Lindstrom, D. McKenzie, J. Steffensen, and P. Domenici, "Fish swimming in schools save energy regardless of their spatial position," *Behavioral Ecology and Sociobiology*, vol. 69, no. 2, pp. 219–226, 2015.

[94] Nortek, "Vectrino 3d water velocity sensor lab probe," Nortek, Report, 2013.

[95] V. Martin, T. Fisher, R. Millar, and M. Quick, "Adv data analysis for turbulent flows: Low correlation problem," in *Proceedings of Hydraulic Measurements and Experimental Methods Conference 2002. ASCE Conf. Proc.*, vol. 10, 2002.

[96] B. Khorsandi, L. Mydlarski, and S. Gaskin, "Noise in turbulence measurements using acoustic doppler velocimetry," *Journal of Hydraulic Engineering*, vol. 138, no. 10, pp. 829–838, 2012.

[97] A. Birjandi and E. Bibeau, "Improvement of acoustic doppler velocimetry in bubbly flow measurements as applied to river characterization for kinetic

turbines," *International Journal of Multiphase Flow*, vol. 37, no. 8, pp. 919–929, 2011.

[98] S. Bell, "Measurement good practice guide no. 11 (issue 2)," *A Beginners Guide to Uncertainty of Measurement. National Physical Laboratory Teddington, Middlesex, United Kingdom*, 2001.

[99] C. F. Dietrich, *Uncertainty, calibration and probability: the statistics of scientific and industrial measurement.* CRC Press, 1991.

[100] S. d'Auteuil, A. Birjandi, J. Soviak, and E. Bibeau, "Flow measurement on assiniboine river at the forks for hydrokinetic turbine deployment purposes," Canadian Turbine Testing Center, Technical Report, 2015.

[101] "Best practice guidelines for turbomachinery cfd," www.cfd-online.com/Wiki/Best_practice_guidelines_for_turbomachinery_CFD, accessed: 2015-07-24.

[102] J. Ferziger and M. Peric, *Computational methods for fluid dynamics.* Springer Science & Business Media, 2012.

[103] M. Akbarzadeh, M. Birouk, and B. Sarh, "Numerical simulation of a turbulent free jet issuing from a rectangular nozzle," *Computational Thermal Sciences: An International Journal*, vol. 4, no. 1, 2012.

Appendix A

Cylinder contour plots

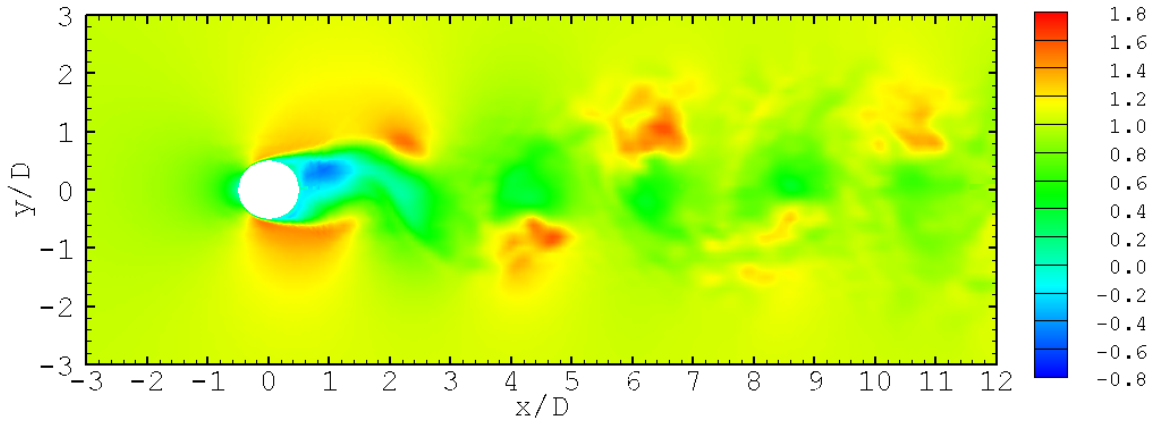

(a) Instantaneous streamwise velocity $\bar{u}/U_\infty$ around a single cylinder at time $tU_\infty/D = 585$

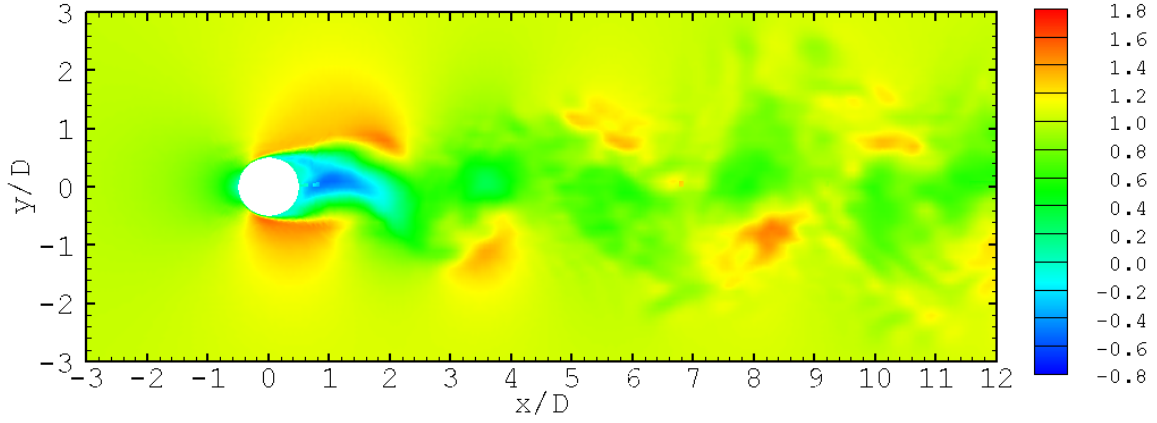

(b) Instantaneous streamwise velocity $\bar{u}/U_\infty$ around a single cylinder at time $tU_\infty/D = 780$

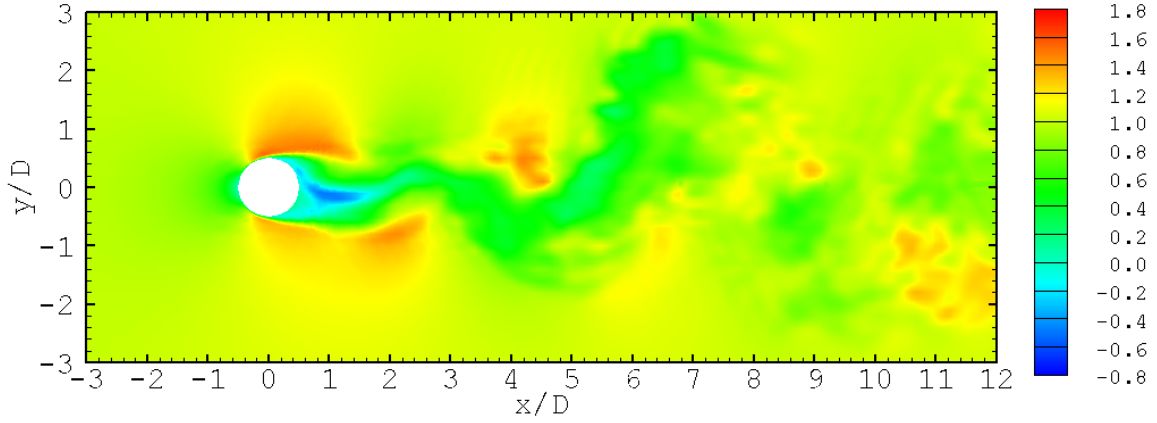

(c) Instantaneous streamwise velocity $\bar{u}/U_\infty$ around a single cylinder at time $tU_\infty/D = 975$

Figure A.1: Instantaneous streamwise velocity $\bar{u}/U_\infty$ behind a single cylinder for three different times

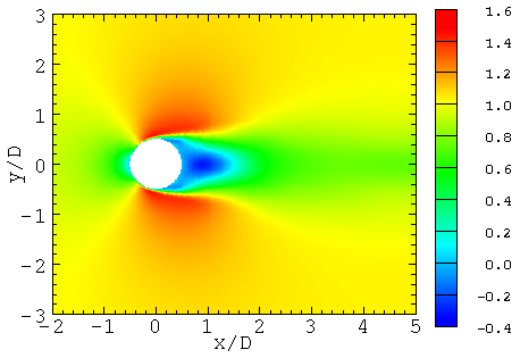

(a) Mean streamwise velocity $\langle\bar{u}\rangle/U_\infty$ around a single cylinder

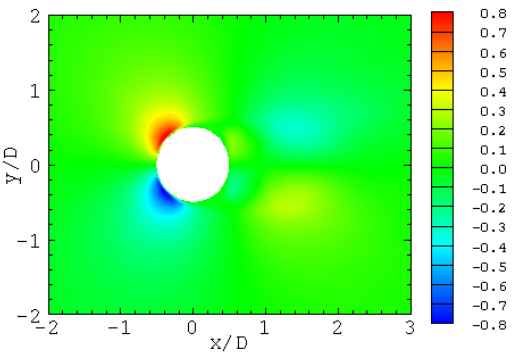

(b) Mean spanwise velocity $\langle\bar{v}\rangle/U_\infty$ around a single cylinder

Figure A.2: Mean streamwise velocity $\langle\bar{u}\rangle/U_\infty$ and mean spanwise velocity $\langle\bar{v}\rangle/U_\infty$ around a single cylinder.

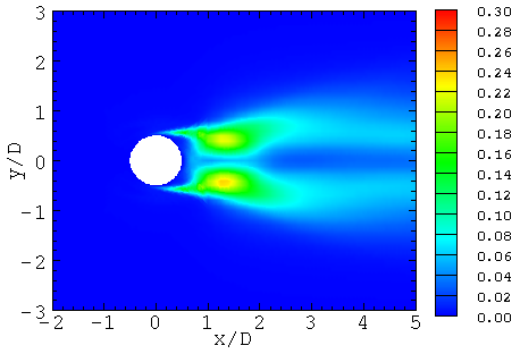

(a) Reynolds normal stress component $\langle\bar{u}'\bar{u}'\rangle/U_\infty^2$ behind a single cylinder

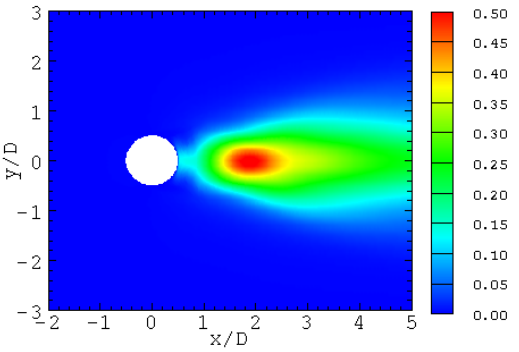

(b) Reynolds normal stress component $\langle\bar{v}'\bar{v}'\rangle/U_\infty^2$ behind a single cylinder

Figure A.3: Reynolds normal stress components $\langle\bar{u}'\bar{u}'\rangle/U_\infty^2$ and $\langle\bar{v}'\bar{v}'\rangle/U_\infty^2$ behind a single cylinder

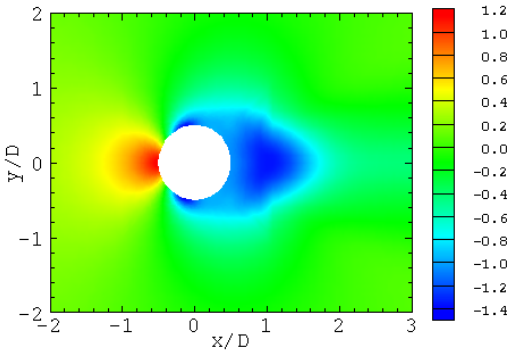

Figure A.4: Average pressure coefficients behind a single cylinder

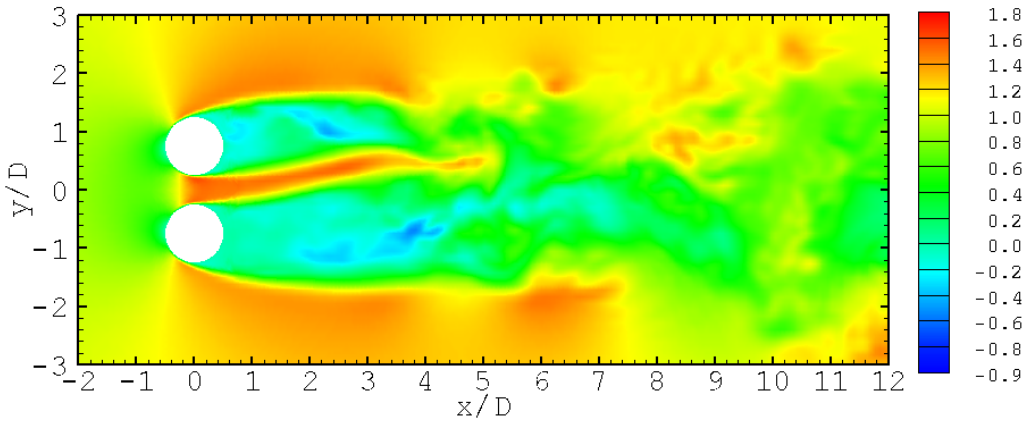

(a) Instantaneous streamwise velocity $\bar{u}/U_\infty$ around side-by-side cylinders separated by $T/D = 1.5$ at time $tU_\infty/D = 960$ separated by $T/D = 1.5$.

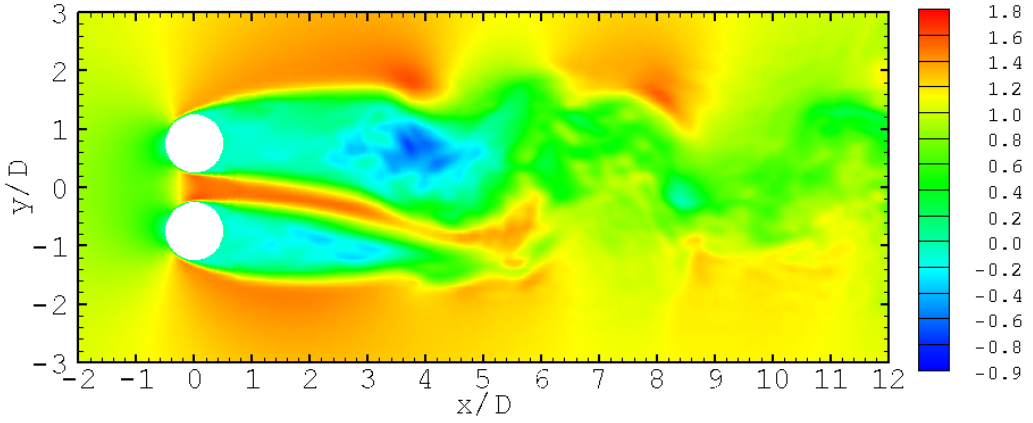

(b) Instantaneous streamwise velocity $\bar{u}/U_\infty$ around side-by-side cylinders separated by $T/D = 1.5$ at time $tU_\infty/D = 1965$ separated by $T/D = 1.5$.

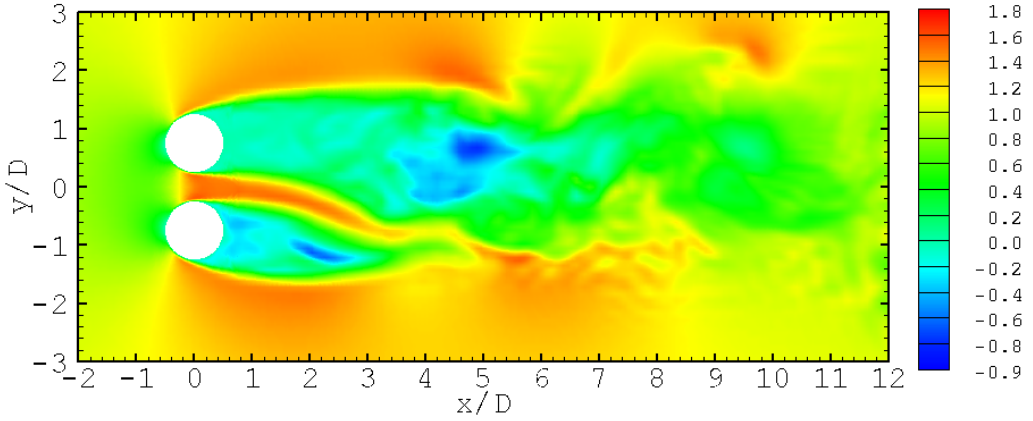

(c) Instantaneous streamwise velocity $\bar{u}/U_\infty$ around side-by-side cylinders separated by $T/D = 1.5$ at time $tU_\infty/D = 2250$ separated by $T/D = 1.5$.

Figure A.5: Instantaneous streamwise velocity $\bar{u}/U_\infty$ behind staggered cylinders for three different times

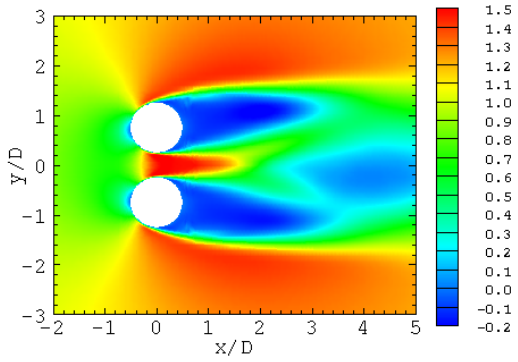

(a) Mean streamwise velocity $\langle\bar{u}\rangle/U_\infty$ around side-by-side cylinders

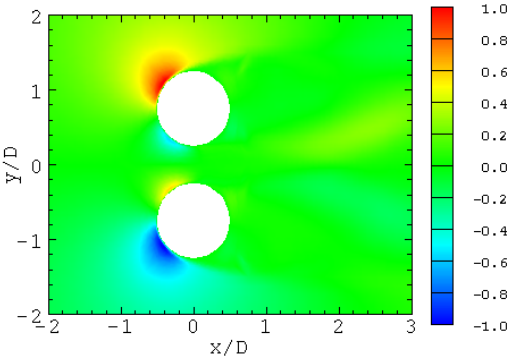

(b) Mean spanwise velocity $\langle\bar{v}\rangle/U_\infty$ around side-by-side cylinders.

Figure A.6: Mean streamwise velocity $\langle\bar{u}\rangle/U_\infty$ and mean spanwise velocity $\langle\bar{v}\rangle/U_\infty$ around side-by-side cylinders separated by $T/D = 1.5$. The asymetry is caused by a bias in the averaging period.

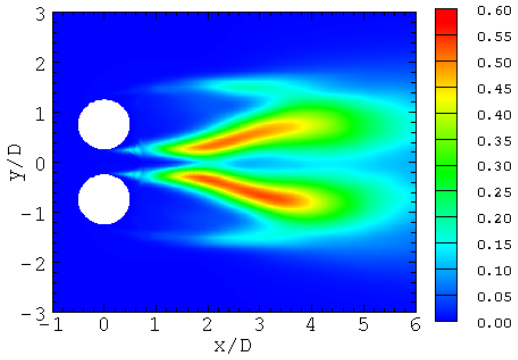

(a) Reynolds normal stress component $\langle\bar{u}'\bar{u}'\rangle/U_\infty^2$ behind side-by-side cylinders

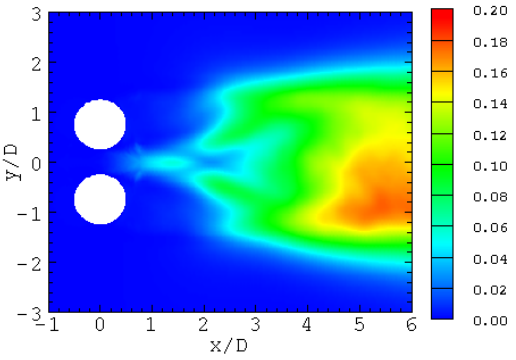

(b) Reynolds normal stress component $\langle\bar{v}'\bar{v}'\rangle/U_\infty^2$ behind side-by-side cylinders

Figure A.7: Reynolds normal stress components $\langle\bar{u}'\bar{u}'\rangle/U_\infty^2$ and $\langle\bar{v}'\bar{v}'\rangle/U_\infty^2$ behind side-by-side cylinders separated by $T/D = 1.5$. The asymetry is caused by a bias in the averaging period.

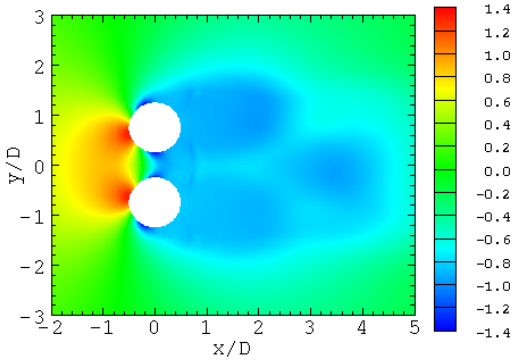

Figure A.8: Average pressure coefficients around side-by-side cylinders separated by $T/D = 1.5$. The asymetry is caused by a bias in the averaging period.

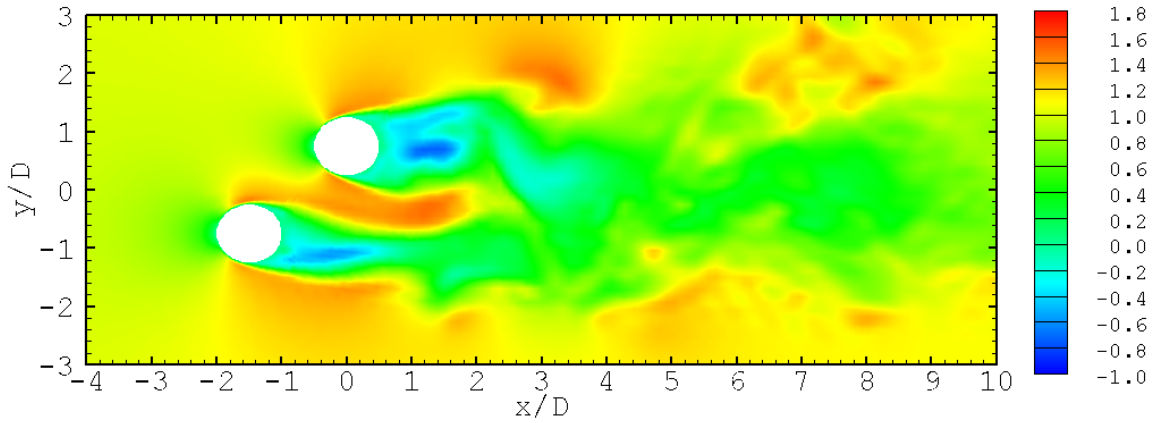

(a) Instantaneous streamwise velocity $\bar{u}/U_\infty$ around staggered cylinders at time $tU_\infty/D = 450$ separated by $T/D = L/D = 1.5$

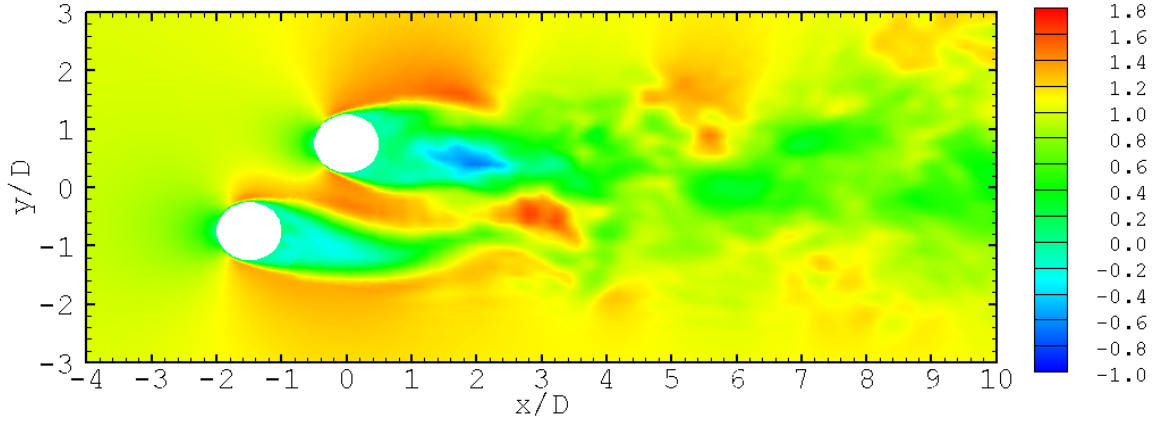

(b) Instantaneous streamwise velocity $\bar{u}/U_\infty$ around staggered cylinders at time $tU_\infty/D = 570$ separated by $T/D = L/D = 1.5$

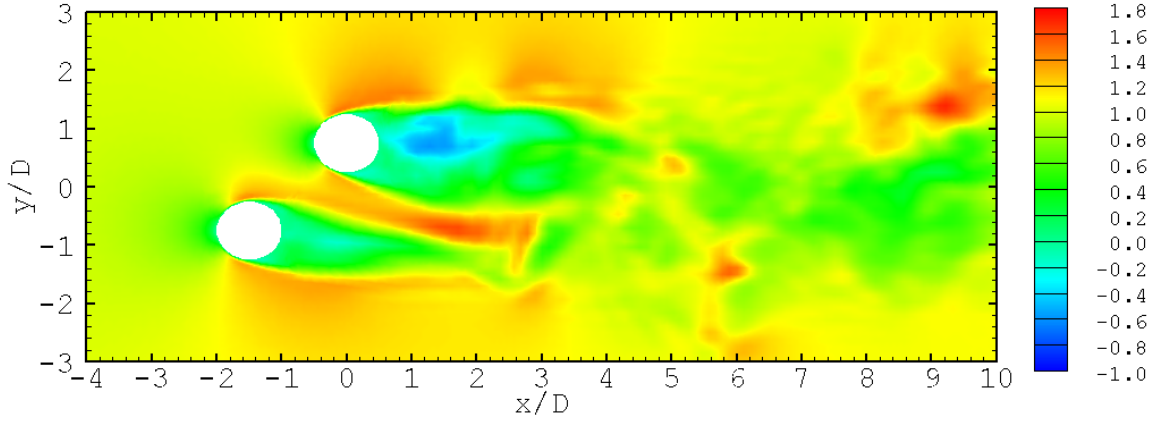

(c) Instantaneous streamwise velocity $\bar{u}/U_\infty$ around staggered cylinders at time $tU_\infty/D = 690$ separated by separated by $T/D = L/D = 1.5$

Figure A.9: Instantaneous streamwise velocity $\bar{u}/U_\infty$ behind staggered cylinders for three different times

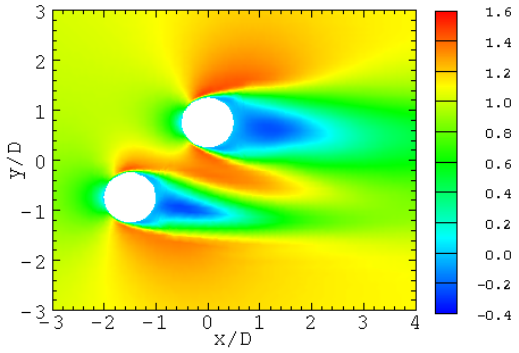

(a) Mean streamwise velocity $\langle\bar{u}\rangle/U_\infty$ around staggered cylinders

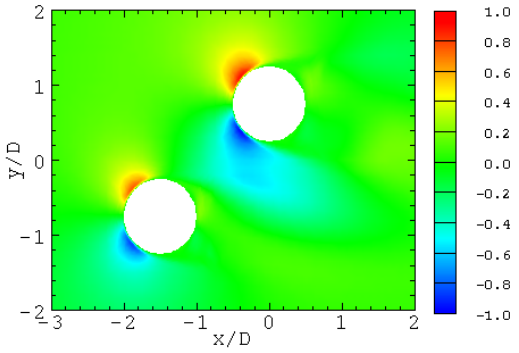

(b) Mean spanwise velocity $\langle\bar{v}\rangle/U_\infty$ around staggered cylinders

Figure A.10: Mean streamwise velocity $\langle\bar{u}\rangle/U_\infty$ and mean spanwise velocity $\langle\bar{v}\rangle/U_\infty$ around staggered cylinders separated by $T/D = L/D = 1.5$.

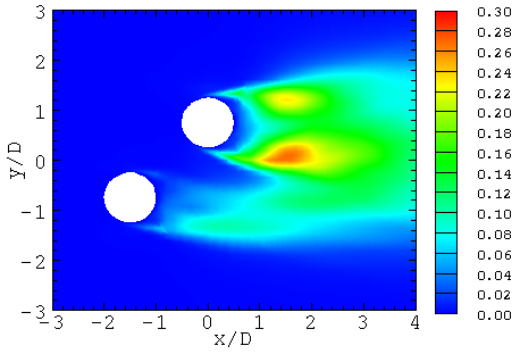

(a) Reynolds normal stress component $\langle\bar{u}'\bar{u}'\rangle/U_\infty^2$ behind staggered cylinders

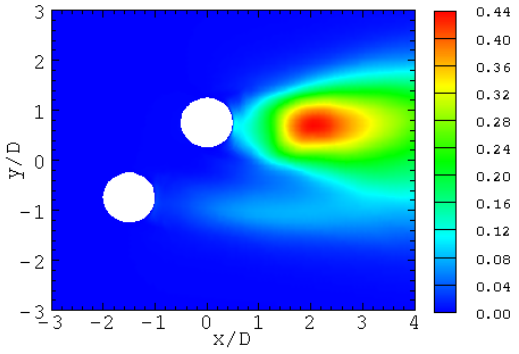

(b) Reynolds normal stress component $\langle\bar{v}'\bar{v}'\rangle/U_\infty^2$ behind staggered cylinders

Figure A.11: Reynolds normal stress components $\langle\bar{u}'\bar{u}'\rangle/U_\infty^2$ and $\langle\bar{v}'\bar{v}'\rangle/U_\infty^2$ behind staggered cylinders separated by $T/D = L/D = 1.5$

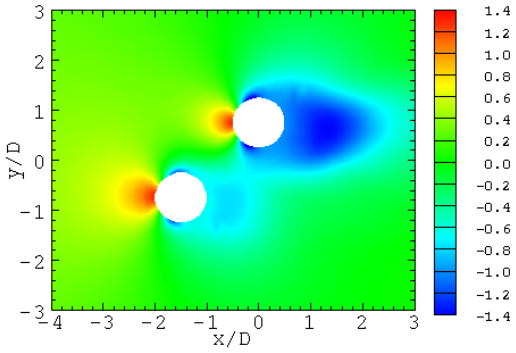

Figure A.12: Average pressure coefficients behind staggered cylinders separated by $T/D = L/D = 1.5$